Measurement of the Branching Ratio $B \to D^{**}\ell\nu_\ell$ using the hadronic Full Event Interpretation with Belle II Data

Dissertation

zur Erlangung des mathematisch-naturwissenschaftlichen Doktorgrades
„Doctor rerum naturalium“
der Georg-August-Universität Göttingen

im Promotionsprogramm ProPhys
der Georg-August University School of Science (GAUSS)

vorgelegt von

Noreen Rauls

aus Peine

Göttingen, 2024

Betreuungsausschuss

Prof. Dr. Ariane Frey
Dr. Benjamin Schwenker
Prof. Dr. Stan Lai

Mitglieder der Prüfungskommission:

Referentin:	Prof. Dr. Ariane Frey II. Physikalisches Institut, Georg-August-Universität Göttingen
Koreferent:	Prof. Dr. Thibaud Humair II. Physikalisches Institut, Georg-August-Universität Göttingen

Weitere Mitglieder der Prüfungskommission:

PD Dr. Jörn Große-Knetter
II. Physikalisches Institut, Georg-August-Universität Göttingen

Prof. Dr. Stan Lai
II. Physikalisches Institut, Georg-August-Universität Göttingen

Prof. Dr. Steffen Schumann
Institut für Theoretische Physik, Georg-August-Universität Göttingen

Prof. Dr. Baida Achkar
II. Physikalisches Institut, Georg-August-Universität Göttingen

Tag der mündlichen Prüfung: 27.05.2024

Für meine Familie.

Measurement of the Branching Ratio $B \to D^{**}\ell\nu_\ell$ using the hadronic Full Event Interpretation with Belle II Data

Abstract

The Belle II detector is situated at the asymmetric $e^- e^+$ collider SuperKEKB at KEK in Tsukuba in Japan, which operates with an energy slightly above the mass of the $\Upsilon(4S)$ resonance. As a result, pairs of B mesons are predominantly produced. Due to the clean experimental environment, various measurements to test the Standard Model and precisely determine its parameters can be performed. This is e.g. the element V_{cb} of the CKM matrix among others, where one of the leading systematic uncertainties arises due to decays of the nature $B \to D^{**}\ell\nu_\ell$.
This thesis presents the first measurement of the branching ratio $B \to D^{**}\ell\nu_\ell$ using the data set collected with the Belle II detector between 2019 and 2022 and corresponds to about $364\,\mathrm{fb}^{-1}$ of integrated luminosity at the $\Upsilon(4S)$ resonance. To reconstruct the "other" B meson, a multivariate analysis tool called "Full Event Interpretation" is used, which reconstructs a variety of different hadronic decay modes. For the reconstruction of the signal side B meson, a light charged lepton is combined with a D^{**} meson that is reconstructed from various $D\pi$ and $D^*\pi$ combinations. In contrast to previously performed analyses, this analysis also takes the π^0 into account in the reconstruction of the D^{**} meson.
A selection of events is applied to obtain a sample enriched in $B \to D^{**}\ell\nu_\ell$ decays and a binned maximum likelihood fit is performed to determine the branching ratio for the different $B \to D^{**}\ell\nu_\ell$ decay channels. To account for effects in the simulation that are currently not well understood, the branching ratio is normalised to the branching ratio of the much more frequent decay $B \to D^*\ell\nu_\ell$.

Messung des Verzweigungsverhältnisses des Zerfalls $B \to D^{**}\ell\nu_\ell$ unter Verwendung der Full Event Interpretation mit Belle II-Daten

Zusammenfassung

Der Belle II-Detektor befindet sich am asymmetrischen e^-e^+-Beschleunigerring SuperKEKB am KEK in Tsukuba in Japan, welcher bei einer Energie leicht oberhalb der Masse der $\Upsilon(4S)$-Resonanz läuft. Aufgrund dessen werden hauptsächlich B-Meson-Paare produziert. Diese können wegen der relativ sauberen experimentellen Umgebung genutzt werden, um verschiedene Messungen zur Untersuchung des Standardmodells durchzuführen. Des Weiteren können unterschiedliche Parameter genau bestimmt werden. Einer dieser Parameter ist das CKM-Matrixelement V_{cb}, welches als eine Hauptquelle der systematischen Unsicherheiten die Zerfälle $B \to D^{**}\ell\nu_\ell$ besitzt.
Diese Arbeit präsentiert eine erste Messung des Zerfallsverhältnisses von $B \to D^{**}\ell\nu_\ell$-Zerfällen unter Verwendung des Belle II-Datensatzes, welcher zwischen 2019 und 2022 mit einer integrierten Luminosität von $364\,\mathrm{fb}^{-1}$ auf der $\Upsilon(4S)$-Resonanz aufgenommen wurde. Zur Rekonstruktion des „anderen "B-Mesons wird die Full Event Interpretation verwendet. Hierbei handelt es sich um ein multivariates Analysewerkzeug, welches eine Vielzahl an hadronischen Zerfallsmoden rekonstruiert. Zur Rekonstruktion des B-Mesons auf der Signalseite wird ein leichtes geladenens Lepton mit einem D^{**}-Meson kombiniert, wobei diese mit Hilfe von verschiedenen $D\pi$- und $D^*\pi$-Kombinationen rekonstruiert werden. Im Vergleich zu vorangegangenen Analysen werden hier auch explizit die D^{**}-Meson-Moden rekonstruiert, welche ein π^0 beinhalten.
Eine Selektion der Ereignisse wird vorgenommen, um einen Datensatz mit vielen $B \to D^{**}\ell\nu_\ell$-Zerfällen zu erhalten. Mit Hilfe eines gebinnten Maximum-Likelihood-Fits werden die einzelnen Zerfallsraten der $B \to D^{**}\ell\nu_\ell$-Zerfälle bestimmt. Aufgrund dessen, dass in der Simulation noch Effekte auftreten können, welche bisher noch unverstanden sind, werden die Zerfallsraten mit dem viel häufiger auftretenden Zerfall $B \to D^*\ell\nu_\ell$ normiert.

Contents

CHAPTER 1

Introduction

The Standard Model of particle physics encodes our current understanding of the fundamental constituents of the universe and their interactions.
The first discovery of an elementary particle now contained in the Standard Model, the electron, was already in 1897 by J.J. Thomson [1] using cathode rays. In the following first half of the 20^{th} century, further experiments analysing the structures of the atoms and nuclei were performed, whereas the second half of the century focused more on the structures that are currently thought of as fundamental.
In 1911, Rutherford [2] conducted his famous experiment, which consisted of shooting alpha particles on a very thin gold foil. This gave the first insight into the structure of an atom, that atoms consist of a heavy nucleus that is surrounded by electrons. During the following years, the constituents of the nucleus, the proton [3] and the neutron [4], were discovered in 1919 and 1931, respectively.
By this point, the understanding of the atomic structure had progressed significantly. However, there were still many exciting new discoveries left to be made, such as the muons [5] (1938) and the charged pions [6] (1947) in cosmic rays.
In parallel to the experimental discoveries of particles, there were also major advances in theoretical physics, such as the mass-energy equivalence, special relativity and the photo electric effect by Albert Einstein [7–10]. Moreover, Max Planck introduced the concept of quantisation of energy [11]. These discoveries resulted in the emergence of a new field. Namely, quantum mechanics in the 1920's with the wave formulation by Schrödinger [12] and quantum mechanics [13–15] by Heisenberg. Quantum mechanics and Einstein's theory of special relativity were then combined into the relativistic Dirac wave equation by Paul Dirac [16, 17]. After around another 30 years of evolution, this resulted in the theory used to describe quantum electrodynamics [18–27] in the Standard Model of particle physics in the 1950's.
Over the following years, new particles detectors were built and higher energies reached,

which resulted in even more particles that were discovered without a visible pattern. To bring some order into the *particle zoo*, the special unitary group $SU(3)$ was devised. This led to the prediction of the quark model by Gell-Mann [28] and Zweig [29]. By also introducing the concept of a colour charge and some further developments, the theory of quantum chromodynamics (QCD) [30–32] to describe the strong force was born.
The discovery of the $W^{\pm}$ [33, 34] and the Z boson [35, 36] in the coming years led to the assumption that the theory for the weak and the electromagnetic force could be combined into a single theory, named the electroweak theory [37–39].
With the discovery of the b quark in 1977 [40], the gluon in 1979 [41–44] and the t quark in 1995 [45, 46], all particles required for QCD were discovered.
The last particles to be discovered were the τ neutrino in 2000 [47] and the Higgs boson [48, 49] in 2012, the latter of which was still a missing piece for the generation of mass in the Standard Model.
As of today, the Standard Model is a well established theory, however, a few observed phenomena still cannot be explained.
One such example is the observed asymmetry between matter and anti-matter in the universe. Despite the assumption that equal amounts of matter and antimatter were produced in the early universe, the observable universe is now predominantly composed of matter. To address this asymmetry, Sakharov [50] proposed three essential criteria. The first criterion is the violation of baryon number conservation and the second requires CP violation. The third and last criterion demands interactions out of equilibrium.
The first two criteria can be tested with particle physics experiments, however the CP violation predicted by the Standard Model in the weak interaction is still too small. Therefore, this is further investigated at e.g. the Belle II detector, which focusses on weak decays of the B meson.
The $b \to c$ transitions are of particular interest. A ratio of the decay branching fraction involving a τ lepton divided by the branching fraction of a $b \to c$ transition and a light charged lepton can be used to probe the Standard Model, as the heavy τ lepton might have enhanced couplings to new particles not yet discovered. To get a very precise measurement, all the background components need to be understood well. One of the main backgrounds for this analysis is the decay $B \to D^{**}\ell\nu_\ell$. Therefore, this analysis performs a first measurement of the decay rate $B \to D^{**}\ell\nu_\ell$ at Belle II using a binned maximum likelihood fit.
First, the Standard Model of Particle Physics is described in some more detail as well as the so far measured branching ratios for the $B \to D^{**}\ell\nu_\ell$ decays in chapter 2. In chapter 3 the experimental setup is explained, followed by the utilised recorded and simulated data set in chapter 4. For this analysis certain tools are required that are explained in chapter 5, followed by a thorough description of the reconstruction in chapter 6. In the next chapter, chapter 7, the validation of the simulated data set is illustrated. Afterwards, the method for determining the branching ratio is described in chapter 8 including the systematic uncertainties. Lastly, a conclusion and outlook are given in chapter 9.
If not explicitly stated, the charge-conjugated modes are also considered in this thesis. This means that every particle is exchanged by its corresponding anti-particle.

CHAPTER 2

Theory

2.1. Standard Model of Particle Physics

The Standard Model of Particle Physics (SM) [37–39, 51–58] describes the elementary particles and their interactions, the different forces. The SM is a relativistic local quantum field theory based on the $\mathrm{SU(3)_C \times SU(2)_L \times U(1)_Y}$ combined gauge groups. Being one of the best tested theories, the SM is still not able to explain everything. It can be used to explain three of the four fundamental forces, meaning the strong, the electromagnetic and the weak force. So far, gravity cannot be described by the SM, but the time and length scales considered for particle physics are comparably short and the mass scale very small and thus gravity does not need to be not considered here.
A schematic of the SM and all its elementary particles can be seen in fig. 2.1.
The three fundamental forces are mediated by spin-1-bosons. The gluons (g) are the massless bosons associated to the strong force. They only couple to particles with a colour charge. The mediators of the weak force are the massive charged $W^{\pm}$ and neutral Z^0 bosons that interact only with particles carrying a weak isospin and weak hypercharge, respectively. The massless photon (γ) mediates the electromagnetic force that only couples to particles having an electric charge. The last two interactions can be combined in the electroweak unification [37–39].
The other elementary particles are twelve fermions with spin 1/2, which can be further divided into six quarks and six leptons according to their coupling behaviour. Generally speaking, both quarks and leptons can be further sub-divided into three families or generations with two particles each. The first generation comprises the lightest elementary particles with higher generations being a higher mass copy of the first generation, but being otherwise identical. As a result, elementary particles of higher families decay into the particles of the first generation, meaning the elementary particles in the first generation are stable and make up our ordinary matter.

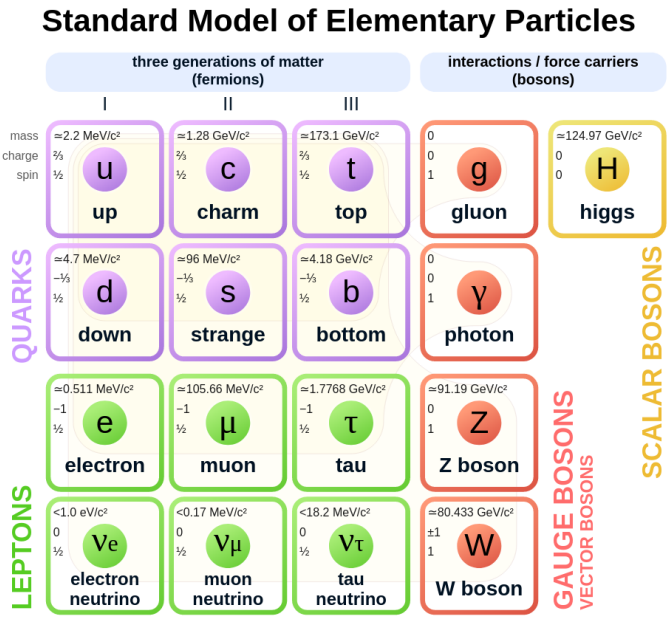

Figure 2.1.: Schematic overview of the SM with the fermions on the left-hand side and the bosons on the right-hand side. Shown are the masses of the individual elementary particles, their charges and the spin. ©Wikimedia Commons

To each particle there exists an anti-particle that has the same mass, but e.g. opposite electric charge.
The quarks (q) are elementary particles with a colour charge and couple to all of the three forces described by the SM.
The first generation of quarks consists of an up (u) and a down (d) quark with a fractional electric charge of $Q_u = +\frac{2}{3}e$ and $Q_d = -\frac{1}{3}e$. The charm (c) and the strange quark (s) make up the second generation. The third family contains the heaviest elementary particle, the top (t) quark, and its isospin partner, the bottom (b) quark.
Due to the fact that all quarks carry a colour charge, they are confined, meaning that they form a bound state that is colourless. These colourless states are called hadrons. Only the t quark is so heavy that it decays before it can hadronise. The hadrons can either be a combination of a quark and an anti-quark, where the anti-particle has the same mass as the particle, but opposite quantum numbers such as the electric charge. The bound states with $q\ \bar{q}$ are called mesons. Baryons are hadrons with three quarks ($q\ q\ q$) or three anti-quarks respectively. Both these hadrons have integer elementary charge.
In addition to baryons and mesons there exist the hypothesis of pentaquarks, consisting of four quarks and an anti-quark. The existence of these states has been claimed by e.g. the LHCb collaboration [59, 60]. Besides, there might be bound states containing two quark- anti- quark pairs, called tetraquarks, where the most recent result from LHCb can

be found in [61].
Compared to the quarks, a family of leptons consists of a charged particle and a corresponding neutral particle, the neutrino. In the SM the neutrinos are assumed to be massless. This is however not the case as already seen in neutrino oscillations, the first hint of which was already found in 1968 [62].
The first generation of leptons contains the electron (e^-) and electron-neutrino (ν_e). The muon (μ^-) and the muon-neutrino (ν_μ) make up the second generation. The third generation is composed of the tau (τ^-) and the tau-neutrino (ν_τ).
The only particle not yet described is the Higgs boson. It is a spin-0-particle and without it, the mass terms of all particles would break local gauge invariance, the basic principle of the SM. Therefore, its discovery at the Large Hadron Collider (LHC) [48, 49] in 2012 was a huge milestone in particle physics.

2.1.1. Quantum Electrodynamics

Quantum Electrodynamics (QED) [18–27] describes electromagnetic interactions which are mediated by photons that couple to all electrically charged particles. It is mathematically represented by the unitary group of order 1, $\mathrm{U}(1)_{\mathrm{EM}}$, and is the only interaction of the SM with unlimited range in vacuum.
The Lagrangian for an electromagnetic interaction with a massive fermion ψ and a massless spin-1 photon field A^μ is given by:

$$\mathcal{L}_{\mathrm{QED}} = \bar{\psi}(x)(i\gamma^\mu \mathrm{D}_\mu - m)\psi(x) - \frac{1}{4}F^{\mu\nu}F_{\mu\nu} \tag{2.1}$$

$$= \bar{\psi}(x)(i\gamma^\mu \partial_\mu - m)\psi(x) + g_e\bar{\psi}\gamma^\mu\psi A_\mu - \frac{1}{4}F^{\mu\nu}F_{\mu\nu}, \tag{2.2}$$

with $\mathrm{D}_\mu = \partial_\mu - ig_eA_\mu$ being the covariant derivate. This is introduced to keep the $U(1)_{EM}$ invariance, which then leads to a coupling between the photon field and the electric charge. $\bar{\psi} = \psi^\dagger\gamma^0$ is the adjoint spinor, γ^μ are the Gamma matrices, m corresponds to the particle mass, $F_{\mu\nu} = \partial_\mu A_\nu - \partial_\nu A_\mu$ represents the field strength tensor and considering the Einstein summation convention.
In eq. (2.2) the first term represents the free fermion field, whereas the second term reflects the interaction between fermions and photons with a coupling strength of g_e. The third and last term stands for the free photon field.
However, self-couplings of the photon are not possible as it does not have an electric charge.
Aforementioned, QED is described by $\mathrm{U}(1)_{\mathrm{EM}}$ under which its Lagrangian is also invariant with a phase $\alpha(x)$, where x is dependent on space-time. The $U(1)_{EM}$ transformation is given by:

$$\psi(x) \to \psi'(x) = e^{i\alpha(x)}\psi(x) \text{ and } A_\mu \to A'_\mu = A_\mu + \frac{1}{g_e}\partial_\mu\alpha. \tag{2.3}$$

2.1.2. Quantum Chromodynamics

The quantum field theory used to explain the strong interaction is Quantum Chromodynamics (QCD) [30–32]. The strong interaction is mediated by gluons that couple to the colour charge, similar to the electric charge in QED.
The colour was historically introduced to account for an additional degree of freedom for the overall wave function of the Δ^{++} baryon. The Δ^{++} consists of three identical u quarks with a total spin of $J = 3/2$. As the quarks are fermions, they need to satisfy the Pauli exclusion principle. This means that for indistinguishable fermions, the state should be antisymmetric for the interchange of any two quarks. Nonetheless, the components of the wave function for the spin, the flavour and space are symmetric. Thus, an additional component was needed and introduced, the colour. The resulting overall wave function is therefore asymmetric again.
The colour charge has three discreet values and they are called, for visual purposes only: *red*, *green* and *blue*.
QCD can mathematically be expressed in a non-Abelian Lie Group $\mathrm{SU(3)_C}$, where the C in the subscript stands for the colour charge. The special unitary group of dimension three has eight generators, where each generator corresponds to one gluon. The resulting Lagrangian is given by the following expression:

$$\mathcal{L}_{\mathrm{QCD}} = i \sum_q \bar{\psi}_q \gamma^\mu \mathrm{D}_\mu \psi_q - \sum_q m_q \bar{\psi}_q \psi_q - \frac{1}{4} G^a_{\mu\nu} G^{a\mu\nu}. \tag{2.4}$$

Analogously to QED, ψ_q and m_q are the spinor field and the mass of the quark q.
The covariant derivative for the $\mathrm{SU(3)_C}$ is defined as:

$$\mathrm{D}_\mu = \partial_\mu - \frac{i}{2} g_\mathrm{s} \lambda^a \mathcal{G}^a_\mu. \tag{2.5}$$

Here, $\mathcal{G}^a_\mu$ denotes the eight gauge fields, corresponding to the eight gluons. Therefore, a, the colour index, can have any value between one and eight. λ^a are the generators of the $\mathrm{SU(3)_C}$ and are expressed by the Gell-Mann matrices [63]. Thus, $\lambda^a \mathcal{G}^a_\mu$ can be thought of as a rotation of the colour space defined by $\mathrm{SU(3)_C}$. Besides, $g_\mathrm{s} = \sqrt{4\pi\alpha_\mathrm{s}}$ is the dimensionless coupling strength for the strong interaction.
The field strength tensor $G^a_{\mu\nu}$ for the gluon field $\mathcal{G}^a_\mu$ can be expressed by:

$$G^a_{\mu\nu} = \partial_\mu \mathcal{G}^a_\nu - \partial_\nu \mathcal{G}^a_\mu - g_\mathrm{s} f_{abc} \mathcal{G}^b_\mu \mathcal{G}^c_\nu, \tag{2.6}$$

with f_{abc} being the structure constants of the $\mathrm{SU(3)_C}$.
The Lagrangian in its form in eq. (2.4) is invariant under local $\mathrm{SU(3)_C}$ gauge transformations.
In eq. (2.4), the first term is similar to the terms in eq. (2.2) for the QED Lagrangian. It describes the free propagation of the quarks and additionally the interaction between gluons and quarks. The second term is the mass term for the corresponding quark q. The last term accounts for the free gluon propagation and self-couplings of the gluon, meaning three and four gluon vertices.

Due to the self-coupling of the gluons, the strong interaction is special in many ways. For an infinite number of self-interactions of the gluons, the strong coupling constant g_s, contrary to what its name suggests, is not a constant any more, but rather changes it values. For smaller energies the coupling strength effectively increases and strong interactions cannot be calculated using perturbation theory any more. In contrast, for the high energy regime, the coupling strength decreases and the quarks and gluons can be considered as being asymptotically free particles [53, 54], making it possible to use perturbation theory again.
The two effects that are responsible for the running of the coupling constant are: firstly the shielding effect between a $q\overline{q}$ pair to reduce the coupling constant and secondly the opposite effect arising because of the colour charge of the gluon, called anti-screening. For large distances or small energies the effect of the gluons surpasses the effect of the $q\overline{q}$ pair increasing the strong coupling strength.
This directly links to colour confinement, which explains why no coloured objects can be found in nature and only hadronised quarks in form of bound states, the hadrons, can be observed.

2.1.3. Weak Interaction and Electroweak Unification

Initially, the electromagnetic and the weak interaction were described by two disjoint theories, quantum electrodynamics and quantum flavourdynamics. However, due to the similarity of the currents of these two interactions, Glashow, Weinberg and Salam [37–39] proposed a single Yang-Mills field with a $\mathrm{SU(2)_L} \times \mathrm{U(1)_Y}$ Lie group.
The $\mathrm{SU(2)_L}$ group introduces the three gauge fields W_μ^i $(i = 1, 2, 3)$ with the gauge coupling constant g and the generator I, which corresponds to the weak isospin. The L in the subscript refers to the left-handed fields.
The weak interaction distinguishes between left-handed and right-handed particles, due to the fact that the wavefunction of the fermions can be split into just these two components, left-handed and right-handed.
One additional field B_μ is introduced via the $\mathrm{U(1)_Y}$ group with the gauge coupling constant g' and Y being the generator of the group. Y is called the hypercharge and defined as: $Y = 2(Q - I_3)$ with Q being the electromagnetic charge.
The physical boson field for the photon (A) and the Z^0 boson can be connected to the gauge group boson fields by using $\theta_W = \tan^{-1}\left(\frac{g}{g'}\right)$, the weak mixing or Weinberg angle:

$$\begin{pmatrix} A \\ Z^0 \end{pmatrix} = \begin{pmatrix} \cos\theta_\mathrm{W} & \sin\theta_\mathrm{W} \\ -\sin\theta_\mathrm{W} & \cos\theta_\mathrm{W} \end{pmatrix} \begin{pmatrix} B \\ W^3 \end{pmatrix}. \tag{2.7}$$

The fields for the observed $W^\pm$ bosons are related to the gauge boson fields via:

$$W^\pm = \frac{1}{\sqrt{2}}(W^1 \mp iW^2). \tag{2.8}$$

To generate the masses of the fermion and weak isospin fields and preserve gauge invariance, the Higgs field is needed. It was introduced by Higgs, Englert and Brout and is

therefore called Brout-Englert-Higgs mechanism [64,65]. The ground state of the Higgs field spontaneously breaks the electroweak gauge symmetry. In this case the excitation of the additional field corresponds to a scalar particle, the Higgs boson. The Higgs field is added as a complex scalar SU(2) doublet $\phi = (\phi^+, \phi^0)$ with the potential $V(\phi)$. Here, the parameters of the potential are chosen in such a way that the vacuum expectation value v is not equal to zero and the electroweak gauge symmetry is broken in the minimum, but the Lagrangian is kept symmetric. At the end, only the physical Higgs scalar $\phi = h$ remains. For this, Higgs, Englert and Brout received the Nobel Prize in 2013 after experiments confirmed its existence.
The Lagrangian for the electroweak interaction, using the $\mathrm{SU(2)_L \times U(1)_Y}$ gauge groups and the Higgs mechanism, can be written as:

$$\mathcal{L}_{\mathrm{EW}} = \underbrace{\sum_i \bar{\psi}_i \left(i\gamma^\mu \partial_\mu - \frac{m_i h}{v} \right) \psi_i}_{\text{fermion kinematics + Yukawa term}} \tag{2.9}$$

$$\underbrace{-\frac{g}{2\sqrt{2}} \sum_i \bar{\psi}_i \gamma^\mu \left(1 - \gamma^5\right) \left(T^+ W_\mu^+ + T^- W_\mu^- \right) \psi_i}_{\text{weak charged current}} \tag{2.10}$$

$$\underbrace{-e \sum_i Q_i \bar{\psi}_i \gamma^\mu \psi_i A_\mu}_{\text{electromagnetic current}} \tag{2.11}$$

$$\underbrace{-\frac{g}{2\cos\theta_W} \sum_i \bar{\psi}_i \gamma^\mu \left(g_{\mathrm{V}}^i - g_{\mathrm{A}}^i \gamma^5 \right) \psi_i Z_\mu}_{\text{weak neutral current}} \tag{2.12}$$

$$\underbrace{+|D_\mu h|^2 - V(h)}_{\text{Higgs kinematics + potential}} \tag{2.13}$$

$$\underbrace{-\frac{1}{4} B_{\mu\nu} B^{\mu\nu} - \frac{1}{4} \mathrm{tr}\left(W_{\mu\nu} W^{\mu\nu} \right)}_{\text{gauge field kinematics}} \tag{2.14}$$

$$\underbrace{+\left(\frac{g^2}{2} v h + \frac{g^2}{4} h^2 \right) \left(W_\mu^+ \; W^{-\mu} + \frac{1}{2 \; \cos^2(\,\theta_{\mathrm{W}})} Z_\mu \; Z^\mu \right)}_{\text{Higgs interaction with gauge vector bosons}} \tag{2.15}$$

$$\underbrace{+\mathcal{L}_{\mathrm{WWV}}}_{\text{Gauge boson three-point self interactions}} \tag{2.16}$$

$$\underbrace{+\mathcal{L}_{\mathrm{WWVV}}}_{\text{Gauge boson four-point self interactions}} \; . \tag{2.17}$$

The sum of all the individual terms run over all the fermions i. $T^{\pm}$ are the lowering and raising operators for the weak isospin, which means that the weak isospin doublet partners are connected at the interaction vertex.
The electromagnetic coupling constant e corresponds to the elementary charge and is related to the coupling constant of the weak isospin fields g via $e = g \sin\theta_W$. The masses of the bosons are given by $M_W = \frac{1}{2} ev \sin\theta_W$ and $M_{Z^0} = \frac{1}{2} ev \sin\theta_W \cos\theta_W$, where v corresponds to the vacuum expectation value of the scalar Higgs field h and are generated by the coupling between Higgs and gauge boson fields. The mass of the photon $M_\gamma = 0$ after the symmetry breaking. The mass of the Higgs boson arises due to the parameter λ in its potential $V(\phi)$ with $M_h = \lambda v$.

2.1.4. Symmetries

Symmetries are an important concept in physics to provide a basic way for the explanation of physics laws. A symmetry corresponds to an operation on a system, which leaves the system unchanged. This means that the transformed system is indistinguishable from the original one.
In the context of classical physics this corresponds to continuous transformations like translations in space, time or rotations.
The importance of the symmetries is stated in Noether's theorem [66], which relates continuous symmetries to conservation laws. In case of classical physics: energy, momentum and angular momentum conservation.
The three major discrete symmetries in particle physics are parity (P), charge conjugation (C) and time reversal (T). All of these symmetries invert a certain physical quantity. Applying the symmetry operators twice returns the original state of the system. If $X \in \{P, C, T\}$ the following identify holds that:

$$X^2 = I, \tag{2.18}$$

where I is the identity operator.

Parity The parity operator (P) performs an inversion in space, meaning that it mirrors the spatial components at the origin: $P(\vec{x}) = -\vec{x}$. After the application of the parity operator, the helicity of the particle is changed. The helicity projects the particles spin onto the particles direction of motion. In case the spin and the motion direction point into the same direction (parallel), the particle is called right-handed, whereas if they are anti-parallel it is referred to as left-handed.
The angular momentum of the particle, however, stays unchanged under parity operations and is therefore called a pseudoscalar.
The application of the parity operator on a fermion yields again the fermion with eigenvalue $+1$ ($P|f\rangle = +|f\rangle$) and respectively $P|\bar{f}\rangle = -|\bar{f}\rangle$ for the anti-fermion. For hadrons the components are multiplied with an additional orbital angular momentum part.

Charge Conjugation The charge conjugation operator (C) does not only change the electric charge as the name suggests, but also all other additive quantum numbers such as flavour and colour charge. This changes a particle into its anti-particle ($C|t\rangle = |\bar{t}\rangle$). The only particles that are eigenstates of this operator are a few neutral particles (e.g. γ, π^0, η, J/ψ,...) so particles that are also their anti-particle.

Time Reversal The time reversal operator (T) exchanges an incoming particle into an outgoing particle in a reaction. This operator has no particles that are eigenstates.

CPT The effect of C, P and T together is a fundamental theorem of quantum field theory, the CPT theorem [67]. If this combination would not be conserved, it would mean that Lorentz invariance is violated and the masses of particles and anti-particles are not identical.

2.1.5. Symmetry violations

In electromagnetic and strong interactions the three discrete symmetries are individually conserved. This was also assumed for the weak interaction, but Wu [68] showed that parity is maximally violated. To test this, the beta decay of spin polarised cobalt nuclei was investigated:

$$^{40}\mathrm{Co} \rightarrow ^{40}\mathrm{Ni} + e^- + \bar{\nu}_e. \tag{2.19}$$

As the angular momentum is conserved, the electron and the electron-anti-neutrino are emitted along the polarisation axis. If P was conserved in the weak interaction, the electron would be emitted equally in alignment with the Cobalt spin axis and opposite to it. However, it was observed that the electron was only emitted anti-parallel to the spin axis, meaning that all electrons were left-handed. This means that the weak interaction has a preferred handedness.
After the discovery of the parity violation, it can directly be concluded that also the charge conjugation symmetry is not conserved. This can be seen in, for example, the charged pion decay:

$$\pi^+ \rightarrow \mu^+ \nu_\mu. \tag{2.20}$$

The charged pion is a spin-0 particle and due to conservation of angular momentum, the decay products need to have the same handedness.
This however means that the (nearly massless) neutrino needs to be left-handed for the weak interaction to couple to it. So the anti-muon is also left-handed in the pion rest frame. If one would now apply the charge conjugation operator, the result would be:

$$\pi^- \rightarrow \mu^- \bar{\nu}_\mu. \tag{2.21}$$

Angular momentum is still a conserved quantity, which means that the μ^- and the $\bar{\nu}_\mu$ would still be left-handed. This, however, was not what was measured experimentally. The measured helicity of the μ^- was right-handed, which is also the handedness for the

$\bar{\nu_\mu}$.
A right-handed particle μ^- and a left-handed anti-particle μ^+ seems to be a contradiction to Wu's observation of maximal parity violation in weak interactions.
This can be explained as the chirality is a Lorentz-invariant quantity, whereas helicity is not. For massless particles the chirality and the helicity are equal, whereas for massive particles this is not the case. There always exists another reference frame that is moving faster than the particle, reversing its helicity.
The coupling to the "wrong" handedness is highly suppressed for lower masses, which also explains why the charged pion prefers to decay into the μ instead of the lighter e.
If one would now apply the parity operator on the π^- again, the handedness would also be changed and it was assumed that at least CP would be a conserved quantity in the weak interaction.
This was tested by Cronin and Fitch [69] in 1964 using the neutral Kaon system. The strong eigenstates $K^0(u\bar{s})$ and $\overline{K}^0(\bar{u}s)$ can convert into each other via so called box diagrams, which results in a mixed state.
The strong eigenstates for the neutral kaon do not correspond to the CP eigenstates. The application of the CP operators on the strong eigenstates are given by:

$$CP|K^0\rangle = +|\overline{K}^0\rangle \tag{2.22}$$

$$CP|\overline{K}^0\rangle = -|K^0\rangle. \tag{2.23}$$

An arbitrary mixed state can generally be written as:

$$|\pm\rangle = N(p|K^0\rangle \pm q|\overline{K}^0\rangle), \tag{2.24}$$

where N is the normalisation and p and q correspond to the fraction of K^0 and $\overline{K}^0$ states. As a result, the CP eigenstates can be written as:

$$|K_1\rangle = \frac{1}{\sqrt{2}}\left(|K^0\rangle + |\overline{K}^0\rangle\right) \tag{2.25}$$

$$|K_2\rangle = \frac{1}{\sqrt{2}}\left(|K^0\rangle - |\overline{K}^0\rangle\right), \tag{2.26}$$

where the CP eigenvalue for K_1 would be $+1$ and -1 for the K_2. The K_1 would decay into two pions, whereas the CP odd state would decay into three pions. This particle would be longer-lived as it has less phase-space available compared to the CP even state. Therefore, Cronin and Fitch proposed an experiment, where a beam of neutral Kaons was left to travel a long distance for the short-lived component to decay, so that only the long-lived component was left. The results of the experiment showed, however, that there were still a few Kaons decaying into the two pion state and not as assumed only into the three pion final state. This can be explained by e.g. that the CP eigenstate K_2 does not exactly correspond to the long-lived state K_L^0 but rather also has a small contribution from the other CP eigenstate K_1:

$$|K_L^0\rangle = \frac{1}{\sqrt{1+|\epsilon|^2}}\left(|K_2\rangle + \epsilon|K_1\rangle\right). \tag{2.27}$$

The ϵ parameter, which measures the strength of CP violation due to mixing, was found to be $|\epsilon| = (2.228 \pm 0.011) \cdot 10^{-3}$ [70].
In general, for this type of CP violation the decay rates for particle and anti-particle are the same, the CP violation occurs via mixing as the oscillation rate is not equal going both directions. This results in a difference in CP and weak eigenstates, meaning that $|\frac{q}{p}| \neq 1$.
This kind of CP violation can also be analysed in an asymmetry of the time-dependent $\frac{\mathrm{d}\Gamma}{\mathrm{d}t}$ decay rates, defined as:

$$A_{SL} := \frac{\frac{\mathrm{d}\Gamma}{\mathrm{d}t}(\bar{I}^0_{\mathrm{phys}}(t) \to \ell^+ X) - \frac{\mathrm{d}\Gamma}{\mathrm{d}t}(I^0_{\mathrm{phys}}(t) \to \ell^- X)}{\frac{\mathrm{d}\Gamma}{\mathrm{d}t}(\bar{I}^0_{\mathrm{phys}}(t) \to \ell^+ X) + \frac{\mathrm{d}\Gamma}{\mathrm{d}t}(I^0_{\mathrm{phys}}(t) \to \ell^- X)} = \frac{1 - |\frac{q}{p}|^4}{1 + |\frac{q}{p}|^4}, \tag{2.28}$$

where I^0_{phys} is an initial, mixed state and $\bar{I}^0_{\mathrm{phys}}$ the corresponding initial anti-particle. To experimentally determine the decaying flavour, semi-leptonic decays of the charge-conjugated partner are used, as the flavour can be directly inferred by the charge of the final state charged lepton in the decay.
This kind of CP violation is time dependent, but the asymmetry is not, as can be seen in eq. (2.28). It is constant and only depends on the two factors q and p.
The second type of CP violation, called direct CP violation, manifests itself in different decay rates if all particles in a reaction are exchanged by their anti-particles:

$$\mathcal{B}(I \to f) \neq \mathcal{B}(\bar{I} \to \bar{f}). \tag{2.29}$$

For the decay amplitude A_f the particle I decays into the final state f and for $\bar{A}_{\bar{f}}$ all particles are replaced by their corresponding anti-particle. When direct CP violation occurs $|\bar{A}_{\bar{f}}/A_f| \neq 1$, it means that the decay amplitudes are not invariant under the exchange of particles with their corresponding anti-particles.
The effect of direct CP violation is about three orders of magnitude smaller than the mixing effect in the neutral kaon system, if ϵ' is the size of the direct CP violation $\frac{\epsilon'}{\epsilon} = (1.66 \pm 0.23) \cdot 10^{-3}$ [70].
Contrary to mixing, the direct CP violation is also possible for charged hadrons. The fully time dependent asymmetry for a general decay of a charged hadron I into the final state f is given by:

$$A_{f^\pm} := \frac{\Gamma(I^- \to f^-) - \Gamma(I^+ \to f^+)}{\Gamma(I^- \to f^-) + \Gamma(I^+ \to f^+)} = \frac{|A^-_{f^-}/A_{f^+}|^2 - 1}{|A^-_{f^-}/A_{f^+}|^2 + 1}. \tag{2.30}$$

The third and last type of CP violation is called CP violation in interference between decay and mixing and is only possible for neutral mesons again. In this interference process the decay of the neutral particle I^0 can either directly proceed into the final state f or it can occur via mixing $I^0 \to \bar{I}^0 \to f$. The final state f however needs to be reachable by both particles I^0 and $\bar{I}^0$, making it a CP eigenstate. Thus, the asymmetry for the decay into the CP eigenstate f_{CP} can be defined as:

$$A_{f_{CP}}(t) := \frac{\frac{\mathrm{d}\Gamma}{\mathrm{d}t}(\bar{I}^0_{\mathrm{phys}}(t) \to f_{CP}) - \frac{\mathrm{d}\Gamma}{\mathrm{d}t}(I^0_{\mathrm{phys}}(t) \to f_{CP})}{\frac{\mathrm{d}\Gamma}{\mathrm{d}t}(\bar{I}^0_{\mathrm{phys}}(t) \to f_{CP}) + \frac{\mathrm{d}\Gamma}{\mathrm{d}t}(I^0_{\mathrm{phys}}(t) \to f_{CP})}. \tag{2.31}$$

This type of time-dependent CP violation is the main source of CP violation in the system of B mesons. There exist four different kinds of B mesons, the $B_d^0(d\bar{b})$, the $B_u^+(u\bar{b})$, the $B_s^0(s\bar{b})$ and the $B_c^+(c\bar{b})$. The first two B mesons B_d^0 and B_u^+ are usually shortly referred to as B^0 and B^+. The masses of these mesons are quite large, which yields many possible different decay channels. This is useful in many aspects, as this can be exploited to test the SM or detect deviations from it.
B^0 mesons are neutral particles and thus can oscillate. The physical eigenstates of the neutral B meson have nearly the same life time, however they differ in their masses.
As already explained above, to measure CP violation in the interference between decay and mixing, the B^0 and the $\overline{B}^0$ meson both need to be able to reach the same final state. In the case of the B meson the investigated CP eigenstate is $J/\psi K_S^0$. In this case, the asymmetry simplifies to:

$$A_{J/\psi K_S^0}(t) = \sin(\Delta m t)\sin(2\beta), \tag{2.32}$$

with t being the time between the tagging of one of the B mesons as either being B^0 or $\overline{B}^0$ and the observation of the decay $B \to J/\psi K_S^0$. Generally in experiments, where this measurement is performed, B mesons are produced in $B\overline{B}$ pairs.
To determine the flavour of the B meson not decaying to the $J/\psi K_S^0$ usually semi-leptonic decays are considered as the charge of the charged lepton is directly linked to the flavour of the B meson.
The $\sin(\Delta m t)$ in the formula corresponds to the oscillation between B^0 and $\overline{B}^0$ and Δm to the mass difference between the two physical neutral B meson states.
A measurement in this way is only possible, because the B mesons are produced in a coherent state. In this context coherent state means if one of the B mesons decays into a flavour eigenstate the flavour of the other B meson is fixed at this point in time. This fact is what makes the measurement possible in the first place.
However, the other B meson can still oscillate. This difference between the direct decay and the mixing introduces a phase difference of 2β. If one would integrate the CP violation over time, it would vanish. Therefore, time dependent measurements are needed.
Now that CP is also violated, CPT is required to hold. In this case the proof of CP violation directly links to the violation of T, which was soon after discovered to be broken [71].

2.1.6. CKM Matrix

In the 1960's, measurements suggested that the coupling of the $W^\pm$ bosons to a charged lepton-neutrino pair is the same for all three generations of leptons, which is referred to as lepton universality. The same behaviour was expected for the quarks with the $W^\pm$ boson coupling to a u and a d type quark pair.
This was however not what was measured. The decay rate for $\pi^-(u\bar{d}) \to \mu^-\bar{\nu}_\mu$ compared to $K^-(u\bar{s}) \to \mu^-\bar{\nu}_\mu$ is approximately 20 times higher than what would have been expected for a universal coupling to the quarks.
This problem was solved by Nicola Cabibbo [72] in 1963 by introducing the concept of

quark mixing. This means that the weak eigenstates that couple to the $W^{\pm}$ boson are superpositions of the mass eigenstates of the quarks.
The quark mixing relates the mass eigenstates of the d and s quarks in the weak current via a 2×2 rotation matrix:

$$\begin{pmatrix} d' \\ s' \end{pmatrix} = \begin{pmatrix} \cos\theta_{\mathrm{c}} & \sin\theta_{\mathrm{c}} \\ -\sin\theta_{\mathrm{c}} & \cos\theta_{\mathrm{c}} \end{pmatrix} \begin{pmatrix} d \\ s \end{pmatrix}. \tag{2.33}$$

This matrix allows for mixing between the first and the second generation of the quarks with the only parameter in the 2×2 rotation matrix being the strength of the mixing θ_{C}, the Cabibbo angle.
In 1970 Glashow, Iliopoulos and Maiani proposed the GIM-mechanism [73] to explain the much lower observed branching ratio of the $K_L^0 \to \mu^- \mu^+$ compared to only considering ud and us couplings. It postulated another, at that time unknown, fourth quark, the c quark. Therefore, the decay $K_L^0 \to \mu^- \mu^+$ is also possible via the exchange of a virtual c quark in the box diagram, which negatively interferes with the box diagram including a u quark.
Nonetheless, the Cabibbo angle cannot explain the CP violation observed in the SM. Therefore, an extension to three generations was proposed by Kobayashi and Maskawa in 1973: the Cabibbo-Kobayashi-Maskawa (CKM)-mechanism [74]. This unitary 3×3 matrix relates the weak eigenstates $\begin{pmatrix} d' & s' & b' \end{pmatrix}$ to the mass eigenstates $\begin{pmatrix} d & s & b \end{pmatrix}$:

$$\begin{pmatrix} d' \\ s' \\ b' \end{pmatrix} = V_{\mathrm{CKM}} \begin{pmatrix} d \\ s \\ b \end{pmatrix} = \begin{pmatrix} V_{\mathrm{ud}} & V_{\mathrm{us}} & V_{\mathrm{ub}} \\ V_{\mathrm{cd}} & V_{\mathrm{cs}} & V_{\mathrm{cb}} \\ V_{\mathrm{td}} & V_{\mathrm{ts}} & V_{\mathrm{tb}} \end{pmatrix} \begin{pmatrix} d \\ s \\ b \end{pmatrix}. \tag{2.34}$$

The magnitudes of the elements of the CKM matrix can only be determined experimentally, the latest values are [70]:

$$|V_{\mathrm{CKM}}| = \begin{pmatrix} 0.97373 \pm 0.00031 & 0.2243 \pm 0.0008 & 0.00382 \pm 0.00020 \\ 0.221 \pm 0.004 & 0.975 \pm 0.006 & 0.0408 \pm 0.0014 \\ 0.0086 \pm 0.0002 & 0.0415 \pm 0.0009 & 1.014 \pm 0.029 \end{pmatrix}. \tag{2.35}$$

It can be seen that the coupling of quarks within the same generation are highly preferred over couplings to other generations.
A unitary $N \times N$ matrix has $N(N-1)/2$ real parameters and $(N-1)(N-2)/2$ phases. In case of the CKM matrix, this results in three rotation angles and one complex phase δ. Thus the CKM matrix can be parametrised as [75]:

$$V_{\mathrm{CKM}} = \begin{pmatrix} 1 & 0 & 0 \\ 0 & c_{23} & s_{23} \\ 0 & -s_{23} & c_{23} \end{pmatrix} \begin{pmatrix} c_{13} & 0 & s_{13}e^{-i\delta} \\ 0 & 1 & 0 \\ -s_{13}e^{i\delta} & 0 & c_{13} \end{pmatrix} \begin{pmatrix} c_{12} & s_{12} & 0 \\ -s_{12} & c_{12} & 0 \\ 0 & 0 & 1 \end{pmatrix}, \tag{2.36}$$

where $c_{ij} = \cos(\theta_{ij})$ and $s_{ij} = \sin(\theta_{ij})$. By using this parametrisation, the coupling strength between the three quark generations can be related to the three angles. The

Cabibbo angle explained above corresponds to the angle θ_{12}. The phase δ enters the wave function of any particle undergoing an interaction involving the respective CKM matrix elements as $e^{i(\omega t+\delta)}$, which is not invariant under time reversal, and results in the introduction of CP violation in the SM.
Another widely used parametrisation of the CKM matrix is the Wolfenstein parametrisation [76]. It uses a Taylor expansion of $\lambda = \sin(\theta_{12})$, with terms of up to order λ^3, it yields:

$$V_{\mathrm{CKM}} \approx \begin{pmatrix} 1-\frac{1}{2}\lambda^2 & \lambda & A\lambda^3(\rho-i\eta) \\ -\lambda & 1-\frac{1}{2}\lambda^2 & A\lambda^2 \\ A\lambda^3(1-\rho-i\eta) & -A\lambda^2 & 1 \end{pmatrix} + O(\lambda^4)\ . \tag{2.37}$$

The strength of CP violation arises due to $\rho - i\eta$ in the CKM matrix elements V_{ub} and V_{td}.
To test the CKM mechanism, the unitarity of the V_{CKM} matrix can be used. It imposes restrictions that need to be fulfilled by the matrix elements, meaning:

$$\sum_i V_{ij}V_{ik}^* = \delta_{jk}, \tag{2.38}$$

$$\sum_j V_{ij}V_{kj}^* = \delta_{ik}. \tag{2.39}$$

The relations summing to zero represent triangles in the complex plane, called unitary triangles. These triangles are over-constraint as the length of the sides and the three angles are measured independently. If the CKM matrix would not be unitary this would for example be a hint for additional quark generations or physics beyond the SM.
In total there exist six triangles with the same area, where the area is a measure for the amount of CP violation present in the SM.
The unitary triangle most commonly used is given by the relation:

$$V_{\mathrm{ud}}V_{\mathrm{ub}}^* + V_{\mathrm{cd}}V_{\mathrm{cb}}^* + V_{\mathrm{td}}V_{\mathrm{tb}}^* = 0. \tag{2.40}$$

All sides have the same order λ^3 in the Wolfenstein parametrisation. Thus, eq. (2.40) is usually normalised to the bottom side with the corners being at (0,0) and (0,1). The apex of the triangle is a measure for the size of the CP violation. In fig. 2.2 a sketch of this unitary triangle can be seen. The most recent measurements for the angles and the length of the triangle sides are summarised by the CKMfitter group [77] in fig. 2.3. Here, the measurement of $\sin(2\beta)$ in the decay $B \to J/\psi K_{\mathrm{S}}^0$ corresponds one of the angles in the unitary triangle.
All measurements are in good agreement with each other and therefore validate the unitarity of the CKM matrix.

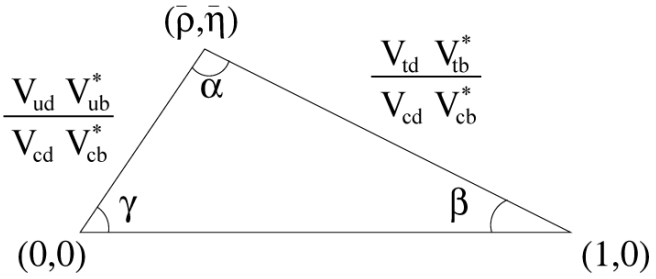

Figure 2.2.: Unitarity triangle for the b quark sector.

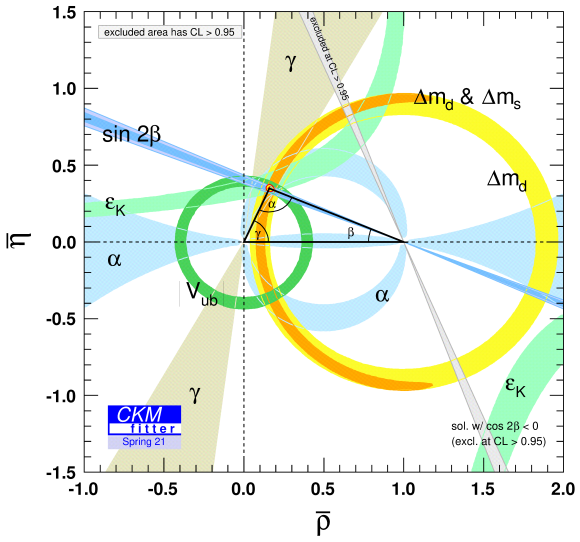

Figure 2.3.: Experimental measurements for the unitary triangle provided by the CKM-fitter group [77].

2.2. *B* mesons

The b quark is the heaviest quark that hadronises to form bound states. It was discovered in 1977 by the E288 experiment [40].
B mesons are the lightest particles containing a b quark and can therefore only decay via the weak force. This results in a relatively large lifetime as no strong decays are possible and the decay can only proceed via the fairly small CKM matrix elements V_{ub} and V_{cb}.
Depending on the resulting final state particles in the B meson decays, the decay modes can be classified into three main modes: hadronic, leptonic and semi-leptonic. The corresponding Feynman diagrams can be seen in fig. 2.4. The purely leptonic decay is only possible for charged B mesons in the SM.

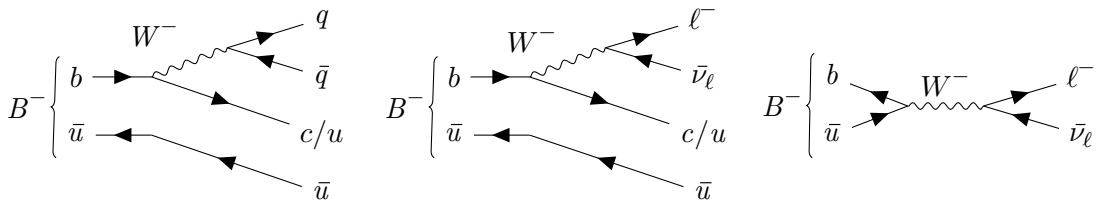

Figure 2.4.: Feynman diagrams showing, from left to right, the fully hadronic, semi-leptonic and purely leptonic decay for the B^- meson at tree level.

In case of a hadronic decay, all decay products of the B meson are hadrons or on fundamental level quarks and anti-quarks. For a purely leptonic decay of a B meson the decay products are a charged lepton and a neutrino. A mixture of both, i.e. quarks and anti-quarks as well as a charged lepton-neutrino pair are the signature for a semi-leptonic decay.
For both the hadronic and the semi-leptonic decay modes, the b quark either decays into a c or a u quark, however $|V_{\mathrm{cb}}| \gg |V_{\mathrm{ub}}|$ meaning that the decay into a charm is preferred due to the involved CKM matrix elements. Besides, the branching ratio for the hadronic decay modes is the highest as the W coupling ratio is biggest [70]. The hadronic decay is nonetheless particularly challenging as there are two CKM matrix elements involved: one in the production of the $W^{\pm}$ boson and the other one in the decay. Additionally, there are many quarks present in this reaction resulting in QCD effects that are theoretically hard to model.
Compared to that, the leptonic decays involve only one CKM matrix element in the production and no additional QCD effects for the decay products, as these are only leptons. However, these decays are helicity suppressed and thus have a low branching ratio. Purely leptonic B meson analyses therefore need a lot of experimental data.
In contrast to that, the semi-leptonic decay modes of the B meson also just have one CKM matrix element that contributes, like the leptonic decay modes. The leptons in the final state is not involved in strong interactions which significantly reduces the QCD

effects that play a major role in the hadronic decay modes. Besides, the decay rate for the semi-leptonic decays is in-between the leptonic and hadronic modes.
As mentioned above, for semi-leptonic decays there is the possibility of a $b \to u$ or $b \to c$ transition. The first kind of transitions are called charmless semi-leptonic decays and due to the quark changing flavour across two generations, the contribution is much smaller than the so called charm transitions.
The semileptonic B meson decays can however be used to determine $|V_{\mathrm{cb}}|$ and $|V_{\mathrm{ub}}|$. To do so, there exist different approaches either the inclusive and the exclusive measurement. In the inclusive measurement of $|V_{\mathrm{cb}}|$, all semi-leptonic decays containing mesons with a c quark (X_c) are considered. Whereas an exclusive measurement just focusses on one particular decay channel. The results of these two methods can be compared and a large deviation between the two approaches has been observed as shown in e.g. [78]. This tension is also seen, when the branching ratios of all measured exclusive decay rates are summed up, which should yield in principle the same value as the inclusive approach.

2.3. The $B \to D^{**}\ell\nu_\ell$ decay

The decay $B \to D^{**}\ell\nu_\ell$ is one of the possible semi-leptonic decay channels for the B meson [70] and may help to explain the difference between the sum of the exclusively measured decays and the inclusive $B \to X_c\ell\nu_\ell$ decays , see e.g. [78].
In addition, the uncertainty on the known branching ratio is one of the leading systematic uncertainties in the determination of the matrix elements $|V_{\mathrm{cb}}|$ and $|V_{\mathrm{ub}}|$ as stated in for example [79].
The D^{**} mesons are orbitally-excited p-wave (L=1) mesons that consist of a charm and a light quark.
According to Heavy Quark Effective Theory (HQET) [80], the dynamics of a meson can be described by a heavy quark, meaning c and b, that can be thought of as a static colour source to the light quark, here u, d and s. The mass of the heavy quark is irrelevant for the degrees of freedom of the light quark within the $Q\bar{q}$ system. Also, the dynamics stay unchanged under the exchange of heavy quark flavours, called heavy quark flavour symmetry. Besides, the heavy quark only interacts with gluons via the chromoelectric charge, which is spin independent. The resulting heavy quark spin symmetry means that the dynamics are unchanged under arbitrary transformations of the heavy quark spin.
Due to this Heavy Quark Spin Symmetry (HQSS) [81], the D^{**} mesons form a doublet of states with angular momentum $j = s_q + L$. Here, s_q corresponds to the spin of the light quark. Thus the hadronic state can be described only by the quantum number of the degrees of freedom of the light quark, as the dynamics are independent of the spin of the heavy quark.
For the orbital angular momentum case of $L = 1$, the total angular momentum, i.e. the total spin of the meson, parity and light quark angular momentum of the four D^{**} states are given by 0^+ and $j = 1/2$ for the D_0^*, 1^+ and $j = 1/2$ for the D_1', 1^+ and $j = 3/2$ for the D_1 and 2^+ and $j = 3/2$ for the D_2^*. The $j = 1/2$ states decay via the s-wave

component resulting in rather broad resonances, whereas the $j = 3/2$ states are narrow and decay in a d-wave with a typical decay width of about $20\,\mathrm{MeV}\,c^{-2}$ [82–84].
The D_0^* can decay into $D\pi$, the D_1' and the D_1 decay into $D^*\pi$ and the D_2^* can either decay into $D\pi$ or $D^*\pi$.
In fig. 2.5 the masses, the widths and the possible decay channels for the excited $c\bar{q}$ mesons can be seen.

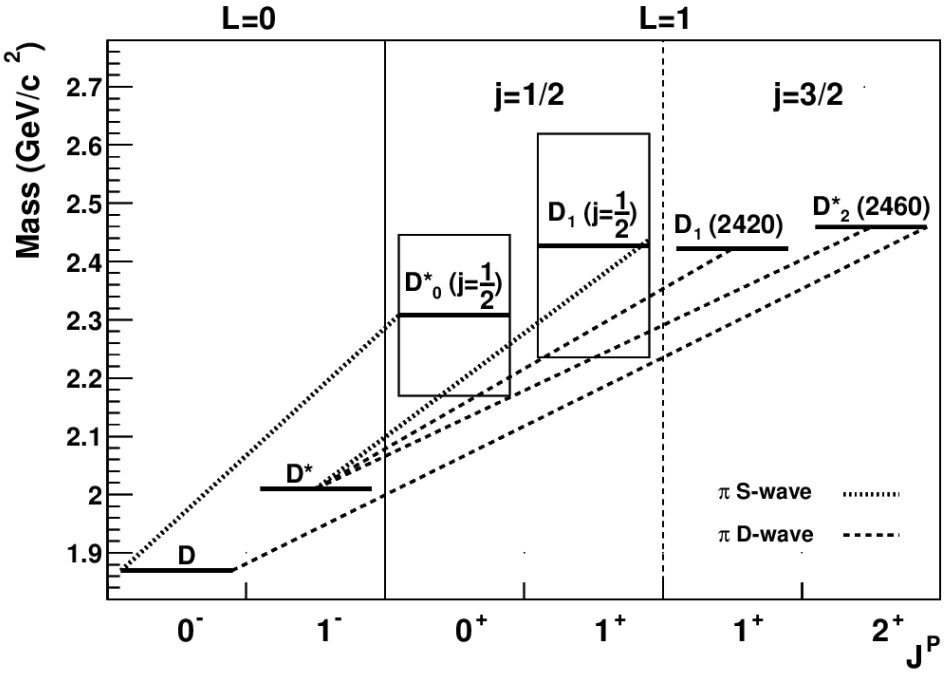

Figure 2.5.: Mass spectrum of the $c\bar{q}$ mesons, where the open box shows the width of the rather wide $j = 1/2$ states D_0^* and D_1'. The differently hashed lines visualise the possible pion transitions, which mostly occur via the strong interaction. Taken from [85].

The observed rates for the B mesons into the $j = 1/2$ states are similar to the rates into the $j = 3/2$ doublet, which is in disagreement with current model calculations [86, 87] that expect a smaller rate for $j = 1/2$ states.
Furthermore, there exists a problem with the D_0^* meson, which is usually parametrised as a single resonance, however several studies have shown that it seems to be an overlap of two states with different pole masses [88–90]. Therefore, a more complex function is required to describe the s-wave component instead of a Breit-Wigner distribution. There are various calculations that support this approach [91, 92].
Due to the very low decay rate, it is experimentally challenging to measure the branching ratio into any of the four D^{**} mesons individually. Therefore, a more inclusive approach

is used in the presented analysis where only the combined branching ratio into the direct decay products of the D^{**} mesons are measured. Hence, the branching ratios $B \to D^{(*)}\pi\ell\nu$ and $B \to D^{(*)}\pi\pi\ell\nu$ are determined.
There have been previous analyses by *BABAR* [84] and *Belle* [93, 94], but only using one charged pion in the final state. Additionally, there was a first measurement of D^{**} mesons into the two-pion state $D^{(*)}\pi\pi$ by *BABAR* [95] with limited statistics. A fairly recent measurement of the two-pion state has been performed at *Belle* [94]. In table 2.1 the previous measurements by *BABAR* and *Belle* are summarised.
This analysis presents the first measurement of the $B \to D^{**}\ell\nu_\ell$ branching ratio into the one pion state using Belle II data.

Decay channel	*BABAR*	*Belle*
$B^0 \to \overline{D}^0\pi^-\ell^+\nu_\ell$	$(0.43 \pm 0.08 \pm 0.03)\,\%$	$(0.360 \pm 0.018 \pm 0.011)\,\%$
$B^+ \to D^-\pi^+\ell^+\nu_\ell$	$(0.42 \pm 0.06 \pm 0.03)\,\%$	$(0.378 \pm 0.013 \pm 0.017)\,\%$
$B^0 \to \overline{D}^{*0}\pi^-\ell^+\nu_\ell$	$(0.48 \pm 0.08 \pm 0.04)\,\%$	$(0.551 \pm 0.024 \pm 0.017)\,\%$
$B^+ \to D^{*-}\pi^+\ell^+\nu_\ell$	$(0.59 \pm 0.05 \pm 0.04)\,\%$	$(0.530 \pm 0.019 \pm 0.025)\,\%$
$B^0 \to D^-\pi^+\pi^-\ell^+\nu_\ell$	$(0.127 \pm 0.039 \pm 0.026 \pm 0.007)\,\%$	$(0.145 \pm 0.018 \pm 0.013)\,\%$
$B^+ \to \overline{D}^0\pi^+\pi^-\ell^+\nu_\ell$	$(0.161 \pm 0.030 \pm 0.018 \pm 0.008)\,\%$	$(0.173 \pm 0.014 \pm 0.013)\,\%$
$B^0 \to D^{*-}\pi^+\pi^-\ell^+\nu_\ell$	$(0.138 \pm 0.039 \pm 0.030 \pm 0.003)\,\%$	$(0.051 \pm 0.021 \pm 0.009)\,\%$
$B^+ \to \overline{D}^{*0}\pi^+\pi^-\ell^+\nu_\ell$	$(0.080 \pm 0.040 \pm 0.023 \pm 0.003)\,\%$	$(0.070 \pm 0.015 \pm 0.008)\,\%$

Table 2.1.: Measurements of the branching ratios $B \to D^{(*)}\pi\ell\nu_\ell$ and $B \to D^{(*)}\pi\pi\ell\nu_\ell$ at *BABAR* [84, 95] and *Belle* [94]. Here, the first uncertainty is statistical, the second systematic and the third arises due to the normalisation mode.

CHAPTER 3

Experimental Setup

The investigated data used in this thesis was collected with the Belle II detector [96], which is the successor of the *Belle* detector [97] in Tsukuba, Japan. The *Belle* detector successfully collected data of $e^- e^+$ collisions between 1999 and 2010. It was located at the High Energy Accelerator Research Organisation (KEK). The achievements and results of the *Belle* experiment as well as the *BABAR* experiment are summarised in [98] and [99].
In 2018, Belle II started recording first collision data at the upgraded asymmetric KEKB accelerator, the SuperKEKB accelerator [100]. It is supposed to accumulate much more data to further study CP-violation by producing entangled and boosted B meson pairs in a clean experimental environment.
The following two sections will start by explaining the SuperKEKB accelerator in more detail, followed by the Belle II detector with comments about changes made to the previous *Belle* detector.

3.1. The SuperKEKB accelerator

The SuperKEKB accelerator is an asymmetric $e^- e^+$ collider, which is located at the KEK high energy research facility in Tsukuba in Japan. Being an upgraded version of one of the first B factories, KEKB [101], SuperKEKB is also designed to produce as many B mesons as possible to study CP-violation in the B system, probing its parameters and measuring rare decays.
The asymmetric $e^- e^+$ collider operates at a centre-of-mass energy of $\sqrt{s} = 10.58\,\text{GeV}$. This energy is on the mass of the $\Upsilon(4S)$ resonance, which is an excited $b\bar{b}$ bound state and almost exclusively ($\approx 96\,\%$ [70]) decays into a pair of neutral or charged B mesons. Due to the fact, that the mass of the $\Upsilon(4S)$ is just slightly above the mass of the two B mesons, the two produced B mesons are nearly at rest in the centre-of-mass system

(CMS). For measuring the spatial distance of the short-lived B mesons, to later measure the CP-violation, the CMS is boosted with respect to the laboratory system. For this reason, the energy of the electrons is chosen to be 7.0 GeV in the high energy ring (HER) and 4.0 GeV for the positrons in the low energy ring (LER). This results in a boost of $\beta\gamma \approx 0.287$ in the flight direction of the e^-.
To fill the two storage rings with electrons and positrons, a single linear accelerator is used. For the production of electrons, an electron beam gun is utilised. Some of these electrons are directly injected into the HER, whereas the other electrons need to strike a tungsten target for the production of the positrons. The positrons need to pass through a damping ring to reduce e.g. the emittance of the positron bunches, before being injected into the LER.
A schematic of the SuperKEKB accelerator, as well as comments about performed changes made to the predecessor, can be seen in Figure 3.1.

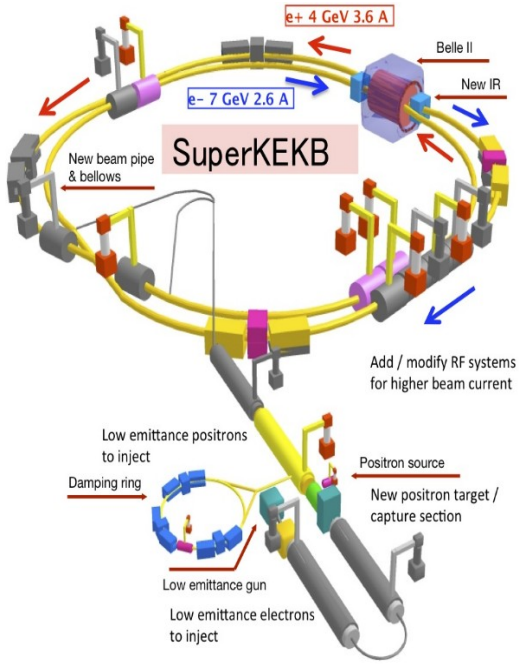

Figure 3.1.: A schematic drawing of the SuperKEKB accelerator in Tsukuba in Japan. SuperKEKB has two separate beam pipes, one to accelerate the electrons, the high energy ring (HER), and one to accelerate the positrons, the low energy ring (LER). At one of the two crossing points of the three kilometre long beam pipes, the Belle II experiment is positioned. ©Belle II

The boost for the KEKB accelerator, where the energy of the HER was 8.0 GeV and 3.5 GeV for the LER, respectively, was higher with approximately $\beta\gamma \approx 0.425$. Moreover, the instantaneous luminosity of the two accelerators is very different. The instantaneous

luminosity $\mathcal{L}$, used as a measure for the collider's performance, can be expressed in terms of the event rate $\frac{\mathrm{d}N}{\mathrm{d}t}$ and the corresponding cross section σ as:

$$\frac{\mathrm{d}N}{\mathrm{d}t} = \mathcal{L}\sigma.$$

The instantaneous luminosity is given by:

$$\mathcal{L} = \frac{N_{e^+} N_{e^-} f}{4\pi\sigma_x\sigma_y} R_L, \tag{3.1}$$

where σ_x and σ_y correspond to the horizontal and vertical size of the two beams with a Gaussian profile, N_{e^+} and N_{e^-} are the number of particles in a positron or electron bunch and f is the bunch crossing frequency. R_L is a correction factor which accounts for geometrical effects associated to the bunch length and the finite crossing angle.
As can be seen in Equation 3.1, one option to increase the instantaneous luminosity is to reduce the beam size at the collision point. This was done for the SuperKEKB accelerator as well as increasing the beam currents $I_{e^+/e^-} \propto N_{e^+/e^-} f$ compared to the KEKB accelerator by a factor of two. The idea to increase the beam currents and squeeze the beam size among others, was first proposed by P. Raimondi for the Italian super B factory [102] and is called "nano-beam" scheme. Using this approach, the design luminosity for the SuperKEKB accelerator is $8 \times 10^{35}\,\mathrm{cm}^{-2}\,\mathrm{s}^{-1}$ compared to the highest recorded peak luminosity for the KEKB accelerator of $2.11 \times 10^{34}\,\mathrm{cm}^{-2}\,\mathrm{s}^{-1}$.

3.2. The Belle II detector

The purpose of the Belle II detector, surrounding one of the two crossing points of the SuperKEKB accelerator, is to measure the decay products or final state particles of the two B mesons originating from the $\Upsilon(4S)$ resonance. The Belle II detector is composed of several subdetectors, each one measuring different properties of the final state particles such as charges or momenta.
Each subdetector will be explained in more detail in the following subsections. For further reading please refer to [96] and [103].
The subdetector being closest to the interaction point (IP) is the pixel detector (PXD), followed by the silicon vertex detector (SVD). These two tracking detectors are summarised as the overall vertex detector (VXD). Also part of the tracking system is the central drift chamber (CDC). All of these three subdetectors are immersed in a nearly homogeneous magnetic field along the beam direction with a field strength of 1.5 T. The superconducting solenoid magnet forces charged particles onto a bent trajectory.
To distinguish between kaons and pions, a time-of-propagation counter (TOP) in the barrel region and an aerogel ring imaging Čerenkov detector (ARICH) in the forward endcap region are included. For measuring the energy of the neutral photons as well as the charged electrons and positrons, an electromagnetic calorimeter (ECL) is needed.
The outermost subdetector is used to identify K_L^0 and muons. The K_L^0 and muon detector (KLM) consists of scintillator strips in the endcaps and glass-electrode resistive

plate chambers in the barrel region.
An overall schematic drawing of the Belle II detector including the used coordinate system can be seen in Figure 3.2.

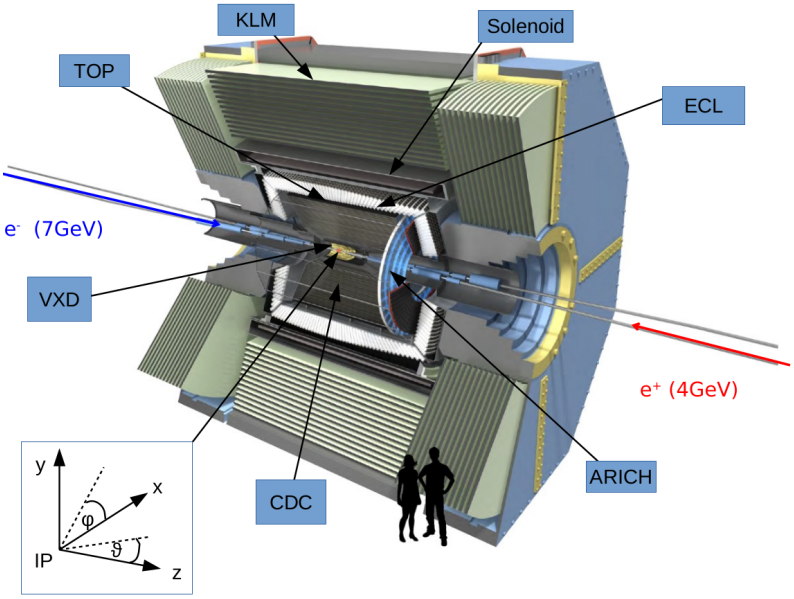

Figure 3.2.: Schematic overview of the Belle II detector with the vertex detector (VXD), the central drift chamber (CDC), the time-of-propagation counter (TOP), the aerogel ring imaging Čerenkov detector (ARICH), the electromagnetic calorimeter (ECL), the solenoid and the K_L^0 and μ detector (KLM). Also drawn is the coordinate system used at Belle II, where the origin corresponds to the IP. Adapted from [104].

3.2.1. Vertex Detector (VXD)

The subdetector closest to the interaction point (IP) is the VXD, which is comprised of the pixel detector (PXD) and the silicon vertex detector (SVD). The reason for mounting a PXD very close to the IP is the existence of an irreducible luminosity dependent background component, that is very large [105]. If silicon strip detectors would be used instead, the occupancy, meaning for each triggered event the fraction of channels hit, would be very high. Therefore, the first two layers (r =14 and 22 mm) of the VXD are pixel detectors. They have 10M readout channels (the SVD has 245k readout channels) and therefore a much smaller occupancy and resolution to measure origin vertices of charged particles precisely. For the four outer layers ($r = 38, 80, 115$ and 140 mm) silicon strip detectors are used, as the occupancy is much less when being further away from the beam pipe as it scales with $1/r^2$.
The basic principle for both vertex detectors is based on the semiconducting material silicon. For silicon the energy gap between the valence and conduction band is very small

and thus it is possible for charged particles to generate electron-hole pairs, when they are traversing the sensor. The number of free electrons is proportional to the deposited energy and can be measured using external electronics. The measured signal can then be converted into binary format and sent to the detector readout and the trigger.
The PXD is based on the DEPleted p-channel Field Effect Transistors (DEPFET) [106]. These DEPFET sensors are very thin with a thickness of the sensitive parts of about 75 µm, which has the advantage of having a small material budget, resulting in a reduction of multiple scattered charged particles. This can be achieved because of the signal amplification, which is done internally, and the high signal-to-noise ratio.
The combination of PXD and SVD is able to measure the vertices of the two decaying B mesons. The SVD alone can also provide information about other decaying particles such as the ones from the D mesons or the τ leptons. The design of the SVD is similar to the *Belle* SVD. This means that the modules have about the same thickness of around 300 µm. But due to the lower boost at Belle II, the forward sensors of the three outermost layers are tilted with an angle towards the beam axis direction.
A figure showing the PXD and the SVD, including the three tilted outermost layers, can be seen in 3.3.

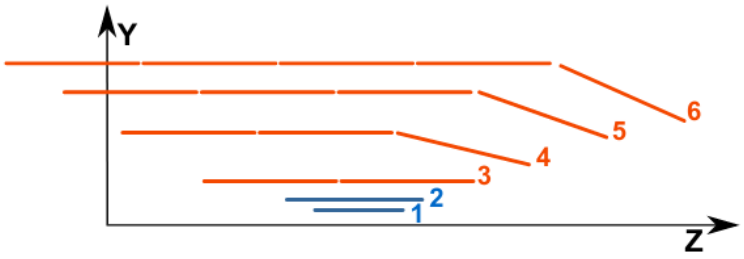

Figure 3.3.: Shown in blue are the two layers of the PXD (1, 2), followed by the four layers of the SVD (3, 4, 5, 6) in orange. Starting from layer 4, the modules of the SVD are tilted [107].

In general, the beam pipe and the first two detector layers of the Belle II detector are much closer to the IP than at *Belle*. Furthermore, the VXD has a much bigger radius than the *Belle* detector had. This results in a much better vertex resolution as well as a better reconstruction efficiency for the decays such as $K_S^0 \to \pi^+\pi^-$ at Belle II.

3.2.2. Central Drift Chamber (CDC)

One of the major subdetectors used for tracking in the Belle II detector is the central drift chamber (CDC). It is a multi-wire proportional chamber, which is filled with a 50:50 helium-ethane gas mixture. In total, it contains 14 336 sense wires arranged in 56 layers. Each of these layers is either aligned with the magnetic field of the solenoid ("axial") or skewed with respect to the axial wires ("stereo"). The combination of information gained

by the axial and stereo wires at the end allows to reconstruct a 3D helix track. Every charged particle that traverses the CDC produces free electrons and ions. Due to the large mass of the ions, they recombine quickly again. Compared to that, the electrons are accelerated as a result of the applied electric field between this field and the sense wires. Secondary ionisation processes happen up to the point, when a measurable signal can be read out by the sense wires. By using ethane also in the gas, it can be ensured that the cascading ionisation just happens locally around the sense wire. Due to the magnetic field, the charged particle tracks are bent. With this knowledge the energy loss per distance $\mathrm{d}E/\mathrm{d}x$ and the momentum for each track can be inferred. Using this $\mathrm{d}E/\mathrm{d}x$ of each track, one can use the Bethe formula [108] to relate the measured track to a particle. This is of particular importance for very low momentum particles, which do not reach the outer subdetectors, thus the particle identification.
In comparison to the gas chamber of the *Belle* detector, the CDC is much larger. It has a radius of 1130 mm compared to the CDC in the *Belle* detector with 880 mm. Furthermore, the drift cells itself are smaller, as there occur more collisions resulting in an increase in background.

3.2.3. Particle Identification (PID)

The particle identification (PID) system for the Belle II detector used to discriminate between charged particles, especially between pions and kaons, can be further split into the aerogel ring imaging Čerenkov detector (ARICH) and the time-of-propagation counter (TOP).
The ARICH is installed in the front-end cap, where it covers the polar angle in the range between 17° and 35°. In the barrel region, the TOP is placed, where the range of the polar angle between 32° and 120° is covered by it.
Both of the detectors used for PID exploit the Čerenkov effect. The effect is based on a cone of Čerenkov photons, being emitted by a particle passing through a dielectric medium with a speed, which is greater than the speed of light in the respective medium. The Čerenkov angle θ_C depends only on the velocity of the traversing particle and the refractive index of the used material. It does not rely on information about the momentum of the corresponding particle. By considering the measurement of the CDC regarding the momentum and the velocity measurement from the PID, the mass of the particle can be determined and thus kaons and pions can be distinguished.
A schematic drawing of the Čerenkov effect can be seen for the TOP in Figure 3.4. The radiator used in the TOP is quartz, compared to the ARICH, which uses aerogel as the Čerenkov radiator.
In the previous experiment, at the *Belle* detector, instead of the ARICH an aerogel Čerenkov counter (ACC) and instead of the TOP a time of flight counter (TOF), were used. One reason for changing the PID in addition to the higher backgrounds at the Belle II detector is the reduced amount of material used for the PID. This in return results in a better response of the electromagnetic calorimeter following in the next outer layer.

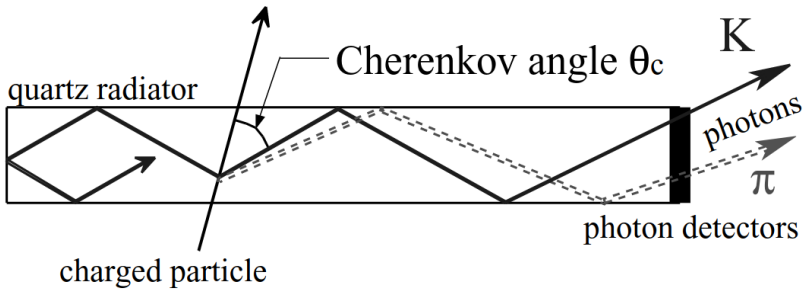

Figure 3.4.: A schematic showing the internal reflection of the Čerenkov photons resulting from a charged particle in this case either a charged kaon or a charged pion. Taken from [96].

3.2.4. Electromagnetic Calorimeter (ECL)

About one third of the decay products of the B meson decays are neutral pions, which mainly decay into a pair of photons. So far, the photons could not be measured by the previous subdetectors. The subdetector concerned about measuring the energy of the photons as well as the electrons and positrons, which could already be measured by the previous subdetectors, is the electromagnetic calorimeter (ECL).
The ECL exploits electromagnetic showers. If an electron, positron or a photon enters into a material, the particle loses its energy through bremsstrahlung or pair production, therefore, resulting in a shower of particles. When the shower particles are below the critical energy, they start to excite the material and are absorbed. The resulting light can then be measuring using photo multipliers. The way this was incorporated into the Belle II ECL is to use a highly-segmented array of thallium-doped caesium iodide CsI(Tl) crystals. In total across the three detector regions of the barrel, forward and backward end-caps 8736 crystals are installed. This results in a coverage of the solid angle in the CMS of about 90 %.
Mainly all the hardware from the *Belle* ECL was reused for the Belle II ECL. The only major difference between the two calorimeters is the improved readout system and the reconstruction software for the Belle II detector. The reason for this upgrade was mainly the increased number of background processes.

3.2.5. K_L^0 and Muon Detector (KLM)

The magnetic flux for the solenoid returns through the iron return yoke, which is used for the outermost system, the K_L^0 and muon detector (KLM). The iron is used as an absorber material, which is alternated with layers of resistive plate counters (RPCs). The glass electrode RPCs, separated by a gas-filled gap, are parallel electrodes with a very high bulk resistivity. If a charged particle passes through the gas, the gas molecules are ionised and the electrodes are discharged. This discharge is local, as the resistance

is very high. With the help of perpendicular readout strips, the location can thus be measured.
The ECL has 0.8 interaction lengths for the K_L^0 mesons, whereas the KLM adds another 3.9 interaction lengths using 14 iron layers for the barrel and each end-cap region. Therefore, the flight direction of the K_L^0 can be determined.
Most of the other charged particles are being shielded by the iron structure and the solenoid, but if one reaches the RPCs, a differentiation between the charged particle and a muon can be done due to their energy loss, as muons barely interact resulting in a much further travelled distance and less scattering in the KLM, or even just traversing it.
With the higher background rates for the Belle II detector arising due to neutrons being produced in electromagnetic showers from background reactions such as radiative Bhabha scattering, not in all the regions RPCs are being used as in *Belle*. Due to the higher background fluxes, the detection efficiency for the RPC will be less, as there is a long dead time for the recovery of the electric field after discharging. Therefore, the RPCs in the end-caps of the former *Belle* detector were replaced by scintillators for the Belle II experiment.

3.2.6. Trigger

The purpose of the trigger system is to discriminate background events from events, which are interesting to investigate, during data taking. However, saving all data would be overwhelming for the bandwidth as well as the data storage. Therefore, a trigger system is required.
For this task, the trigger system for the Belle II detector is nearly completely reused from the *Belle* experiment. The triggering scheme is split into two triggering steps, the hardware (Level 1) and the software (High Level Trigger [HLT]) trigger.
The hardware trigger is further divided into a sub-trigger system and one final-decision logic (FDL). The sub-trigger collects information for a specific subdetector and sends it to the FDL. The FDL has to combine the information from the sub-triggers and decide if the event should be triggered or not. This approach was especially useful for hadronic events, where the trigger system achieved an efficiency of nearly 100 % for *Belle*.
After the Level 1 trigger, a very simplified form of the event reconstruction, optimised on speed, is performed and the HLT decides if the event is stored or not. In addition to this binary decision, the HLT also classifies the events regarding to their underlying physical processes.
Compared to the *Belle* trigger, the Belle II trigger also looks for events with low multiplicity, the dark sector, so single photon events and also axion-like particle searches using two- and three photon events. This broadens the physics scope, but is a big challenge for the data acquisition system.
Moreover, the trigger system for the Belle II detector has been upgraded by including certain information about subdetectors to cope with the increase in the background conditions.

CHAPTER 4

Data Sets

This chapter gives more details on the experimental data recorded at the Belle II detector as well as information regarding the simulated data used in this analysis.

4.1. Experimental data

The experimental data set used for this analysis was taken during the time between the end of the commissioning phase to prepare the accelerator and the detector for the recording of data in 2019 and the first long shut down in 2022, where the detector underwent an upgrade.
The total collected data set corresponds to about $(423.593 \pm 0.022)\,\mathrm{fb}^{-1}$ [109] of integrated luminosity, however not all the data were recorded at the $\Upsilon(4S)$ resonance. In total, the analysed data set at the $\Upsilon(4S)$ resonance corresponds to an integrated luminosity of $(364.436 \pm 0.020)\,\mathrm{fb}^{-1}$ [109]. The just mentioned integrated luminosity only uses data sets that meet the quality constraints for physics measurements. These are considered as "good" runs, and are therefore suitable for physics analyses. This data set is competitive with the data set collected by the *BABAR* collaboration and corresponds to about half the data set collected by the *Belle* detector.
In addition to the data set collected at the $\Upsilon(4S)$ resonance, some data was recorded below this resonance. This off-resonance data set corresponds to about $(42.329 \pm 0.007)\,\mathrm{fb}^{-1}$ [109] and helps in understanding the continuum background as detailed in section 4.2.2.

4.2. Simulated data

Monte Carlo simulations (MC) are an important tool to determine the optimal event selections for an analysis or produce signal and background model templates to extract

certain quantities, such as a branching ratio, from the recorded data.
Since interactions of particles can be described using quantum mechanics, MC simulations are based on probabilities. With the help of MC generators, it is possible to produce simulated events that have very similar properties to experimental data. This means, to be more precise, that the final state particles of the e^-e^+ interaction can be simulated. At first, the initial particles are passed through the MC generator, which generates hard interactions and decays. Next, the generators handle the decay in flight and the stable particles are passed through the detector simulation. Additionally, the energy depositions in the different sub-detectors are simulated. These energy depositions produce measurable signals that mimic these energy depositions for the recorded data. The simulation is made more realistic by considering beam backgrounds, which arise due to e.g. the loss of beam particles during the machine operation, which lead to electromagnetic showers and thus higher hit rates.
The simulation of the initial particles, i.e. the e^-e^+ collision, the hadronisation and the decays in flight is done using EvtGen [110]. The interactions with the detector material are simulated using Geant4 [111], and its response using the open-source software framework Belle II analysis software framework (basf2) [112, 113].
To account for final state radiation of photons originating from charged stable particles PHOTOS [114, 115] is used.
At last, the beam background is incorporated into the simulation [116].

4.2.1. $B \to X_c \ell \nu_\ell$ decays

According to most recent measurements, the sum of all exclusively measured $B \to X_c \ell \nu_\ell$ decays only adds up to roughly 90 % of the inclusively measured branching ratio for the $B \to X_c \ell \nu_\ell$ decays [70]. The remaining 10 % of the $B \to X_c \ell \nu_\ell$ decays, called the "gap", are filled in the MC generation with the so far unmeasured decays of the nature $B \to D^{(*)} \eta \ell \nu_\ell$ and decays of the nature $B \to D^{(*)} \pi\pi \ell \nu_\ell$. The $B \to D^{(*)} \pi\pi \ell \nu_\ell$ decays however proceed via the broad D_0^* and D_1' states, which is much more plausible than the generation using phase space, which is an alternative approach to model these modes. The approach via the resonance has already been assessed in previous *Belle* measurements [117].
A new model-independent calculation of the form factors (explained in more depth further below) for the decays $B \to D\pi \ell \nu_\ell$ just recently showed that the semi-leptonic gap cannot be filled only by the assumed gap modes mentioned above [118]. Consequently, the ideas that were so far considered at *Belle* and Belle II as theoretical explanations for the "gap" are excluded as an approach to describe the missing decays.
Unfortunately, there are no new proposals to fill the remaining gap in the simulation, and therefore, the old approach is still used for this analysis. However, the simulation of the gap already includes the newest branching ratios.
The calculation of the branching fractions for the different processes can be found in [117]. Here, branching fraction ratios, absolute measurements and the knowledge of isospin relations between certain hadrons are exploited to determine the individual values. The generated branching ratios are updated to newer values to account for e.g. improved

measurements or theoretical calculations.
The resulting branching ratios and their uncertainties are summarised in table 4.1.

Process	$\mathcal{B}(B^+) \times 10^{-3}$	$\mathcal{B}(B^0) \times 10^{-3}$
$B \to D\ell\nu_\ell$	24.10 ± 0.71	22.40 ± 0.66
$B \to D^*\ell\nu_\ell$	55.02 ± 1.15	51.14 ± 1.08
$B \to D_0^*\ell\nu_\ell$	4.20 ± 0.75	3.90 ± 0.70
$B \to D_1'\ell\nu_\ell$	4.20 ± 0.90	3.90 ± 0.84
$B \to D_1\ell\nu_\ell$	6.63 ± 1.09	6.61 ± 1.01
$B \to D_2^*\ell\nu_\ell$	2.93 ± 0.32	2.73 ± 0.30
$B \to D\pi\pi\ell\nu_\ell$	0.62 ± 0.89	0.58 ± 0.82
$B \to D^*\pi\pi\ell\nu_\ell$	2.16 ± 1.02	2.01 ± 0.95
$B \to D_s K\ell\nu_\ell$	0.30 ± 0.14	-
$B \to D_s^* K\ell\nu_\ell$	0.29 ± 0.19	-
$B \to D\eta\ell\nu_\ell$	3.77 ± 3.77	4.09 ± 4.09
$B \to D^*\eta\ell\nu_\ell$	3.77 ± 3.77	4.09 ± 4.09
$B \to X_c\ell\nu_\ell$	108.00 ± 4.00	101.00 ± 4.00

Table 4.1.: Branching ratios for the exclusive $B \to X_c\ell\nu_\ell$ processes from [117], so that the sum of the individual processes sums up to the measured inclusive $B \to X_c\ell\nu_\ell$ branching ratio in the last row. The last two processes including η mesons are so far unmeasured and thus an uncertainty of 100 % is assigned to them.

The procedure to include the updated branching fractions into the simulation is by reweighting the events based on their truth information using the weight w_{BR}, where the weight can be determined as following:

$$w_{BR,i} = \frac{BR_i^{\text{updated}}}{BR_i^{\text{MC}}}, \tag{4.1}$$

with i being the considered generated decay, BR^{updated} being the updated and BR^{MC} the used branching ratio in the current simulation.

$D^{(*(*))}$ meson decays

Another very important contribution to a correct simulation are the form factors. These encode the hadronic transition properties of the hadrons and need to be calculated numerically. They have a significant impact on the shapes of kinematic distributions. In some cases, the simulation does not include the newest parameters or models, therefore, it is updated by reweighting the generated events.
In table 4.2, the form factor models used in the current simulation can be seen as well as the form factor models that are now considered for this analysis. The general idea to calculate the form factors for the $b \to c$ transitions is considering the HQET as

mentioned in section 2.3. The high masses of the b and c are exploited, but due to the finiteness of the masses, the form factor calculations need to be corrected by additional terms such as $1/m_Q$ and $\alpha_s(m_Q)$.

Process	Form factor model	No. parameters	Reference
$B \to D\ell\nu_\ell$	BGL to BLPRXP	9	[119]
$B \to D^*\ell\nu_\ell$	BGL to BLPRXP	9	[119]
$B \to (D_0^*, D_1')\ell\nu_\ell$	BLR to BLR	3	[120, 121]
$B \to (D_1, D_2^*)\ell\nu_\ell$	BLR to BLR	4	[120, 121]

Table 4.2.: The different form factor models used in the current simulation and the form factor models considered for this analysis including references and the number of parameters. For the $B \to D^{**}\ell\nu_\ell$ decays the form factor models stay the same only the input parameters are updated.

The updating of parameters as well as changing between different form factor models is done using Hammer [122]. Hammer is a software package for matrix element reweighting. It translates events generated with another form factor model to a new model including the uncertainties of the new form factors. This is done by alternating the events via weights in the following manner:

$$w_i = \frac{\Gamma_{\text{MC}}}{\Gamma_{\text{new}}} \cdot \frac{\mathrm{d}\Gamma_{\text{new}}}{\mathrm{d}\Gamma_{\text{MC}}}, \tag{4.2}$$

where Γ is the total and $\mathrm{d}\Gamma$ the differential decay rate.
By using Hammer it is possible to not only change the central prediction, but also evaluate the uncertainties originating from the form factor models. To do so, the chosen form factor parameters are rotated into an uncorrelated eigenbasis. These rotated parameters are varied within their $\pm 1\,\sigma$ uncertainties to produce additional weights, such that at the end there is one resulting variation for every form factor parameter.
Since the kinematics of the broad D^{**}mesons are poorly known, the rotated parameters are instead varied within $\pm 1.5\,\sigma$ of their large uncertainties.

4.2.2. Light quark pair interaction

Another important process is the light quark pair production from e^-e^+ interactions, which is also called continuum or $q\bar{q}$ background.
Since the resulting hadrons are not produced in resonance, it is not possible to use EvtGen directly. Rather, a combination of two MC generators is used. At first, the KKMC generator [123] produces quark pairs while considering Initial State Radiation (ISR), Final State Radiation (FSR) and also the interference between both. Secondly, the general-purpose MC generator PYTHIA [124] produces a parton shower from the quark pair, which is then hadronised.

The resulting unstable hadrons and their decays in this hadronisation process are then again simulated via EvtGen.
Using this approach the key features of the off-resonance data sets are reproduced, but they are highly dependent on many different experimentally determined input parameters for PYTHIA. Currently, the determination for the parameters in PYTHIA is still a work-in-progress in the Belle II collaboration and thus this part of the simulation is assumed to be less reliable than the simulated $B\overline{B}$ samples.
In addition, events of the nature $e^- e^+ \to \tau^- \tau^+$ are generated using the dedicated MC generator TAUOLA [125].

CHAPTER 5

Tools

This chapter describes the used tools and methods for this analysis in detail. At first in section 5.1 a general introduction about boosted decision trees is given. Following this, the different reconstruction possibilities for the second B meson are mentioned in section 5.2. In subsection 5.2.1 the Full Event Interpretation utilised at Belle II is described. Afterwards, the Belle II analysis framework is explained in section 5.3. At last, the used particle identification methods at Belle II are discussed in section 5.4.

5.1. Boosted Decision Trees

Multivariate algorithms (MVA) have become very popular during the last decades. They are easy to use and take into account the correlation between variables, compared to the traditional sequence of cuts for the categorisation of reconstructed events into signal (the process of interest) and background events (incorrectly reconstructed events).
It is out of the scope of this thesis to give a full overview about boosted decision trees, so the reader is referred to e.g. [126] for further information.
In general, there are two steps for an MVA. The first step is called fitting- or training-phase, where the statistical model is sequentially learned from the given data set by considering more and more features. There exist different approaches e.g. supervised learning, meaning that the data set used for training is labelled as being a signal or background event. During the second phase, the inference-phase, the model is used to infer the desired information from a new independent data set.
For the best possible classification result however, the training needs to stop before only learning statistical fluctuations, as this result does not generalise well on the new unseen data set. This phenomenon is called overtraining and there are several ways to prevent it, like simplifying the structure of the used MVA.

There are different types of MVAs like Boosted Decision Trees (BDT) or Neural Networks (NN). The focus of this chapter lies on BDTs.
A single decision tree can be thought of as a series of one-dimensional splits of the data set, where each split is optimised using a certain figure-of-merit (FOM). The labelled data set is split at the point, where the separation becomes maximal on the statistically independent data set.
A single decision tree however needs a large depth for a reasonable separation power, meaning many branches where the separation improvement of the final splits is only very small. This easily results in overtraining. To address this problem, the depth parameter can be adapted or instead of training a comparably deep decision tree, one could combine multiple shallow trees to a "forest".
There are different approaches for combing shallow trees called bagging [127] and boosting [128]. The bagging method is based on resampling with replacement, whereas the boosting approach iteratively optimises assigned weights to the training data set in each iteration step, so that misclassified data gains higher importance. During each iteration step one tree is trained and the weights are updated accordingly for the training of the next tree.
One boosting possibility is the Stochastic Gradient Boosted Decision Tree (SGBDT) that combines gradient boosting [129] with stochastic gradient boosting [130].
For the stochastic boosting each tree is trained using the residual errors of the predecessor as labels. While for the stochastic gradient boosting, at each iteration a subsample of the training data is drawn at random (without replacement) and the randomly selected subsample is used to train the learner.
At Belle II there are a few use-cases for SGBDTs, for example the reconstruction of the tag-side B meson or also for the particle identification. To be more precise, FastBDTs (FBDTs) [131] are used.
FBDTs are SGBDTs in a fast and cache-optimised way. Compared to normal SGBDTs, FBDTs are more robust to missing data, also allow preprocessing and an estimation of the feature importance.
Missing data in this sense means that e.g. certain detector information are not available due to technical reasons or the particle did not active a certain subdetector.

5.2. Reconstruction of B mesons

As already mentioned, B mesons are always produced in pairs at Belle II, but due to their short life time they cannot be measured directly. The detector measures final state particles or particles with a long life time.
In this analysis, only one of the B mesons (B_{Sig}) is reconstructed in the decay of interest. The decay products of the other B meson, called B_{Tag}, overlap with the B_{Sig} decay products in the detector. Therefore, there exist different approaches how to reconstruct or treat the B_{Tag} meson with a trade-off between precision and efficiency.
The three possibilities to reconstruct the B_{Tag} meson are called untagged or inclusive, semileptonic, or hadronic tagging. For the untagged case, the B_{Sig} mesons is recon-

structed in the decay of interest and the B_{Tag} meson is not reconstructed at all. This results in a large sample size with much statistics, however there are many possible combinations during the reconstruction as all measured particles in the detector are considered. Thus, this reconstruction approach yields many signal events, but also a lot of background events from wrongly reconstructed events resulting in a high signal efficiency, but a low purity.
The other two methods reconstruct the B_{Tag} meson in exclusive channels. In case of the semileptonic tagging, semileptonic decay modes are considered for the reconstruction of the B meson. The semileptonic approach has one neutrino in the final state, which results in missing kinematic information.
In contrast to this, the hadronic tagging method only uses hadronic decay modes to reconstruct the B_{Tag} meson. The individual hadronic branching ratios however are much lower than the semileptonic branching ratios. Besides, the tagging efficiency for the hadronic tagging is in the order of $\mathcal{O}(10^{-3})$.
The upside of using hadronic tagging is nevertheless that the total four-momentum of the B_{Tag} meson is well known and a very pure selected sample. Therefore, the hadronic tagging approach is used in this analysis.
A schematic summarising the three different approaches to reconstruct the B_{Tag} meson including their efficiencies and their information content can be seen in fig. 5.1.

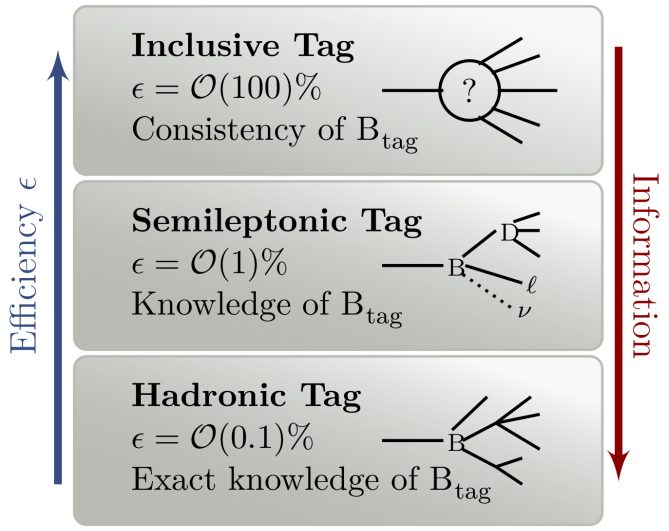

Figure 5.1.: Schematic sketch of the three different tag approaches for the B_{Tag} meson including reconstruction efficiencies and their information content. Taken from [132].

5.2.1. Full Event Interpretation

Already at *Belle* there existed two different approaches to reconstruct the B_{Tag} meson hadronically. The first algorithm (see e.g. [133–137]) is based on a fixed selection that reconstructs specific $B \to D^{(*)}X$ decay modes. The second approach is called Full Reconstruction (FR) [138] and increases the number of hadronically reconstructed decay channels by exploiting multivariate analysis methods for the determination of a probability metric for the reconstructed decay at each reconstruction stage.
In previous measurements of the branching ratio $B \to D^{**}\ell\nu_\ell$ at *Belle*, the FR, which was especially developed for *Belle* was used in [93]. The latest *Belle* measurement [94] used the Full Event Interpretation(FEI) [132], which is the successor of the FR designed for the Belle II experiment.
Approximately 200 SGBDTs from the FBDT package are used to combine final state particles to B mesons using the FEI algorithm. The classifier uses a hierarchical approach with six stages. At the beginning lighter particles are combined to reconstruct heavier hadrons.
The detailed six reconstruction and classification stages of the FEI are:

1. long-lived neutral (γ and K_L^0) and charged (e^-, μ^-, π^+, K^+ and p) particles formed from tracks, calorimeter and KLM clusters,
2. reconstruction of J/ψ, π^0 and Λ,
3. reconstruction of K_S^0 and Σ^+,
4. reconstruction of D and Λ_c^+,
5. reconstruction of D^*,
6. reconstruction of B^+ and B^0.

A schematic of the FEI can be seen in fig. 5.2.
For each reconstruction stage of the FEI, all previous particle candidates are combined to heavier particles. After the recombination, the vertexing algorithm utilised at *Belle* [139] is used to determine the probability that the combined particles originate from the same vertex.
Following that, the SGBDT is applied and depending on the particle type the best 5-20 candidates with the highest classifier output are considered for the next reconstruction step. Each classifier uses specific decay features, however, the production vertex is a strong constraint. This so called best candidate selection is different than the one used at *Belle* for the FR. In the FR, for each decay channel there were different threshold cuts imposed on the classifier output. By considering only a certain number of candidates per event the computing resources are more evenly distributed between events and decay channels than for the FR. Thus, there is no single event that generates a large amount of possible candidates that requires a lot of resources and a rather long next fitting phase.
At the end, the FEI has one last classifier that is used to assign a signal probability to

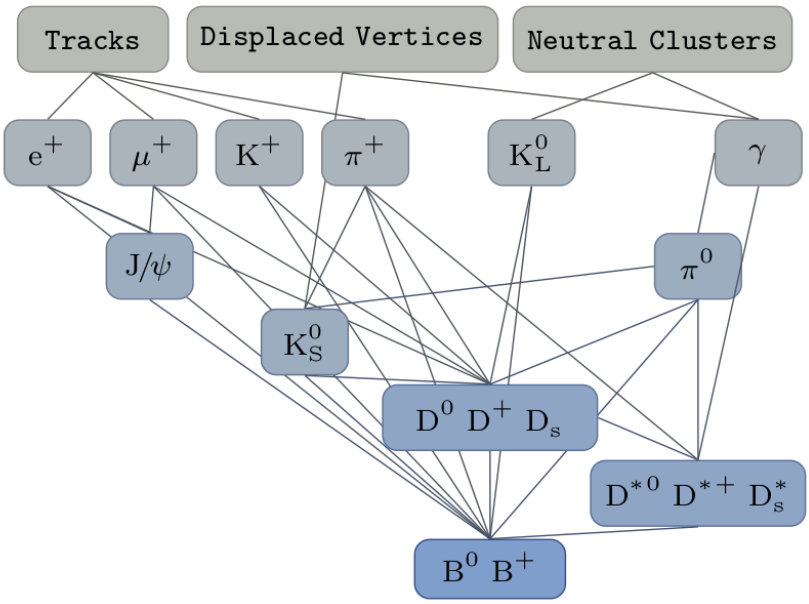

Figure 5.2.: Schematic sketch of the FEI, where the hierarchical approach of the algorithm is visible. Starting with detector information to build final state particles and combining these to intermediate particles to at last form a B meson candidate. Taken from [132].

the B meson and outputs up to 20 possible B meson candidates.
For the reconstruction of the intermediate particles and the B mesons the FEI reconstructs more than 100 explicit decay channels for the intermediate particles, where the explicit decay channels are summarised in [132]. For the charged B meson there exist 36 decay channels, whereas the neutral B meson is reconstructed in 32 decay channels.
There are different approaches on how to proceed now with the analysis after the B_{Tag} meson has been reconstructed. One possibility would be to use the candidate with the highest signal probability or as an alternative investigate the signal side first, which might however impact the ranking of the candidates.
Furthermore, the usage of the hadronic FEI for the reconstruction of the B_{Tag} meson reduces the combinatoric background significantly. It happens due to the fact that the considered reconstructed particles are assigned to the tag side and cannot be considered for the signal side reconstruction any longer.
In general, the FEI has a higher purity and larger tag-side efficiency than the FR by using an improved classification method, additional channels and the best candidate selection. This can also be seen in fig. 5.3a for the charged B meson and in fig. 5.3b for the B^0, where the FEI outperforms the FR in most cases, especially for regions with high efficiencies, where most analyses can be found.

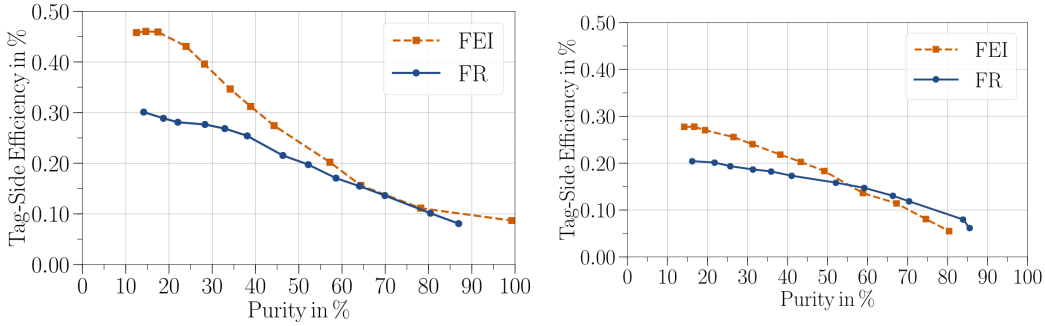

(a) B^+ meson

(b) B^0 meson

Figure 5.3.: The tag-side efficiency in dependence of the purity for the charged and neutral B mesons compared for the FR and the FEI. Taken from [132].

5.3. BASF2

The Belle II analysis software framework (BASF2) [112, 113] is used for the online processing of the data as well as the post-processing of the simulated and experimental data for this analysis. It is based on the data analysis framework ROOT [140, 141] with most of the code written in C++. For higher flexibility, the BASF2 framework is however split into individual modules with certain purposes. The programming language Python is used for the configuration as well as the arrangement of the different modules.
In general, data and MC are saved in files with event-wise basic quantities. These quantities, such as tracks, clusters or the combination of both, can be used to build particle candidates. These particle candidates can then be further combined to intermediate particles and at the end into an $\Upsilon(4S)$ candidate. Usually, there is more than one $\Upsilon(4S)$ candidate at the end of the reconstruction due to combinatorics, therefore, a best candidate selection needs to be performed to have only one reconstructed candidate at the end.

5.4. Particle identification

To distinguish between different particle candidates, particle identification (PID) is a useful tool. It uses information from all subdetectors except for the PXD. The PID gets the particle velocity from the TOP and the ARICH, the energy loss per distance from the tracking system and the deposited energy from the ECL as well as information to distinguish between π and μ depending on the traversing depth in the KLM.
There are two approaches at Belle II to combine all these detector outputs into one single variable. The first approach, which is explained in more detail in [103], assumes that the measured observables are independent between the different subdetectors and that the different particle hypotheses can be described by independent likelihood functions. To parametrise the likelihood functions $\mathcal{L}^d(\boldsymbol{x}|i)$ for each particle hypothesis i, joint

probability density functions (PDFs), based on a set of observables $\boldsymbol{x}$ in each detector part d, are utilised. In this analysis the simulation is used to determine the various likelihood functions for the different detector parts. There are also other approaches to determine the likelihood such as using well-measured physical processes or analytic descriptions.
The resulting global likelihood $\mathcal{L}(\boldsymbol{x}|i)$ is given as a product of the individual likelihoods $\mathcal{L}^d(\boldsymbol{x}|i)$ for each particle hypotheses.
By using Bayes' theorem, the probability of identifying a particle candidate in hypotheses i against all other possible hypotheses j is given by:

$$P(i|\boldsymbol{x}) = \frac{\mathcal{L}^d(\boldsymbol{x}|i)}{\sum_j \mathcal{L}^d(\boldsymbol{x}|j)}, \tag{5.1}$$

which is according to the Neyman-Pearson lemma the optimal discriminator.
Other possible particle hypotheses j that can be tested against are the two light charged leptons, meaning electron and muon, the charged pions and kaons, the proton and the deuteron.
The PID utilising likelihoods is considered in this analysis for the charged pions and kaons as well as the muons.
The second approach [142] is based on MVAs. In contrast to the likelihood method it is also helpful for low-momentum particles as the likelihoods for the ECL are determined via E/p.
For the used BDT in this approach one can use many low-level features of the calorimeter shower, such as the longitudinal development of the shower, that are highly correlated and include other subdetectors directly via likelihoods instead of using their product.
The MVA approach is considered for the electrons in this analysis.

CHAPTER 6

Reconstruction

This chapter will outline the reconstruction of different particles from the final state particles measured as detector signals as well as the used selection cuts, to get a fairly clean distribution to extract the branching ratio for the reconstructed $B \to D^{**}\ell\nu_\ell$ decays. Following this, the reconstructed final state particles are combined for the reconstruction of the D, D^* and the D^{**} mesons, which are then used to build B meson candidates and at the end the $\Upsilon(4S)$ resonance candidate.
The particle definitions and selection cuts used in this analysis are based on already performed analyses at Belle II such as [143–145]. Furthermore, for correction factors to be applicable, the selections between the samples for the determination of the corrections and the sample the corrections are applied to need to be perfectly aligned. Only for the selections of the D^{**} mesons in this analysis, there are no suggestions available.
After the reconstruction of the $\Upsilon(4S)$ resonance, a best candidate selection is performed so that maximally one candidate is left per event after all selection cuts are considered. Moreover, the background categorisation of the reconstructed simulated samples will be explained.
In addition to this, a study investigating the contribution of each D meson decay in dependence of each reconstructed B meson decay mode for the significance of this particular decay channel is performed.
At last, there exist some corrections that either have to be applied to experimental or the simulated data to account for e.g. efficiency differences.

6.1. Pre-selections of the hadronic FEI

The whole analysis is based on the hadronic FEI skims, which are filtered samples that already include a few pre-selection cuts on tracks, ECL clusters and their multiplicity:

$$\text{good track}: \quad dr < 2\,\text{cm}, \quad |dz| < 4\,\text{cm}, \quad p_\text{T} > 0.1\,\text{GeV}\,c^{-1} \tag{6.1}$$

$$\text{good cluster}: \quad 0.296706 < \theta < 2.617\,99\,\text{rad}, \quad E > 0.1\,\text{GeV}. \tag{6.2}$$

The cuts on dr and dz ensure that the particle candidates originate from the IP. Here, dr is the transverse distance with respect to the IP and dz the distance into the z direction. p_T is the transverse momentum of the particle and θ its polar angle.
To be more precise, these track impact parameters at the point of closest approach (POCA), meaning dr and dz, are measured with respect to the IP, as defined in [146].
At the end, at least three good tracks and clusters in the pre-selection of the FEI are required. Besides, there is a lower cut on the sum of all cluster energies of the event in the CMS frame at 4 GeV.

6.2. Neutral particles

This section will focus on the reconstruction of the neutral particles used to reconstruct D^{**} mesons. At first, the two definitions of the photons γ used to reconstruct neutral π mesons are described, where a distinction has to be made between neutral pions with a low momentum, meaning a momentum below $0.2\,\text{GeV}\,c^{-1}$, for the D^* meson reconstruction as well as for daughters of the D^{**} meson and the nominal neutral pion. This nominal pion has a momentum above $0.2\,\text{GeV}\,c^{-1}$ and is used to reconstruct e.g. D mesons.
At last, an explanation of the reconstruction of the K_S^0 is given.

6.2.1. Photon identification

The photons are not directly used in this analysis, they are only used to reconstruct neutral pions by using clusters measured in the electromagnetic calorimeter.
As already mentioned, there are two different γ definitions [147,148] used to reconstruct the π^0 mesons.
To suppress background originating from minimal ionising particles passing the ECL, all reconstructed photons need to have a weighted sum of the number of calorimeter crystal hits above 1.5, where energy splitting across overlapping crystals is taken into consideration via these weights.
In general, the photon candidates are required to pass different energy selection cuts on the clusters of the electromagnetic calorimeter depending on the ECL region. In the forward endcap of the calorimeter, the energy threshold is 80 MeV, whereas the threshold in the barrel region is 30 MeV and 60 MeV for the backward endcap.
To veto clusters originating from electrons in the ECL, additional CDC tracking information is taken into account that removes photon candidates with associated measured

tracks in the CDC. However, this information is only valid for tracks that pass the CDC. Thus, only photon candidates that are reconstructed in the angular region of the ECL that corresponds to the angular acceptance of the CDC, are considered.
Besides the already mentioned selection cuts, some additional selections on the photons used in the slow neutral pion reconstruction need to be considered. At first, a loose selection cut on the time of the ECL cluster of 200 ns is performed. Here, the cluster timing is the time between the measurement of the photon in the ECL and the time, when the event was triggered.
Furthermore, to distinguish between true photon clusters and fake photon clusters from e.g. split-offs or track-cluster matching failures, a selection cut on a pre-trained MVA classifier [149], trained using shower-related variables, is performed.

6.2.2. Neutral pion

For the nominal neutral pions [148], two photon candidates, as just described in the previous section, section 6.2.1, are combined to form a π^0 candidate. The invariant mass of the nominal reconstructed π^0 candidate needs to be in the range of 120 to 145 MeV c^{-2}.
Nominal neutral pions are required to have a momentum in the lab frame greater than 200 MeV c^{-1}. Pions with a momentum between 50 and 200 MeV c^{-1} are called slow neutral pions [147].
In addition to this, the reconstructed mass of the slow neutral pion is only allowed to deviate by 15 MeV c^{-2} from the measured value of the Particle Data Group (PDG) [70].
For both neutral pion candidates, a mass fit is performed using KFit [150], which varies the momenta of the daughter particles within their uncertainties to get a mass value as close as possible to the nominal mass of the π^0. For further reconstruction steps only particle candidates are kept, where the fit converges.

6.2.3. K_S^0

For the reconstruction of the K_S^0 two charged reconstructed tracks are combined, since it decays into two charged pions in about 2/3 [70] of the cases.
A vertex fit using `TreeFit` [151] is performed and only candidates are kept, where the fit converges. `TreeFit` is based on a Kalman Filter [152] for solving a least square estimate for a globally fit decay chain. By using the vertex fit the resolution of measured parameters such as particle momenta or energies is improved. Besides, it helps in suppressing combinatorial background.
In addition to this, a selection cut on the invariant mass of the K_S^0 candidate after the vertex fit in the range of 450 to 550 MeV c^{-2} is applied.
To select mostly true K_S^0 meson candidates, additional selections on the flight distance and its significance are conducted.

6.3. Charged final state particles

In addition to the neutral (final state) particles, there exist two different types of charged final state particles that are important for the reconstruction of intermediate particles such as the D or B mesons. A distinction between two charged hadron types has to be made. These hadrons can either be kaons or pions and charged light leptons, meaning electrons or muons.

6.3.1. Hadrons

For the reconstruction of the charged kaon and pion, considered as daughters of the D and D^{**} meson, similar selection cuts on the particles originating from the interaction point as defined in section 6.1, are performed.
For both charged hadron candidates, the transverse distance to the IP needs to be in the radius of 2 cm and the distance in the z direction below 5 cm. In addition to this, the number of hits in the CDC for the considered track candidate must be more than 20.
To distinguish kaons and pions from each other and also from the light charged leptons, a selection cut on the output value of the likelihood-based particle identification as detailed in section 5.4 is performed.
One possibility to reconstruct a charged D^* meson is combining a neutral D meson with a charged pion. Due to the fact that the mass difference between the reconstructed D^* meson and the D^0 meson is small, a special treatment of the charged pion has to be performed. For this particular case of a slow charged pion, no selection on the track candidates is done. All possible track candidates are considered.

6.3.2. Leptons

For the charged light leptons the same base selections on the IP are performed as for the charged hadrons. On top of that, charged light lepton candidates need to be within the CDC acceptance region.
Besides, for the reconstruction of the muon, only candidates that fulfil a selection cut on the likelihood-based particle identification, which also ensures that there are measured signals in the KLM, are considered.
For the electron candidates the particle identification is performed based on a BDT method as this is more helpful for low-momentum particles. Details on the particle identification can be found in section 5.4.
In addition to this selection on the PID, only muon candidates are considered, where the momentum of the particle candidate in the centre-of-mass frame is above $0.7\,\mathrm{GeV}\,c^{-1}$. This selection is slightly looser for the electron candidates with a value of $0.5\,\mathrm{GeV}\,c^{-1}$.
Moreover, bremsstrahlung is an important phenomenon that needs to be considered for the electron candidates, because the electrons lose energy when interacting with the different detector components.
To take into account this energy loss and the resulting lower electron momenta, the

electron candidates need to be corrected by calorimeter cluster energies that are assigned to the corresponding electron track.
The calorimeter clusters that are considered as bremsstrahlung photons take into account geometrical considerations. In case the photons are in a certain maximum angle β around the considered electron track and pass a maximum energy selection $E_{\mathrm{max},\gamma}$, the electron candidates are corrected using this bremsstrahlung photon.

Electron momentum	Maximal angle β	Maximal energy $E_{\mathrm{max},\gamma}$
$p \leq 0.6\,\mathrm{GeV}\,c^{-1}$	0.1368 rad	0.09 GeV
$p \in (0.6\,\mathrm{GeV}\,c^{-1}, 1.0\,\mathrm{GeV}\,c^{-1}]$	0.0737 rad	0.9 GeV
$p > 1.0\,\mathrm{GeV}\,c^{-1}$	0.0632 rad	1.2 GeV

Table 6.1.: Table showing the different momentum regions for the electron including the optimal parameters for the maximal angle and the energy of the calorimeter clusters assigned to bremsstrahlung photons.

As can be seen in table 6.1, there are three different momentum regions with different selection criteria for the maximal angle and the maximal energy. These values have been determined by minimising the difference between the reconstructed and simulated electron momenta by the semi-leptonic working group in Belle II.
The calorimeter clusters already used for the bremsstrahlung corrections of the electrons are not considered further in the reconstruction of the neutral pion daughters for the $B \to D^{**}\ell\nu_\ell$ decays.

6.4. Reconstruction of intermediate particles

By combining the final state particles, the signal decay $B \to D^{**}\ell\nu_\ell$ and the normalisation decay $B \to D^{*}\ell\nu_\ell$ are reconstructed. A visualisation showing one example decay tree for the reconstruction of the signal decay mode starting with the final state particles on the right-hand side via the intermediate particles towards an $\Upsilon\,(4S)$ resonance, can be seen in fig. 6.1.
In general, it can be said that there exist various different decay modes to reconstruct an intermediate particle candidate. However, it is usually not feasible to reconstruct all of these decay modes. As for the B meson, described in section 2.2, there are three possibilities for the considered mesons to decay. Either the hadronic, the semi-leptonic and the purely leptonic decay modes (only possible for the charged B meson). For the reconstruction of the D mesons these three decay modes are also possible. These decays are mediated by the weak force, as the D meson is the lightest meson containing a charm-quark. However, only the hadronic decay modes are considered for the D, see section 6.4.1 for the considered decay modes in this analysis. The reason for using only the hadronic decay channels is the considerably high branching ratio in addition to the complete reconstruction of the considered meson, meaning that there are no undetected particles such as neutrinos in the reconstruction.

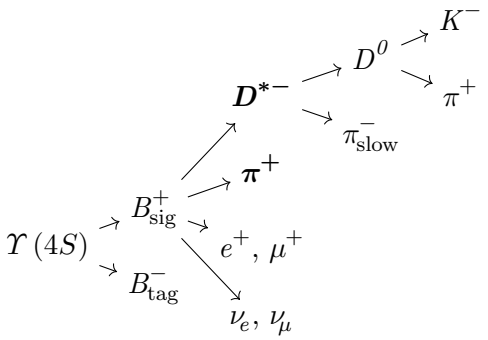

Figure 6.1.: Visualisation of an $\Upsilon(4S)$ decay tree for the signal mode, showing one example decay possibility, where the D^{**} meson is shown in **bold** as a $D^*\pi$ combination. Charge-conjugated decays are also included.

The D^* and the D^{**} mesons are excitations of the D meson and therefore decay either via the electromagnetic or the strong force, which means that the daughters of the decaying mesons can all be measured in the detector in some way and there are no missing particles. The considered decay channels used in this particular analysis can be found in section 6.4.2 for the D^* mesons and in section 6.4.3 for the D^{**} mesons or rather for the B_{Sig}, as the D^{**} meson is not explicitly reconstructed, which will be explained further below.
Therefore, the only missing particle on the signal-side in this analysis is the neutrino in the semi-leptonic decay of the B meson.
Nonetheless, it is not possible to reconstruct all hadronic decay channels, especially for the D mesons as some modes include a lot of neutral particles, which are in general hard to reconstruct. This can result in a lot of wrongly reconstructed meson candidates. Besides, some modes have a very low branching ratio compared to the other hadronic channels.
In addition to the semi-leptonically reconstructed signal side, in section 6.4.4, the selection cuts for the hadronic FEI will be explained in further detail as well as the combination of the tag- and signal- side towards an $\Upsilon(4S)$ candidate in section 6.4.5.

6.4.1. Neutral and charged *D* meson reconstruction

For the reconstruction of a D^{**} meson, a D meson is always required either via a direct decay $D^{**} \to D\pi$ or via a D^* meson, therefore several different decay modes for the charged and neutral D meson decay channels are considered as can be seen in table 6.2 including their branching ratios from [70]. For all decay channels mentioned in this thesis, the charge-conjugated mode, meaning the interchange of all particles with their respective anti-particles, is also reconstructed.
The kinds of particles used for the reconstruction vary, with charged particles such as pions and kaons, which are easier to reconstruct than neutral particles such as π^0 mesons.

Decay channel	Branching ratio
Neutral	
$D^0 \to K^-\pi^+$	$(3.947 \pm 0.030)\,\%$
$D^0 \to K^-\pi^+\pi^0$	$(14.4 \pm 0.5)\,\%$
$D^0 \to K^-\pi^+\pi^+\pi^-$	$(8.22 \pm 0.14)\,\%$
$D^0 \to K^-\pi^+\pi^+\pi^-\pi^0$	$(4.3 \pm 0.4)\,\%$
$D^0 \to K^0_S\pi^0$	$(1.240 \pm 0.022)\,\%$
$D^0 \to K^0_S\pi^+\pi^-$	$(2.80 \pm 0.18)\,\%$
$D^0 \to K^0_S\pi^+\pi^-\pi^0$	$(5.2 \pm 0.6)\,\%$
$D^0 \to K^+K^-$	$(4.08 \pm 0.06) \times 10^{-3}$
$D^0 \to \pi^+\pi^-$	$(1.454 \pm 0.024) \times 10^{-3}$
$D^0 \to K^0_S K^0_S$	$(1.41 \pm 0.05) \times 10^{-4}$
$D^0 \to \pi^0\pi^0$	$(8.26 \pm 0.25) \times 10^{-4}$
$D^0 \to K^0_S\pi^0\pi^0$	$(9.1 \pm 1.1) \times 10^{-3}$
$D^0 \to \pi^+\pi^-\pi^0$	$(1.49 \pm 0.06)\,\%$
Charged	
$D^+ \to K^-\pi^+\pi^+$	$(9.38 \pm 0.16)\,\%$
$D^+ \to K^-\pi^+\pi^+\pi^0$	$(6.25 \pm 0.18)\,\%$
$D^+ \to K^-\pi^+\pi^+\pi^+\pi^-$	$(5.7 \pm 0.5) \times 10^{-3}$
$D^+ \to K^0_S\pi^+$	$(1.562 \pm 0.031)\,\%$
$D^+ \to K^0_S\pi^+\pi^0$	$(7.36 \pm 0.21)\,\%$
$D^+ \to K^0_S\pi^+\pi^+\pi^-$	$(3.10 \pm 0.09)\,\%$
$D^+ \to K^0_S K^+$	$(3.04 \pm 0.09) \times 10^{-3}$
$D^+ \to K^+K^-\pi^+$	$(9.68 \pm 0.18) \times 10^{-3}$
$D^+ \to \pi^+\pi^0$	$(1.247 \pm 0.033) \times 10^{-3}$
$D^+ \to \pi^+\pi^+\pi^-$	$(3.27 \pm 0.18) \times 10^{-3}$

Table 6.2.: All considered neutral and charged D meson decay channels and their PDG branching ratio [70].

Furthermore, the multiplicity of particles considered for the reconstruction differs quite a lot with at least two particles up to a maximum of five particles for the reconstruction of the D mesons.
Besides, the branching ratio for the different decay channels is very different.
A loose selection cut on the invariant mass of the neutral and charged D meson in the range of $1.84 < M < 1.89\,\mathrm{GeV}\,c^{-2}$ is performed.
It is observed that some modes are reconstructed with higher efficiency than others, therefore a selection of the considered D meson decay channels is performed for the different B mesons. This results in an improvement of the number of correctly reconstructed D mesons and is directly linked to a purer D^{**} meson reconstruction, even though the amount of statistics decreases.
Further information about the performed study as well as the results are given in section 6.8.

6.4.2. Neutral and charged D^* meson reconstruction

In some cases (see section 2.3), it is also possible for the D^{**} meson to decay into a D^* meson before the D^* meson can then further decay into a D meson, therefore modes with $D^{**} \to D^*\pi$ are also reconstructed. As the D^* meson is an excited D meson it can either decay via the strong or the electromagnetic force into the ground state, the D meson, again.
The considered decay channels for the neutral and charged D^* mesons can be found in table 6.3, including their PDG branching ratio values [70].
The decay $D^{*0} \to D^+\pi^-$ is not allowed, because of phase-space availability, which means that the masses of the D^+ and the π^- meson are larger than the mass of the D^{*0}.

Decay channel	Branching ratio
Neutral	
$D^{*0} \to D^0\pi^0$	$(64.7 \pm 0.9)\,\%$
Charged	
$D^{*-} \to \bar{D}^0\pi^-$	$(67.7 \pm 0.5)\,\%$
$D^{*-} \to D^-\pi^0$	$(30.7 \pm 0.5)\,\%$

Table 6.3.: Reconstructed neutral and charged D^* meson decay channels considered for this analysis and their corresponding PDG branching ratio [70].

The mass difference ΔM between the D^* and the D meson is very small, which leaves the neutral or charged π meson with only a very low momentum, as the phase space is highly limited. Due to its low momentum, the π meson is usually called "slow pion".
To only get the best D^* meson candidates, a selection cut on the mass difference ΔM in the range of 130 to $150\,\mathrm{MeV/c^2}$ is conducted for the neutral slow pions. For the charged slow pion an even tighter selection cut in the range of 141 to $150\,\mathrm{MeV/c^2}$ is applied.

The reason for making such a distinction in the selection is simply that the charged track can be measured much more precisely than the low energetic cluster depositions of the photons for the neutral slow pions.
The electromagnetic decay $D^{*0} \to D^0\gamma$ is also allowed for the D^* meson. It was also investigated for this analysis to include this decay channel for the reconstruction of the D^{*0}, however this resulted in a lot of additional D^* meson candidates due to the huge number of measured photons in the Belle II detector that yielded many combinatorial wrong candidates. Besides, these candidates do not have a really good resolution due to the additional photon. Therefore, it was decided to exclude this decay channel and focus on a more clean reconstruction, which is of particular interest for the D^{**} mesons.

6.4.3. Neutral and charged B_{Sig} reconstruction

For the reconstruction of the B_{Sig} meson, different combinations of the final state and intermediate particles are considered.
For the reconstruction of the D^{**} meson different combinations of neutral and charged $D^{(*)}\pi$ are formed. These are then combined with a light charged lepton to form a B meson candidate. The reconstruction modes considered for the neutral and charged B_{Sig} meson can be seen in table 6.4.

Decay channel	$\Delta M_{D^{**}}$ [GeV c^{-2}]
Neutral	
$B^0 \to \boldsymbol{D^-\pi^0}\ell^+\nu_\ell$	0.15
$B^0 \to \boldsymbol{D^{*-}\pi^0}\ell^+\nu_\ell$	0.19
$B^0 \to \boldsymbol{\bar{D}^0\pi^-}\ell^+\nu_\ell$	0.25
$B^0 \to \boldsymbol{\bar{D}^{*0}\pi^-}\ell^+\nu_\ell$	0.35
Charged	
$B^+ \to \boldsymbol{\bar{D}^0\pi^0}\ell^+\nu_\ell$	0.19
$B^+ \to \boldsymbol{\bar{D}^{*0}\pi^0}\ell^+\nu_\ell$	0.15
$B^+ \to \boldsymbol{D^-\pi^+}\ell^+\nu_\ell$	0.25
$B^+ \to \boldsymbol{D^{*-}\pi^+}\ell^+\nu_\ell$	0.30

Table 6.4.: Considered neutral and charged B meson decay channels for this analysis, where the D^{**} mesons are printed in **bold** and the ℓ can either be an electron or a muon. In addition to this, also the lower selection cut on the variable $\Delta M_{D^{**}}$ is provided.

The different D^{**} mesons are not explicitly reconstructed. Although all of them have been observed as summarised in [70], the data set taken by the Belle II detector so far is not yet well enough understood to distinguish between their origin.
In addition to these signal decay channels, also the normalisation channel $B \to D^*\ell\nu_\ell$

is reconstructed. It is used to normalise the branching ratio of the D^{**} mesons, so that certain systematic uncertainties cancel out. This decay also occurs much more often and is better understood. Besides, it can be used as a cross-check for e.g. the fit setup.
The considered decay channels for the normalisation mode can be seen in table 6.5.

Decay channel
Neutral
$B^0 \to D^{*-}\ell^+\nu_\ell$
Charged
$B^+ \to \overline{D}^{*0}\ell^+\nu_\ell$

Table 6.5.: All considered neutral and charged B meson decay channels for the normalisation mode, where the ℓ can either be an electron or a muon.

In the D^{**} meson reconstruction, a lower selection cut on the invariant mass of the $D^{(*)}\pi$ pair of $2.05\,\mathrm{GeV}\,c^{-2}$ to suppress background events arising from $B \to D^*\ell\nu_\ell$, is performed. An additional upper selection cut of $2.80\,\mathrm{GeV}\,c^{-2}$ is applied due to the assumed D^{**} meson masses.
The first selection cut, the lower invariant mass cut, is inverted and used for the normalisation mode $B \to D^*\ell\nu_\ell$ as an upper cut on the invariant mass of the D^* meson. This automatically results in two statistically independent samples, which is important later, when calculating the ratio of the signal and the normalisation mode.
There still exists a significant amount of background in the signal mode after applying these selection cut. Therefore, an additional selection on the resolution of the second daughter of the D^{**} meson, meaning either the charged or neutral pion, is conducted. For this reason, the variable $\Delta M_{D^{**}}$ is defined as $\Delta M_{D^{**}} = M(D^{(*)}\pi) - M(D^{(*)})$ using the reconstructed masses of the $D^{(*)}\pi$ pair and the $D^{(*)}$. The upper selection cut on $\Delta M_{D^{**}}$ is kept the same for all considered D^{**} decay modes with $0.9\,\mathrm{GeV}\,c^{-2}$, whereas the lower selection cut is chosen so that most of the wrongly reconstructed candidates are removed.
Two example distributions for the motivation of the lower selection on $\Delta M_{D^{**}}$ can be found in fig. 6.2. All selections have been applied except for the selection on the resolution of the D^{**} meson and the best candidate selection. The candidates with the fainter colour below the dashed line are removed.
It can be seen that particularly for the mode in the histogram on the left-hand side a significant amount of $B \to D^*\ell\nu_\ell$ is removed, whereas the other $B \to D^{**}\ell\nu_\ell$ decay mode including a neutral pion has a worse resolution in $\Delta M_{D^{**}}$ and thus the selection cut cannot be chosen tighter.
The chosen values for the lower selection cut on $\Delta M_{D^{**}}$ for all $B \to D^{**}\ell\nu_\ell$ decay modes can be found in the right column in table 6.4.

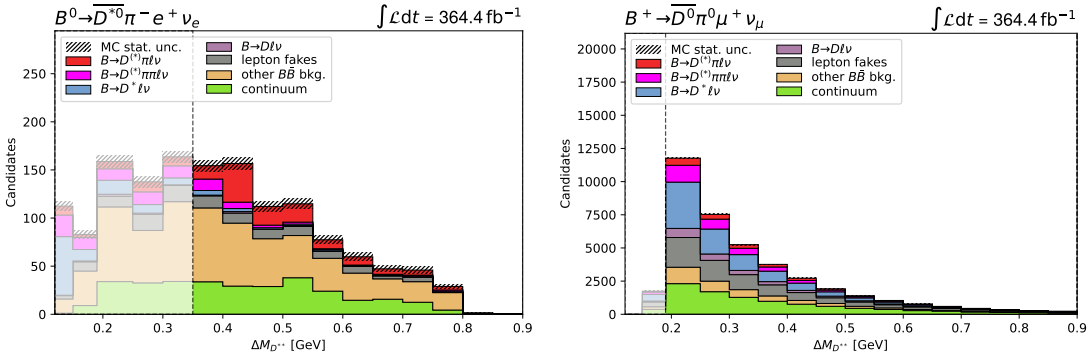

Figure 6.2.: Histograms motivating the lower cut on the variable $\Delta M_{D^{**}}$ for two example decay modes that can be found in the title of the plot. All selection cuts except for the $\Delta M_{D^{**}}$ and the best candidate selection have been applied.

6.4.4. Neutral and charged B_{Tag} reconstruction

For the reconstruction of the tag-side B meson, the hadronic Full Event Interpretation is used. By choosing only the hadronic decay modes for the reconstruction, the four-momentum of the B_{Tag} meson can be precisely measured and thus the resulting purity of the tagged sample is very high. However, the efficiency is about $\mathcal{O}(0.1\,\%)$ and therefore very small.

For a general overview and additional information on the FEI, please refer to section 5.2.1. The FEI outperforms its predecessor, the FR, in many ways. Nonetheless, there are some significant observed performance differences between measured and generated data, which are discussed further later in section 6.9.6. Therefore, it is important to do extensive studies of well-known physics processes and determine calibration factors using physical properties to account for these performance differences.

Due to the fact that these calibration factors have been determined using a certain selection, these selection cuts need to be reproduced exactly. This means, however, that the tag-side can not be optimised for one particular decay channel on the signal side, which reduces the reconstruction efficiency drastically.

For the current version of the trained hadronic FEI, there exist calibration factors for two different working points for the output of the FEI. As a consequence of the low branching ratio of the D^{**} mesons, the lowest possible working point of the FEI with a classifier output of more than 0.001 is chosen, which means a high efficiency.

To align the selection of this analysis with the selection used for the calibration factor determination and also increase the number of correctly reconstructed B_{Tag} meson candidates, some basic kinematic properties of B factories are exploited.

For correctly reconstructed B_{Tag} meson candidates, the measured reconstructed mass should correspond to the mass of the B meson. Besides, the total energy of one of the two B mesons should match half of the beam energy in the frame of the $\Upsilon(4S)$ resonance $E_{\text{beam,CMS}}$. Here, the rest frame of the $\Upsilon(4S)$ is defined as the CMS of the two colliding

beams.
One could directly use these quantities, however two slightly modified variables, the energy difference ΔE and the beam-constrained mass M_{bc} are favoured. Both these quantities are highly dependent on a very precise knowledge of the beam energy.
The definition of ΔE is given by the following:

$$\Delta E = E_{B_{\mathrm{Tag}},\mathrm{CMS}} - E_{\mathrm{beam,CMS}}, \tag{6.3}$$

where $E_{B_{\mathrm{Tag}},\mathrm{CMS}}$ simply refers to the energy of the B_{Tag} meson in the CMS frame.
The beam-constrained mass M_{bc} is defined as follows:

$$M_{\mathrm{bc}} = \sqrt{E^2_{\mathrm{beam,CMS}}/c^4 - |\vec{p}_{B_{\mathrm{Tag}}}|^2/c^2}, \tag{6.4}$$

where $\vec{p}_{B_{\mathrm{Tag}}}$ is the momentum vector of the reconstructed B_{Tag} meson candidate in the CMS frame.
Compared to the naive kinematic definitions using the mass and the energy of the reconstructed B_{Tag} meson, the altered variables also take into account the resolution of certain detector components, as can be seen in eq. (6.3). ΔE is highly dependent on the particle hypotheses used to build a B meson candidate as well as on the detector resolution to determine $E_{B_{\mathrm{Tag}},\mathrm{CMS}}$.
By using a wrong combination of daughter particles the value of ΔE is shifted from its nominal value of zero.
M_{bc}, in contrast, is independent of the mass hypothesis for the final state particle as only the momentum measurement of the final state particles is required to calculate this variable. Furthermore, M_{bc} can be used to distinguish combinatorial background, meaning hadronisation processes of the light quark pairs from B meson candidates that were reconstructed using the correct detector objects.
The candidates built using light quark pairs are expected to spread uniformly in the allowed kinematic range, whereas the correctly reconstructed B meson candidates are expected to peak at the nominal B meson mass.
To remove wrong B_{Tag} meson candidates a selection cut on the energy resolution in the range $-0.15 < \Delta E < 0.10\,\mathrm{GeV}$ and on the beam-constrained mass M_{bc} with a value of above $5.27\,\mathrm{GeV}\,c^{-2}$, is applied.
After these selections, still a considerable amount of background arising from light quark pair interactions remains. This can, however, be further suppressed by taking into account differences in the topological properties of $\Upsilon\,(4S) \to B\overline{B}$ decays and processes of the nature $e^-\,e^+ \to q\,\bar{q}$ with $q \in \{u, d, c, s\}$, i.e. the light quark pair interactions.
In case of light quark pair interactions, the q and $\bar{q}$ are created back-to-back in the centre-of-mass frame and each quark carries almost half of the beam energy. Therefore, the resulting hadrons during the fragmentation process obtain only a small momentum in the transverse plane. Hence, the particles show a jet-like structure after hadronisation. Compared to that, for the $B\overline{B}$ events, the B mesons are produced nearly at rest in the CMS frame. As the B meson is a pseudo-scalar particle i.e. spin-0 particle, the decay products of the B meson have no directional preference and are therefore distributed

isotropically in the detector volume. A schematic showing these differences can be seen in fig. 6.3.

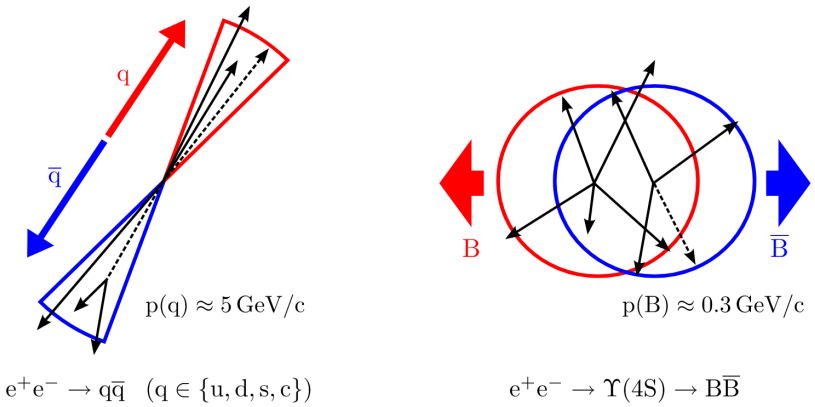

Figure 6.3.: Schematic of the different event topologies in the CMS system for the light quark pair on the left-hand side, where the light quarks are produced back-to-back in pairs in the $e^- e^+$ annihilation, which results in a jet-like structure. Whereas the $B\overline{B}$ shows a spherical shape on the right-hand side. Taken from [153].

One quantity that exploits these differences in the event topology is the thrust, which has already been developed in the 1980s by the PEP and PETRA accelerators for a quantification of jets at high energy experiments [154].
The definition of the thrust axis $\vec{T}$ is given by the direction in which the sum of the longitudinal momenta of all measured particles is maximised. The thrust T is described by the following formula:

$$T = \max_{\vec{x}} \frac{\sum_i |\vec{p}_i \cdot \vec{x}|}{\sum_i |\vec{p}_i|}, \tag{6.5}$$

where $\vec{p}_i$ is the momentum vector of the i-th final state particle in an event and the maximisation is done over all possible directions $\vec{x}$ with $|\vec{x}| = 1$ [154]. The thrust axis $\vec{T}$ is the axis $\vec{x}$ multiplied by T for which the thrust is maximal.
For the light quark pairs, the thrust leads to higher values ($T \to 1$), as the event shape has a strong directional preference, whereas for the $B\overline{B}$ events, the thrust prefers minimal values with $T \to 0.5$ as the decay products are isotropically distributed in the event. The variable used to distinguish these two processes is the cosine of the angle between the trust axis of the reconstructed B_{Tag} meson candidate $\vec{T}_{\text{B}}$ and the thrust axis of all remaining particles in an event that are not assigned to the reconstructed B_{Tag} meson candidate $\vec{T}_{\text{O}}$, $\cos(\vec{T}_{\text{B}}, \vec{T}_{\text{O}})$.
For the B meson decays at rest, a uniform distribution is expected, whereas for the decay products of the highly boosted lighter particles, the thrust axes are collinear, which produces a peak towards one. This means by using a selection cut of $\cos(\vec{T}_{\text{B}}, \vec{T}_{\text{O}}) < 0.9$

a significant amount of continuum background is removed.
In addition to this, there exist the so called Fox-Wolfram moments [155]. These quantities can be used to define the shape of an event and without making a distinction between signal- or tag- side particles in an event. The definition of the l^{th} Fox-Wolfram moment H_l is given by the following expression:

$$H_l := \sum_{i,j}^{N} |\vec{p_i}||\vec{p_j}| P_l(\cos(\theta_{i,j})), \tag{6.6}$$

where the sum goes over all particle pairs i, j up to the overall amount of particles N in an event. $\cos(\theta_{i,j})$ is the angle between the momentum of the ith and jth particle and P_l corresponds to the Legendre polynomial of order l.
Due to the fact that the Legendre polynomial of order 0 is $P_0 = 1$, a constant, the lowest-order Fox-Wolfram moment is usually considered to normalise the other moments.
Of particular interest is the second-order moment, which is defined as:

$$R_2 = \frac{H_2}{H_0}. \tag{6.7}$$

For even l $q\bar{q}$ events show a peak at one, whereas for odd l, they produce a peak at zero. Other processes give a wide range of values for R_l.
Therefore, this is another important variable to discriminate between $B\overline{B}$ and $q\bar{q}$ events. However, there has been a noticeable observed disagreement in this variable between simulation and data. Therefore, this variable was removed from the selection.

6.4.5. $\Upsilon(4S)$ reconstruction

After the reconstruction of B_{Sig} and B_{Tag} meson candidates, these particles can be combined to form a neutral $\Upsilon(4S)$ candidate.
The three reconstructed $\Upsilon(4S)$ decay modes are summarised in table 6.6, where the last option also takes into account mixing in the neutral B meson system.

Decay channels
$\Upsilon(4S) \to B^{-}_{\text{Tag}} B^{+}_{\text{Sig}}$
$\Upsilon(4S) \to B^{0}_{\text{Tag}} \overline{B}^{0}_{\text{Sig}}$
$\Upsilon(4S) \to B^{0}_{\text{Tag}} B^{0}_{\text{Sig}}$

Table 6.6.: Considered $\Upsilon(4S)$ decay modes for this analysis including mixing in the neutral B meson system.

In addition to these three reconstruction modes of the $\Upsilon(4S)$, the reconstruction of the $\Upsilon(4S)$ with a charge was also investigated, e.g. combine a charged B_{Tag} meson candidate and a neutral B_{Sig} meson candidate. The idea was that this approach would account for missed charged tracks in the reconstruction. However, after extensive studies this proposal was discarded, as it accumulated more wrongly reconstructed $\Upsilon(4S)$ candidates than correctly built candidates.

6.5. Rest-of-Event selection

After the combination of the B_{Sig} and B_{Tag} meson candidates to an $\Upsilon(4S)$ candidate, the "completeness constraint" can be imposed on this event.
One can look for particles not considered in the reconstruction of the $\Upsilon(4S)$ candidate. These additional particles are called "Rest of Event" (ROE). For the ideal case, there should not be any particles left in the event, as the event is completely reconstructed. However, there might be tracks or clusters that were not used in the $\Upsilon(4S)$ reconstruction and might be a hint for wrongly reconstructed $\Upsilon(4S)$ candidates. However, particle candidates in the ROE could also originate from material interactions with the detector or simply fake particles. Therefore, a clean-up on the ROE particles is performed to remove such particle candidates. This selection is based on [156].
The tracks in the ROE need to be within the CDC acceptance region and stem from close to the IP with $dr < 1\,\text{cm}$ and $|dz| < 3\,\text{cm}$. Besides, tracks that are likely to originate from low-momentum particles curling in the tracking detectors are rejected, because there exists a high change of reconstructing them as duplicate track candidates. This rejection of curling tracks is based on a pre-trained MVA selector [157] to recognise curling tracks using Belle II data for the training.
For the clusters in the ROE, the ECL-region-dependent selection values are given in table 6.7.

cluster region	track p_{T}	`clusterZernikeMVA`
Forward	$0.02\,\text{GeV}\,c^{-1}$	0.35
Barrel	$0.03\,\text{GeV}\,c^{-1}$	0.15
Backward	$0.02\,\text{GeV}\,c^{-1}$	0.4

Table 6.7.: Selection criteria for the Rest-of-Event using different ECL regions, minimal values for the transverse momentum p_{T} and the multivariate classifier value `clusterZernikeMVA`.

The shower shape, which is the total energy deposit and distribution between ECL crystals, can be used to distinguish between different particle types as the radiation lengths differ. This difference can be exploited using MVA methods for example using the moments of the Zernike polynomials with further information given in [158]. This approach is already implemented in BASF2 and can be directly used by considering the variable `clusterZernikeMVA`.
After the cleaning of the ROE, one additional selection cut is applied on the number of tracks in the ROE. For a correctly reconstructed $\Upsilon(4S)$ candidate, there should not remain any tracks in the ROE. Therefore, this region is referred to as the "signal region", where the determination of the branching ratio will take place.
The region, where one or more additional tracks have been found in the ROE is called "sideband region" and is used later on to investigate the agreement between simulated and experimental data, see chapter 7.

Another discriminating variable for background suppression of neutral particles in the event is the sum of energy depositions found in the ROE, called $E^{\mathrm{ECL}}_{\mathrm{Extra}}$. However, due to bad modelling of this variable in the generated samples, this variable is not considered in this analysis. The reason for the seen disagreement might be that the energy depositions within the particle beam are harder to simulate due to the higher instantaneous luminosity at Belle II.
After the selection on the number of tracks in the ROE a cut on the missing mass m^2_{miss} variable is performed, where the definition can be found in eq. (7.3). Further information regarding this variable are given in section 7.3 and section 8.2.
The applied selection is $-1 < m^2_{\mathrm{miss}} < 2\,\mathrm{GeV}\,c^{-2}$.

6.6. Best candidate selection

After all these selection cuts have been applied, it is still possible that there exists more than one reconstructed $\Upsilon\,(4S)$ candidate per event. However, in reality there is only one $\Upsilon\,(4S)$ resonance decaying into one $B\overline{B}$ pair.
Depending on the reconstructed mode, there are on average between two and five candidates before the best candidate selection (BCS). The most candidates are found for modes, where the D^{**} meson is reconstructed using neutral pions. For modes, where the D^{**} meson is built from combinations of $D^{(*)}\pi^+$ mesons, the multiplicity of candidates in an event is already close to one on average.
To select a best candidate special care has to be taken, as it can easily happen that correctly reconstructed candidates are discarded. In addition, by considering a ranking based on an invariant mass, the resulting distribution after the BCS for the extraction of the branching ratio might show a peaking background structure, which would make it harder for the fit to discriminate the different shapes of signal and background.
The first step in the BCS is to look for the B_{Tag} meson candidate with the highest FEI output for both the signal and the normalisation mode. However, it is often possible that there exist still more than one candidate due to multiple B_{Sig} candidates. Thus, for the $B \to D^{**}\ell\nu_\ell$ reconstruction mode, the $D^{**} \to D^*\pi$ decay channels are favoured over the reconstructed $D^{**} \to D\pi$ decay modes. By preferring the reconstruction of the process $D^{**} \to D^*\pi$, the resolution of the resulting D^{**} mesons is improved as the reconstruction of the D^* meson, due to the slow pion, has a more distinct signature in the detector.
For the case that there is still more than one reconstructed candidate per event left, the absolute difference between the reconstructed and the nominal mass of the first daughter of the D^{**} meson, meaning either the D^* or the D meson, is chosen to reduce the multiplicity in each event to one. In case of the normalisation mode, the reconstructed D^* meson is used directly instead of the first daughter in the D^{**} meson reconstruction. The mass difference should be unique for each candidate. In the rare instances, when this is not the case, a random candidate is chosen.
As already mentioned, it is important to study the impact of a BCS based on a mass variable. Therefore, a study has been performed to investigate, if the selection of a best

candidate based on the mass difference results in a peaking background of the fit variable. This has been done by comparing the shapes of the different background categories for the fit variable before applying the last step of the BCS and after. The comparison of shapes showed no sign for an increase in peaking background, thus the mentioned BCS can be applied.

6.7. MC matching

After the whole procedure for the reconstruction of the $\Upsilon(4S)$ resonance has been performed as described in the previous sections, the reconstructed $\Upsilon(4S)$ events can be classified into different categories based on their generator-truth information.
To do so, the reconstructed objects are compared with the generated objects in simulation.
The following section will describe the classification of the simulated sample into different signal and background categories starting with the generator information of the reconstructed signal lepton.

6.7.1. Signal components

For the truth-matching the decay tree on generator level is traversed starting with the reconstructed light charged lepton. For an $\Upsilon(4S)$ candidate to be classified into the signal component, meaning $B \to D^{**}\ell\nu_\ell$, the following criteria need to be met:

True lepton The reconstructed lepton can be matched to a light charged lepton on truth-level and this lepton originates from a B meson, which is used as the generator signal B meson referred to as $B_{\text{Sig}}^{\text{Gen}}$.

True $B_{\text{Sig}} \to D^{**}$ The first daughter of the generator-level $B_{\text{Sig}}^{\text{Gen}}$ is a D^{**} meson. Furthermore, it is required that the $B_{\text{Sig}}^{\text{Gen}}$ meson does not have any additional daughters except for the charged lepton, the neutrino and final state radiation photons.

Not continuum This requirement ensures that the $\Upsilon(4S)$ candidate does not originate from a continuum or off-resonance simulated data set.

The signal component can then be further sub-divided into D^{**} mesons decaying into a D or D^* meson and one or two additional π mesons, due to the fact that this analysis focusses on the measurement of the branching ratio into a $D^{(*)}$ mesons plus one additional pion. This is later on also considered in the fit by the usage of two templates for both pion multiplicities, as detailed in section 8.2.
In the considered MC matching for this analysis, the decays of the D and D^* mesons are not explicitly taken into account on generator level. This means that the truth-matching allows for mis-reconstructed D or D^* mesons in the D^{**} meson reconstruction.
The advantage of this approach is a non-peaking background in e.g. the fit variable. This might occur when reconstructed B_{Sig} meson candidates have a missed particle in

the reconstruction chain, such as a π_{slow}, but still peak at the expected value. On top of this, the amount of statistics is increased and therefore also the efficiency.
The disadvantage is, however, a lower signal resolution, which results in smeared out variable distributions.
Furthermore, the B_{Tag} meson, meaning the reconstruction of the tag-side B meson using the hadronic FEI is not required to fulfil any specific generator-truth level conditions. Only the B_{Sig} meson candidate needs to fulfil the above defined signal requirements.

6.7.2. Background components

If the reconstructed candidate is not correctly reconstructed, there are different background categories that it can be classified into, depending on the generator information. The background categories considered for this analysis are defined as follows:

Continuum The reconstructed candidates originate from a simulated continuum or off-resonance MC simulation. For all the other background categories it is explicitly demanded that the reconstructed candidates do not originate from a continuum sample.

$B \to D\ell\nu_\ell$ This category is almost identical to the signal category. The only difference is that the "sister" of the true lepton, meaning the first daughter of the $B_{\text{Sig}}^{\text{Gen}}$, is a D meson instead of a D^{**} meson.

$B \to D^*\ell\nu_\ell$ This is also almost equal to the signal category, only this time the sister of the true lepton is a D^* meson.

Lepton fakes This category comprises reconstructed charged leptons that cannot be matched to a charged lepton on generator level, meaning that the reconstructed particle is presumably a hadron.

Other $B\bar{B}$ background This last category summarises all the reconstructed candidates that do not match the signal definition neither can it be classified into any of the categories mentioned above. This means especially that the reconstructed candidates still originate from a $B\bar{B}$ event but not from the continuum sample.

6.8. D meson decay study

In general, there exist many different possibilities to hadronically reconstruct neutral and charged D mesons, where the ones considered for this analysis can be found in table 6.2.
To compare the importance of each reconstructed D meson decay channel for the reconstruction of a single B meson, a figure of merit (FOM) is defined. The FOM used in this case is given by FOM$= S/\sqrt{S+B}$, where S corresponds to the number of generated signal events and B is the number of background events. The value of the FOM will increase as more signal and less background is selected. It is a rough measure for the

expected sensitivity of the analysis.
In this analysis, the signal category is not further sub-divided. This means that the full reconstructed B meson decay channel is not explicitly compared to the generated one, but rather it is tested that the reconstructed decay is on generator level a resonant $B \to D^{(*)}\pi\ell\nu_\ell$ decay with arbitrary $D^{(*)}$ sub-decay.
Before the actual study, based on the FOM, has been performed, the mass distributions of the D meson for simulated and experimental data have been compared. Some modes have already been excluded here due to observed differences between simulation and data for both the signal and the normalisation mode. Besides, modes with only a few reconstructed events were also dropped.
Due to the high purity of the $B \to D^*\ell\nu_\ell$ sample after the discardment of the D meson decay channels with bad modelling in the simulation, no further optimisation of the normalisation mode based on the D meson decay channels is performed.
The D meson study is performed only for the $B \to D^{**}\ell\nu_\ell$ signal channels. At first, the FOM is calculated once for each reconstructed B meson decay channel including all D decay modes. Then one D meson decay mode is excluded one at a time and the FOM is determined again.
The results can be seen in fig. 6.4a for an example decay mode using an electron as the light charged lepton and in fig. 6.4b by taking the muon. The histograms for all other reconstructed B meson decay channels can be found in appendix A.

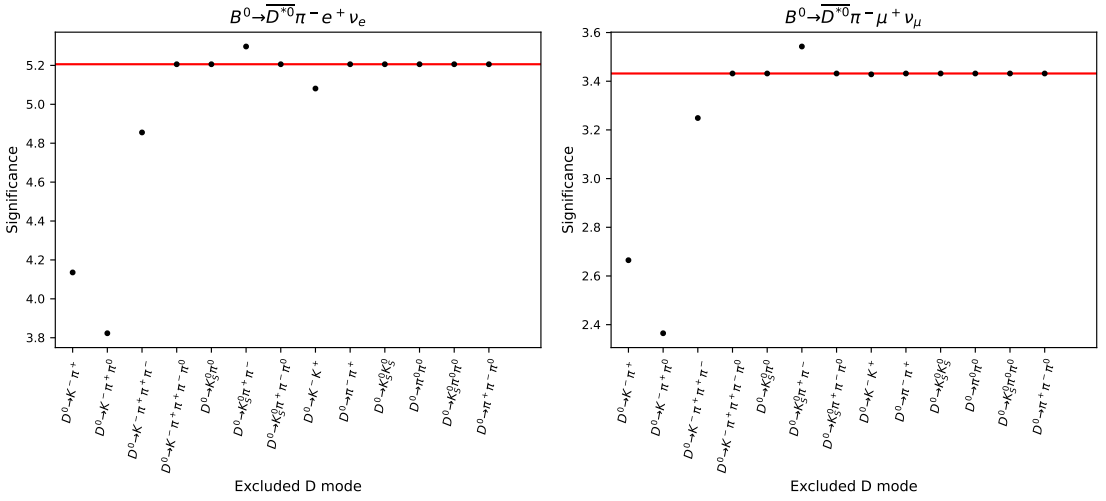

(a) Electron (b) Muon

Figure 6.4.: Histograms showing the significance for one particular reconstructed B meson as stated in the title, where the light charged lepton is the electron on the left-hand side and the muon on the right-hand side. The overall significance is portrayed by the red line and the excluded reconstructed D meson decay mode is shown on the x-axis.

The red line in the histograms symbolises the overall significance of the B meson decay channel in the title of the histogram and the different points show the significance, when the decay mode shown on the x-axis is removed from the calculation of the FOM. This means if after the exclusion of a D meson decay channel the significance is the same as the overall significance or even above the overall significance, the red line, the D meson decay channel can be removed from the reconstruction of the B meson without loosing sensitivity. The reason is simply that this decay channel does not contribute to the overall significance or even worsens it.
After the exclusion of the determined D meson decay channels, the overall significance increases for the B meson reconstruction since in some removed channels more wrongly reconstructed candidates than correct ones were present.
Other removed decay channels do not change the significance at all, mostly because of their small branching ratio, see table 6.2. This means however, that more data in the future might change the picture significantly.
In addition to that, it is noticeable that for the neutral D meson the decay modes of particular importance in the reconstruction are $D^0 \to K^-\pi^+$ and $D^0 \to K^-\pi^+\pi^0$ and for the charged D meson the mode $D^+ \to K^-\pi^+\pi^+$ plays a major role. These are modes that have a large branching ratio as well as only a few particles needed for the reconstruction.

6.9. Corrections to recorded and simulated data

There exist corrections that are applied to simulation to change the underlying physics model as for the form factors or include updated measurements like newer values of branching ratios, as detailed in section 4.2.1. However, there also exist correction factors that need to be applied due to the performed selection, these can be for example corrections that compensate for performance differences between experimental and simulated data such as particle identification and reconstruction or the efficiency of the hadronic FEI for the tag-side.

6.9.1. Track momentum scaling

The track momentum scaling is a correction that needs to be applied to recorded data. A shift in the invariant mass peaks [159, 160] for e.g. D^0, $D^\pm$ and the K^0_S meson has been observed between the data accumulated by the Belle II detector and the simulation that considers values from [70].
The observed shift towards lower values can be explained due to a bias in the tracking momentum, which results from a biased magnetic field map used for the data reconstruction. Currently, the magnetic field map is not finalised yet and therefore a run-dependent scale factor is used as a correction. The determination of the scale factor is done by iteratively fitting the D^0 mass in the decay $D^{*+} \to [D^0 \to K^-\pi^+]\pi^+$ while taking into account the changed three-momentum of the daughter particles originating from tracks that are affected by a changed magnetic field map.

6.9.2. Energy bias corrections

Like the previous correction, the energy bias correction is also applied to the experimental data to account for an observed shift in the photon energy [161] between data and simulation, which directly results in an invariant mass shift of the π^0 mesons.
For the determination of the corrections, the symmetric decays of the nature $\pi^0 \to \gamma\gamma$ and $\eta \to \gamma\gamma$ in the range of the photon energy between 0.02 to 2.00 GeV are used [162].

6.9.3. Particle ID corrections

After the application of the lepton identification or hadron identification algorithm also differences between MC and experimental data have been observed for the efficiencies, but also for misidentification rates of these particles as well. These differences are dependent on momentum and on the polar angle of the associated track and are therefore applied as weights to the simulated particle candidates based on angle and momentum. The efficiency factors are applied in case a reconstructed object can be correctly matched to a generated object, whereas misidentification factors are used if the simulated candidate is not reconstructed correctly.
For the determination of the efficiency factors of the lepton identification, the following four processes [163] are used $J/\psi \to \ell^+\ell^-$, $e^-e^+ \to e^-e^+(\ell^+\ell^-)$, $e^-e^+ \to e^-e^+(\gamma)$ and $e^-e^+ \to \mu^-\mu^+(\gamma)$.
The combination of these four processes spans a wide range in lab momentum p_{lab} and the polar angle θ of the leptons, as each process dominates in a certain region, thus the combination maximises the coverage and minimises the uncertainties.
A tag and probe method is considered for the determination of the efficiency for each process separately. To do so, the tag sample is chosen based on the invariant mass of the two lepton candidate tracks and event shape variables to make sure that a pure lepton sample is selected. Here, the probe sample is a subset of the tag sample with a selection cut on the lepton identification requirement.
The efficiency ε can be calculated as following:

$$\varepsilon = \frac{N_{\text{pass}}^{\text{Sig}}}{N_{\text{pass}}^{\text{Sig}} + N_{\text{fail}}^{\text{Sig}}}, \tag{6.8}$$

with $N_{\text{pass}}^{\text{Sig}}$ being the number of events that pass the lepton identification requirement and $N_{\text{fail}}^{\text{Sig}}$ the number of events that fail the lepton identification requirements, respectively.
The correction factor is determined by taking the ratio of the efficiencies ε between data and simulation. This factor is usually close to one.
Besides, the simulated sample needs to be corrected for hadrons, meaning charged pions or kaons that are misidentified as leptons, where the correction factors are further away from unity.
Here, the tag and probe method is used again. For the pion misidentification factors the following two decay channels are considered $K_S^0 \to \pi^+\pi^-$ as well as the tau decay into one or three charged pions. In contrast to this, for the charged kaon misidentification

factor the decay $D^{*+} \to (D^0 \to K^-\pi^+)\pi^+$ is used.
To determine the hadron identification efficiency and misidentification rates [164], a tag and probe method using the same physical processes as for the determination of the correction of their misidentification as leptons are used.
For each PID correction there exists an associated statistical and systematic uncertainty.

6.9.4. Slow charged pion corrections

In the decay $D^{*+} \to D^0\pi^+$, the π^+ has a low momentum and is thus harder to reconstruct. The slow momentum track efficiency is essential to account for the difference between data and simulation in the range from 0.05 to 0.20 GeV c^{-1}. The resulting systematic uncertainty associated to this correction is one of the leading systematic uncertainties in similar analyses, e.g. [165].
The corrections [166] are provided in bins of pion momentum. To determine these corrections, the decay $B^0 \to D^{*-} \to (D^0 \to (K^-\pi^+, K^-\pi^+\pi^+\pi^-, K^0_S\pi^+\pi^-)\pi^-)\pi^+$ is considered, where a two-dimensional fit in bins of ΔE and ΔM, the mass difference between D^* and D^0, is used.
Similar to the PID corrections, the correction factor is provided with a statistical and systematic uncertainty.

6.9.5. Neutral pion efficiency corrections

Compared to the charged π, the π^0 is built from a pair of energy depositions in the calorimeter, which are less well-measured. Therefore, there are also efficiency corrections available for the π^0 mesons. These, however, need to be split further into the nominal and slow π^0 efficiency corrections.

Nominal neutral pion

For the nominal neutral pion, the efficiency corrections [167] are determined in momentum bins in the range from 0.2 to 3.0 GeV c^{-1} using the decay channels $D^0 \to K^-\pi^+\pi^0$ and also $\tau \to 3\pi^\pm\pi^0\nu_\tau$. The correction factors are determined by comparing the D^0 or the π^0 mass peak between data and simulation.
At the end, there exists one correction factor that needs to be applied to simulated data. It originates from the D^0 method with an additional systematic uncertainty to account for the difference in the determination of both these methods.

Slow neutral pion

To determine the corrections for the slow neutral pion [167] in the momentum range 0.05 to 0.20 GeV c^{-1} relative to the bin 0.2 to 0.4 GeV c^{-1} the decay $B^+ \to (D^{*0} \to (D^0 \to K^-\pi^+)\pi^0)\pi^+$ is used. The correction factor is measured by comparing the mass difference between the charged D^* meson and the neutral D meson. These corrections also have associated systematic and statistical uncertainties.

6.9.6. Tagging efficiency correction

As already mentioned in section 6.4.4, there exist some performance differences between experimental and simulated data for the FEI that need to be corrected by a calibration factor:

$$\kappa_{\mathrm{FEI},i} := \frac{N_{\mathrm{Data},i}}{N_{\mathrm{MC},i}}, \tag{6.9}$$

for the reconstructed FEI channel or the combination of reconstructed channels i.
To determine the correction factors $\kappa_{\mathrm{FEI},i}$ for different working points of the FEI output two different independent decay channels are investigated.
The first method uses an inclusive approach by reconstructing semi-leptonic B meson decays [168] and the other method does a partial reconstruction of the decays $B \to D^{(*)}\pi$ [169]. At last, a combination [170] of the two methods is achieved by doing a χ^2 parameter estimation.

Semi-leptonic calibration method

After the reconstruction and best candidate selection of the B_{Tag} meson as detailed in section 6.4.4, the reconstructed tag-side is combined with a light charged lepton that possesses a momentum above $1.0\,\mathrm{GeV}\,c^{-1}$ in the B meson rest frame.
After the categorisation of the reconstructed B_{Sig} meson candidates based on simulated data into different truth-components, a template fit using the light charged lepton momentum in the B meson rest frame as the fit variable is performed to determine the number of signal and background events in data.

Hadronic calibration method

The other calibration method uses hadronic B meson decays. As for the semi-leptonic calibration method, the reconstructed B_{Tag} meson candidate is selected according to section 6.4.4, where the best candidate is combined with a charged pion with the highest momentum in the CMS. Afterwards the recoil mass of this combination is determined. For $B \to D^{(*)}\pi^{\pm}$ decays this should peak at the $D^{(*)}$ meson mass. Therefore, the invariant mass is used to determine the number of these decays by performing a maximum likelihood fit.
Compared to the semi-leptonic calibration method, the statistics is one order of magnitude lower. However, the sample is much purer as the signal peak is much more dominant. Besides, the background level is much lower and easier to model. Therefore, the determined systematic uncertainties are smaller than for the $B \to X_c \ell \nu_\ell$ calibration method explained above.

Combination

The combination of the two determined calibration factors for each reconstructed B_{Tag} meson decay channel or subset are calculated via a χ^2 fit with further information

in [170], where the discrepancies between the two calibration methods are taken into account.

CHAPTER 7

Validation of Simulation

To test the correctness of the simulation such as the shape and the yield of the simulated data, several studies have been performed to compare how well the simulation describes the data.
This can be done using sidebands, where it is assumed that the amount of signal is negligible compared to the background. Since these sidebands are independent of the signal distribution, they do not bias the analysis and can therefore be used as a cross check of certain background categories.
The sideband considered for this analysis depends on the number of tracks in the ROE as defined in section 6.5. In case there is one or even more tracks left in the ROE, these events are defined as a sideband, which will be further investigated in section 7.1.1.
In addition to this, also the modelling of the continuum simulation is tested in section 7.1.2 by investigating off-resonance data not taken on the $\Upsilon(4S)$ resonance.
At last, some of the tag-side distributions are investigated in section 7.2 as well as signal-side variables in section 7.3 before looking at the fit variable m^2_{miss} as defined in eq. (7.3). However, due to the numerous reconstructed decay channels only a few representative distributions will be shown.

7.1. Sideband studies

Before looking at the signal region, a few checks were performed using the sideband region. Every sideband region can be used to investigate different background categories in e.g. shape and yield.

7.1.1. ROE sideband

The number of charged tracks in the ROE should be zero for correctly reconstructed $B \to D^* \ell \nu_\ell$ and $B \to D^{**} \ell \nu_\ell$ decays in the respective reconstruction. For the case that there exists one or even more tracks in the ROE of the reconstructed $\Upsilon(4S)$ resonance, it can be assumed that these events are mainly background events. These are processes, where the D^{**} meson reconstruction is wrong and thus one or more tracks remain unused in this event. Therefore, this region can be considered to investigate the agreement between the simulation and the recorded data by not biasing the analysis.
In this region various variables can be investigated, to get a clear picture on the modelling of the tag- and signal-side variables for certain background processes.

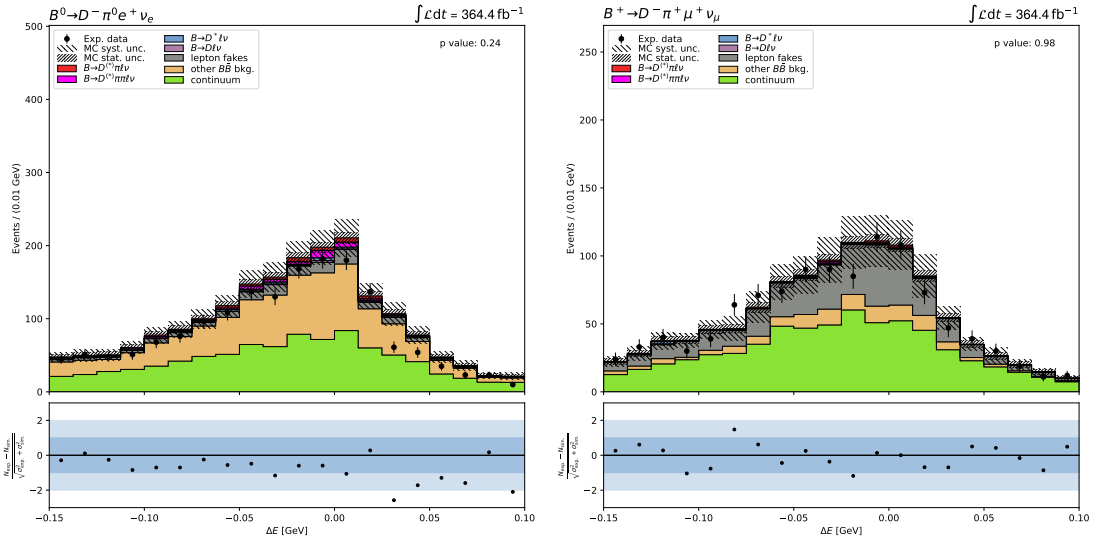

Figure 7.1.: Distributions for ΔE of the B_{Tag} meson for two $B \to D^{**} \ell \nu_\ell$ decay modes, which can be found in the title of the plots.

In fig. 7.1 ΔE (see eq. (6.3) for the definition of the variable) for two example decay modes can be seen, additional variables can be found in appendix K.
The lower part of the histograms shows the pull of the distribution, which is defined as:

$$\frac{N_{\text{exp.}} - N_{\text{sim.}}}{\sqrt{\sigma^2_{\text{exp.}} + \sigma^2_{\text{sim.}}}}, \tag{7.1}$$

where $N_{\text{exp.}}$ and $\sigma^2_{\text{exp.}}$ correspond to the number of experimental events and the associated uncertainty, $N_{\text{sim.}}$ and $\sigma^2_{\text{sim.}}$ correspond to the simulated number of events and the uncertainty. This uncertainty on the simulated samples includes the statistical uncertainty from the simulation as well as the considered systematic uncertainties, which are discussed further in section 8.5.
The differently blue coloured bands correspond to the one and two sigma confidence intervals. In case the experimental and recorded data agree well, the black points for every

bin are close to zero and thus in the one or two sigma confidence intervals. However, due to statistical fluctuations there are usually a few bins, where the deviation is a bit larger.
In all the presented plots in the top right-hand corner the p value for each distribution is presented. The p value can be calculated by first determining the χ^2 of the distribution as follows:

$$\chi^2 = \sum_b \frac{(x_{b,\text{Data}} - x_{b,\text{MC}})^2}{\sigma^2_{b,\text{Data,MC}}}, \tag{7.2}$$

where the sums runs over all bins b of the histogram and x_b corresponds to the number of events in bin b of the data or MC sample , respectively. $\sigma_{b,\text{Data,MC}}$ is the combined uncertainty on the yield of data and MC samples. Then, the difference from unity between the determined χ^2 value plugged into the cumulative χ^2 distribution function with the number of degrees of freedom being the number of bins minus one, is determined. For distributions, where a good agreement between simulation and experimental data is visible, the p value should be close to one, whereas for distributions with a small p value, the simulation does not describe the data well.
In general, however, a reasonable agreement between simulation and data is visible. Therefore, no additional steps have to be taken to account for a particular mismodelling. As already mentioned in section 6.4.4, some variables are not well described in the simulation and are therefore removed from the selection, see e.g. fig. 7.2. Even though the p value sometimes is sensible, a clear mismodelling particularly in the low R_2 region can be seen because the p value does not take systematic trends or shifts into account.

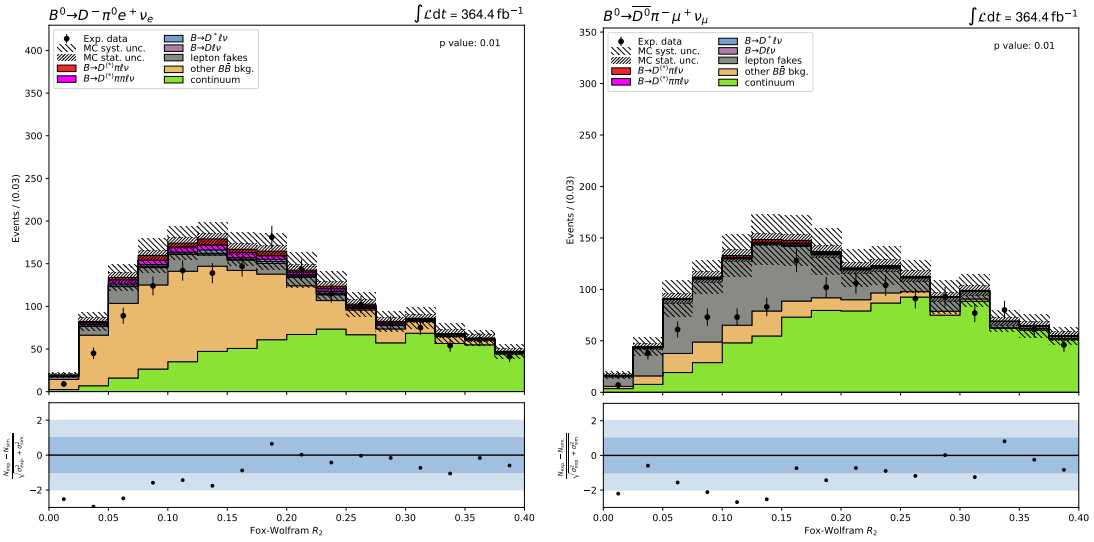

Figure 7.2.: Distributions for the R_2 variable, as defined in eq. (6.7), for two $B \to D^{**} \ell \nu_\ell$ decay modes, which can be found in the title of the plots.

7.1.2. Off-resonance data comparison

The continuum or $q\bar{q}$ processes are especially hard to model in the simulation, because of the Pythia tuning as described in section 4.2.2. Therefore special care has to be taken, when this process is an important background in an analysis.
This can be done by investigating the agreement between the recorded off-resonance data set and the continuum MC. The off-resonance data set has been collected 60 MeV below the $\Upsilon(4S)$ resonance, which means that no $B\overline{B}$ mesons pair could have been created and only light quark pairs are produced.
Different variables can be investigated after the continuum MC is scaled down to the amount of recorded off-resonance data. The recorded data set is quite small with an integrated luminosity of $42.3\,\mathrm{fb}^{-1}$ and therefore, the data points have huge statistical error bars.
Two example distributions for the region with no additional tracks in the ROE and one or more tracks can be found in fig. 7.3. Most of the other modes have even less statistics, thus these two distributions are chosen to demonstrate the agreement.

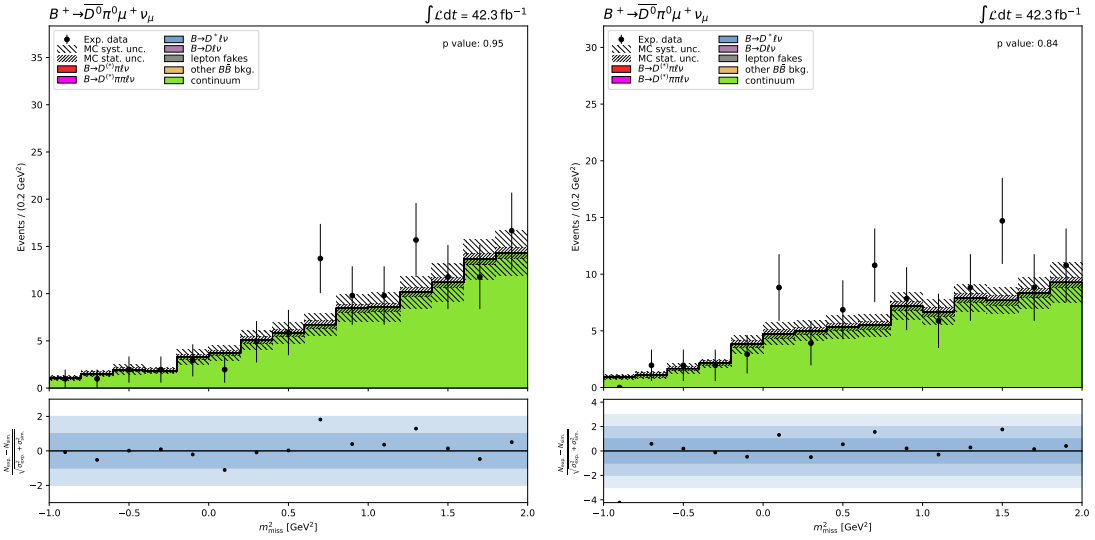

Figure 7.3.: Comparison of the m^2_{miss} for the reconstructed $B \to D^{**}\ell\nu_\ell$ decay mode in the title of the plot in the region with one or more tracks in the ROE on the left-hand side and no tracks in the ROE on the right-hand side.

Within the statistical uncertainties these distributions are compatible with one another and therefore the decision was made not to apply any additional corrections or uncertainties to the continuum MC.

7.2. Investigation of tag-side variables in signal region

Now, that the sideband region as well as the continuum MC have been investigated further and a reasonable agreement between simulation and data has been observed, some tag-side variables in the signal region are investigated. For this, the reconstruction of the B_{Sig} and B_{Tag} meson towards an $\Upsilon(4S)$ resonance has been performed, however, only quantities regarding the B_{Tag} meson are investigated to analyse potential mismodelling between simulation and data.

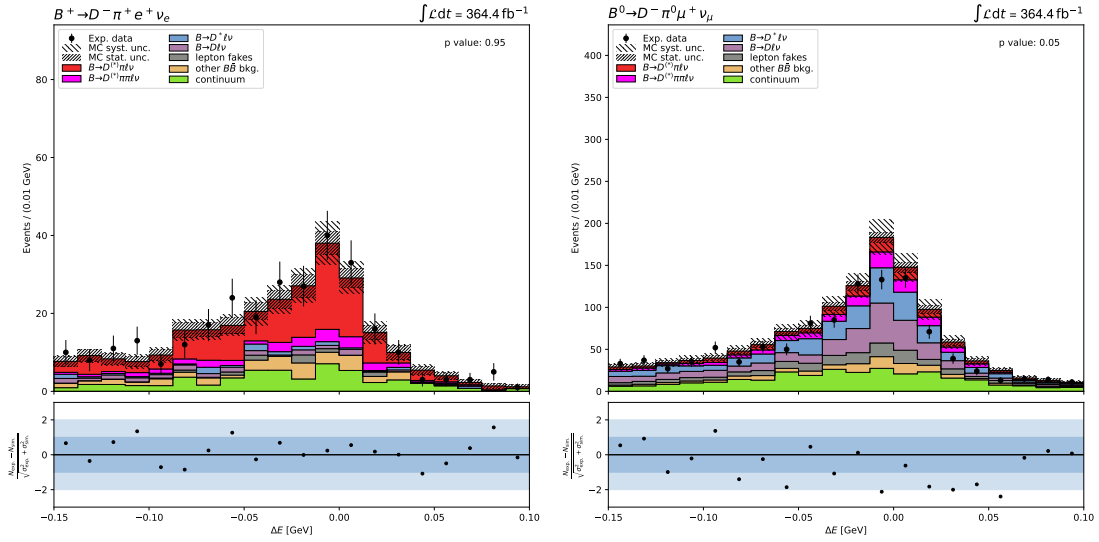

Figure 7.4.: Comparison between simulation and data in the signal region using the ΔE variable of the B_{Tag} meson for the $B \to D^{**} \ell \nu_\ell$ decay channel in the title of the histogram.

Two example distributions for ΔE in fig. 7.4 and for M_{bc} are given in fig. 7.5 (see eq. (6.3) and eq. (6.4) for the definition of the variables). Also in these variables, a reasonable agreement between the recorded and simulated data set can be observed.

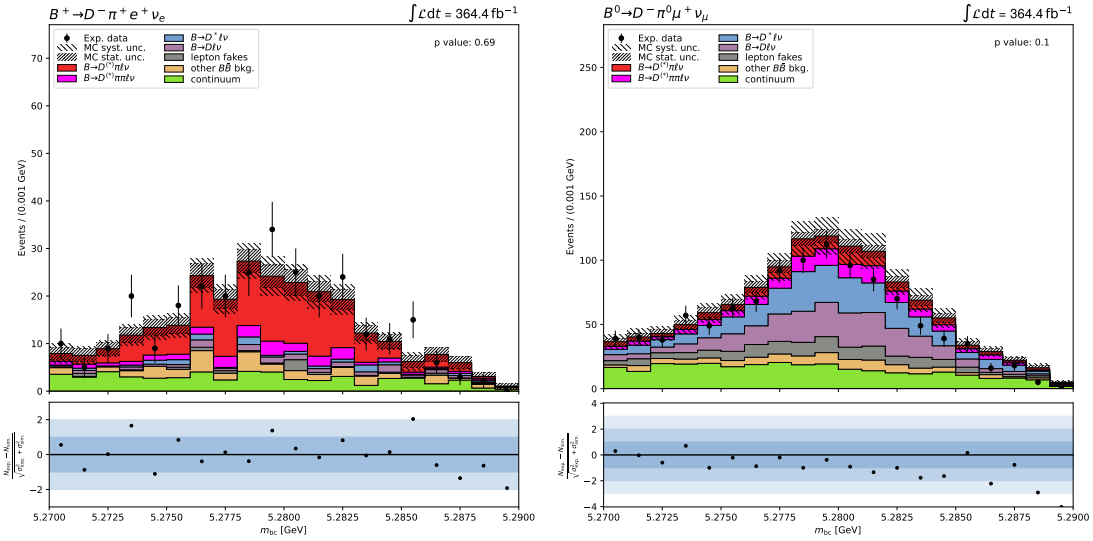

Figure 7.5.: Comparison between simulation and data in the signal region using the beam constraint mass of the B_{Tag} meson for the $B \to D^{**} \ell \nu_\ell$ decay channel in the title of the histogram.

7.3. Investigation of signal-side variables

After also investigating the tag-side in the signal region, also some checks using variables of the signal-side are performed. One such variable is the momentum of the light charged lepton in the CMS, as can be seen in fig. 7.6. For this variable, a good agreement between simulation and data is seen.
Another very important variable that has been investigated is m^2_{miss}, which is considered as the variable to extract the branching ratio for the signal and normalisation mode.
m^2_{miss} can be calculated as follows:

$$m^2_{\mathrm{miss}} = (p_{B_{\mathrm{Sig}}} - p_\ell - p_{D^{*(*)}})^2, \tag{7.3}$$

where $p_{B_{\mathrm{Sig}}}$, p_ℓ and $p_{D^{*(*)}}$ correspond to the four-momentum of the B_{Sig} meson, the charged light lepton and the D^{**} or D^* meson, respectively. Here, it depends which mode is reconstructed either the signal mode D^{**} or the normalisation mode D^* to chose the corresponding meson. As the D^{**} meson is not explicitly reconstructed, the four-momentum of the corresponding $D^{(*)}\pi$ meson pair is added to determine the four-momentum of the potential D^{**} meson candidate.
Besides, the four-momentum of the B_{Sig} meson cannot be measured directly, because there is the undetected neutrino. Rather, it has to be inferred from the tag-side, as the B_{Sig} and the B_{Tag} meson are created back-to-back in the $\Upsilon(4S)$ rest frame. The other required quantities can directly be measured with the detector.
The corresponding distributions can be found in fig. 7.7.
A good agreement between the simulated and experimental data is visible in this variable.

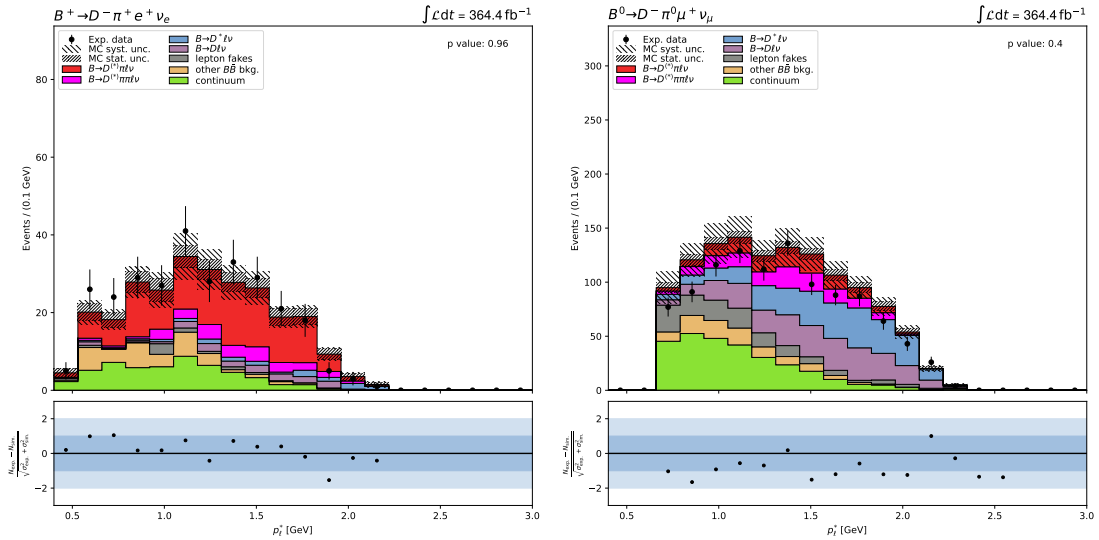

Figure 7.6.: Momentum of the light charged lepton in the CMS in the signal region for the $B \to D^{**} \ell \nu_\ell$ decay in the title.

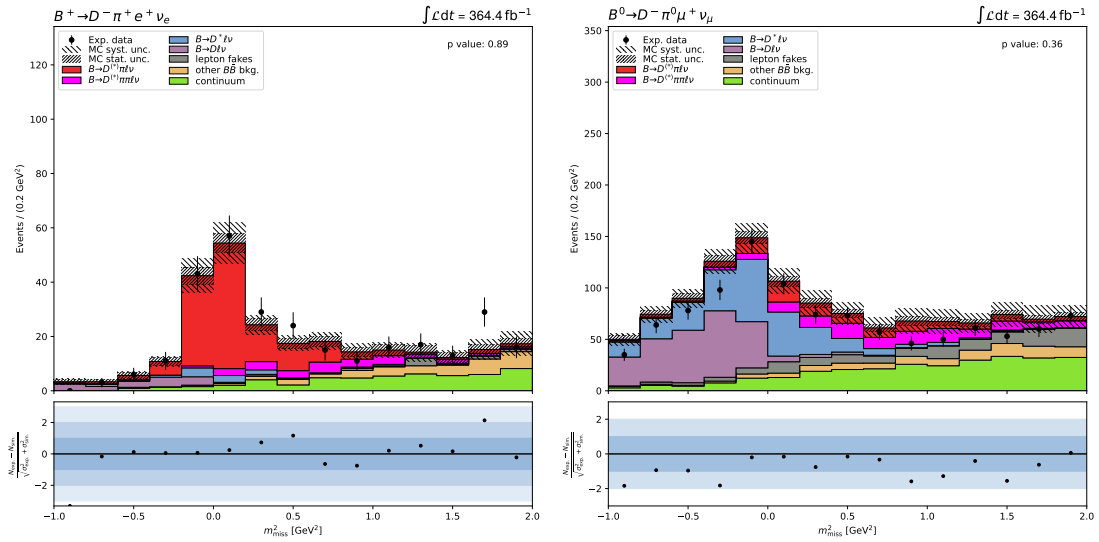

Figure 7.7.: m^2_{miss} in the signal region for the $B \to D^{**} \ell \nu_\ell$ decay in the title.

Also all the other $B \to D^{**}\ell\nu_\ell$ and $B \to D^{*}\ell\nu_\ell$ decay modes have been checked and a good agreement has been observed for all channels, where some example histograms for the $B \to D^{**}\ell\nu_\ell$ can be found in appendix B and in appendix C for the $B \to D^{*}\ell\nu_\ell$ decays.

CHAPTER 8

Branching Ratio Determination and Systematic Uncertainties

8.1. Theory of the fit

To determine the branching ratios of the $B \to D^{**}\ell\nu_\ell$ decays, a binned maximum likelihood fit using the PYHF package [171,172] is performed. It relies on HISTFACTORY [173], where the underlying theory is described in [174].
This chapter, based on [175], will briefly introduce maximum likelihood fits using many parameters that can give e.g. information regarding differences between simulation and data arising from systematic uncertainties.
The main idea is to estimate these numerous parameters using the observed data distributions. Here, the different parameters $\boldsymbol{\theta}$ with the estimators $\hat{\boldsymbol{\theta}}$ need to be determined in one single fitting procedure, where bold parameters correspond to a vector of parameters.
However, to be a single good estimator, it needs to be efficient, unbiased and consistent. This means that the estimator $\hat{\theta}$ converges to the true value θ for a large number of data points N. Besides, it should have a small variance and the expectation value must be equal to the true value θ.
The parameters are estimated as follows: At first, for the given measurement, the data is divided into N statistically independent data points $\{x_i\}$. Every single data point can be described by an (unknown) probability density function $P(x_i|\boldsymbol{\theta})$ (PDF), where $\boldsymbol{\theta}$ are the parameters that need to be determined.
The likelihood function for this unbinned case with the joint probability density for the data set $\boldsymbol{x} = \{x_i\}$ is given by:

$$L(\boldsymbol{x}|\boldsymbol{\theta}) = \prod_{i=1}^{N} P(x_i|\boldsymbol{\theta}). \tag{8.1}$$

If the estimation of parameters $\boldsymbol{\theta}$ equals $\hat{\boldsymbol{\theta}}$, the likelihood function has its global maximum.
However, this approach does not take into account statistical uncertainties on the total number of data points N. This means, if one would perform the measurement again, one would see a Poisson fluctuation from the measured events N around the (unknown) expectation value ν.
This is incorporated into the extended maximum likelihood function. However, usually its logarithm is used due to its monotonous nature as it reduces the product to a sum, which is better for iterative minimisations.
The extended log-likelihood is given by:

$$\ln L(\boldsymbol{x}|\nu, \boldsymbol{\theta}) = \sum_{i=1}^{N} \ln P(x_i|\boldsymbol{\theta}) + N \ln \nu - \nu, \tag{8.2}$$

from which the additive terms that are independent of the parameters $\boldsymbol{\theta}$ are dropped.
To now measure the decay rate, one needs to incorporate the rate as a parameter into the likelihood function and extract its value by determining its optimum for the measured data. Nonetheless, the data is not completely pure, which means that the data must be described by more than one PDF $P(x|\boldsymbol{\theta})$. This is also the case in this analysis, nevertheless, the different $P(x|\boldsymbol{\theta})$ have different distributions for different components. The difference in shapes $P_S(x_i|\boldsymbol{\theta})$ for signal and $P_B(x_i|\boldsymbol{\theta})$ for background processes can be exploited to determine the fraction of signal-like and background-like events in a given data set $\{x_i\}$.
To incorporate this for the fraction of signal-like events, the signal strength parameter μ is included into the model. This is also the parameter of interest in this analysis. It allows to scale the amount of signal events in the simulation up or down. For the case $\mu = 0$, there exists no signal and the background-only hypothesis is considered.
When the scaling parameter μ is set to one, the hypothesis of signal and background is taken from the expectation according to the simulation.
Hence, the total number of events in the measurement is given by $N = \mu S + B$ with S and B being the number of postulated signal and background events respectively. Also, the additional parameters $\boldsymbol{\theta}$ are usually called nuisance parameters (NPs).
By replacing ν with $\mu S + B$ eq. (8.2) yields:

$$\ln L(\boldsymbol{x}|\mu, \boldsymbol{\theta}) = \sum_{i=1}^{N} \ln[\mu S P_S(x_i|\boldsymbol{\theta}) + B P_B(x_i|\boldsymbol{\theta})] - (\mu S + B), \tag{8.3}$$

which is now dependent on the signal strength parameter μ.
For a computationally more efficient calculation, the data is binned if the number of obtained data points N is sufficiently large. This however results in bin-wise probabilities for the PDFs $P_S(x_i|\boldsymbol{\theta})$ and $P_B(x_i|\boldsymbol{\theta})$. Besides, each bin b now has the number N_b of events accumulated into it.
By taking this into account, the likelihood can be written as a product of the Poisson

probabilities to measure N_b events in bin b:

$$L(N|\nu,\boldsymbol{\theta}) = \prod_{b \in \text{ bins}} \text{Poisson}(N_b|\mu\nu_b^S(S,\boldsymbol{\theta}) + \nu_b^B(B,\boldsymbol{\theta})). \tag{8.4}$$

Here, ν_b^S and ν_b^B correspond to the expected number of events in bin b to be signal- or background-like. Regardless, both are dependent on the NPs $\boldsymbol{\theta}$.
In general, there are different ways how to include the NPs into the fit. The three different types account for different kinds of systematic uncertainties.
The first type includes statistical uncertainties that arise due to the limited simulation in each bin. The nuisance parameters γ_{bp} are different for each bin b and uncorrelated, but constrained by the overall amount of events in process p. Due to this bin-wise modification, the number of NPs would increase drastically with more bins. Thus, the statistical uncertainty is evaluated for all processes $\{p_i\}$ together.
The second type of NPs, ϕ_p, can change the overall number of events of the process p. This is usually used when the overall rate is unknown and needs to be determined by the fit. This NP corresponds to the scaling parameter μ of the signal process but for the background template.
The third and last kind of NPs can change the shape as well as the rate of the distribution. It is typically constrained by prior knowledge or auxiliary data. These NPs can be further sub-classed into normalisation-only $\eta_p(\boldsymbol{\theta})$ variations, and shape and normalisation $\sigma_{pb}(\boldsymbol{\theta})$ variations, where $\sigma_{pb}(\boldsymbol{\theta})$ is affected differently for each bin b and process p. These NPs are usually correlated.
The summed number of expected events in bin b for a particular process p with all NPs is then given by: $\nu_{bp}(\gamma_b, \phi_p, \boldsymbol{\theta}) = \gamma_b\phi_p(\boldsymbol{\theta})\eta_p(\boldsymbol{\theta})\sigma_{pb}(\boldsymbol{\theta})$, where $\phi_p(\boldsymbol{\theta})$ is equal to N, the total number of events, and all other NPs are one for the nominal case. All the NPs $\boldsymbol{\theta}$ are allowed to float freely in the fit, but the likelihood needs more information to constrain them. This can e.g. be done by using prior probability density functions to limit the parameter range.
One method to determine the shape and normalisation variation of $\sigma_{pb}(\boldsymbol{\theta})$ is the template method, which uses alternative MC models to derive the systematic uncertainty. This can either be done by using independent sample sets or reweighting of the nominal data set. Here, the priors of the nuisance parameters $\boldsymbol{\theta}$ are constructed so that the alternative models resemble the one-sigma deviation of a Gaussian prior and the central value describes the nominal prediction.
For the normalisation variations $\eta(\boldsymbol{\theta})$ an exponential interpolation is used to create continuous distributions, whereas for the bin-by-bin wise variations $\sigma_b(\boldsymbol{\theta})$ a piece-wise linear interpolation is utilised.

8.2. Fit setup

To determine the branching ratios for the eight different $B \to D^{(*)}\pi\ell\nu_\ell$ combinations, as reconstructed in section 6.4.3, the just described binned maximum likelihood fit is performed. An additional fit based on the same method is conducted to determine the

branching ratio of the normalisation mode $B \to D^* \ell \nu_\ell$.
The signal extraction is done separately for the two light charged leptons, meaning the electron and the muon and the variable chosen to determine the branching ratio is the missing mass squared m^2_{miss} as defined in eq. (7.3). This variable choice is motivated by the fact that the only particle that cannot be measured in the overall $\Upsilon(4S)$ reconstruction is the neutrino in the B_{Sig} meson reconstruction. Therefore, m^2_{miss} corresponds to the mass of the undetected neutrino, which should peak at zero for correctly reconstructed $B \to D^{**} \ell \nu_\ell$ events.
The peak of the distribution at zero for m^2_{miss} shows tails to either side that arise due to the finite detector resolution and misreconstructed candidates. Compared to that, the background categories do not peak around zero, but have a rather broad shape, which makes it possible to separate between the signal and background processes.
Now, a differentiation between the two performed fits has to be made due to different selections, meaning the performed fit for the signal or the normalisation mode.

8.2.1. Signal fit

A schematic of this fit setup can be seen in fig. 8.1.
For the signal mode fit, the m^2_{miss} distribution shows a clear peak at zero for the true D^{**} meson decays with one pion in the D^{**} meson reconstruction. For D^{**} mesons that decay via two pions on truth level, a shift of the peak towards the positive m^2_{miss} regime is expected due to the missed pion in the reconstruction.
For generated $B \to D \ell \nu_\ell$ or $B \to D^* \ell \nu_\ell$ meson decays, the peak is slightly shifted towards negative values of the missing mass because there have been additional particles reconstructed that are not present on generator level such as pions.
The other background categories, as described in section 6.7, meaning lepton fakes, other $B\overline{B}$ background and continuum are distributed more in the positive m^2_{miss} region, covering a rather broad spectrum.
Due to the similar shapes of certain truth categories, they are combined into one fit category. The truth categories lepton fakes, other $B\overline{B}$ background and continuum are combined into the fit category "other background". This is also done for the true $B \to D \ell \nu_\ell$ and $B \to D^* \ell \nu_\ell$ meson decays. Besides, the decays of the nature $B \to D^{(*)} \pi\pi \ell \nu_\ell$ via any resonance for the two pions are included as another template for the fit. It was also investigated to split this category further into decays via an η or via a D^{**} meson, however the fit got unstable due to the reason that the number of events in some bins was small for these modes and rather hard to distinguish from the quite similar signal templates.
The signal category $B \to D^{**} \ell \nu_\ell$ is further sub-divided into the eight different $D^{(*)}\pi$ combinations for the D^{**} meson reconstruction as listed in table 6.4.
To account for the overlap in the reconstruction between the different D^{**} meson decay modes, see e.g. fig. B.4, where most true $B^0 \to D^0 \pi^- \ell^+ \nu_\ell$ events are reconstructed correctly, but some might contribute to $B^0 \to D^{*0} \pi^- \ell^+ \nu_\ell$ because of misreconstruction, one single fit combining all D^{**} decay modes is performed for the electron and another

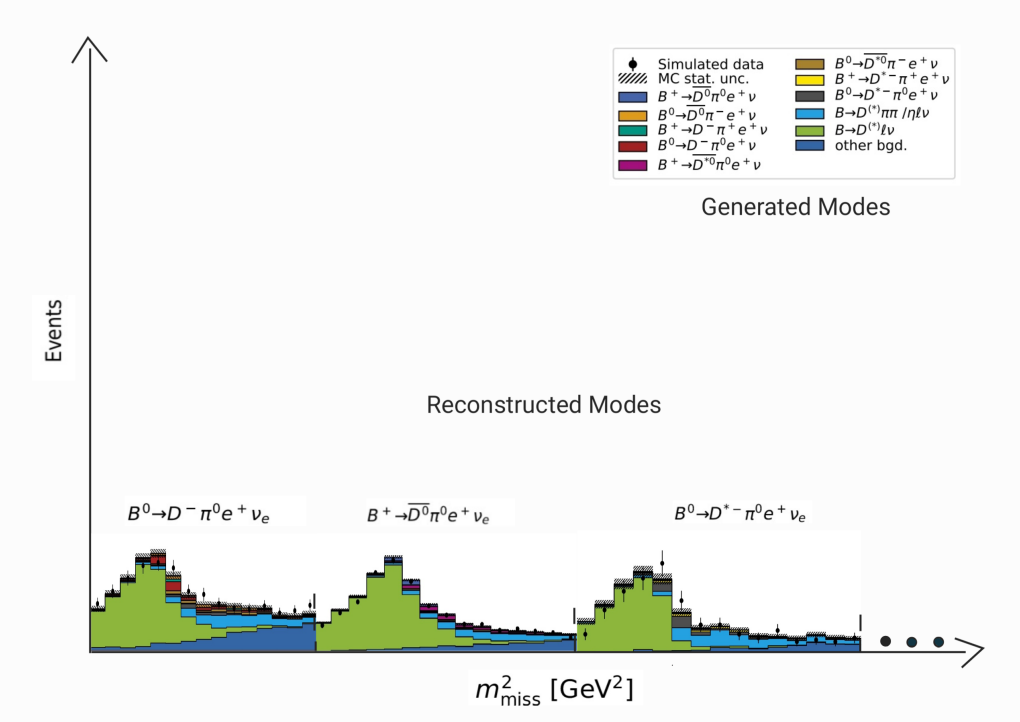

Figure 8.1.: Schematic visualising the fit idea, where the generated decay modes are shown with different colours as can be seen in the box at the top right corner and the different reconstructed decay channels on the x-axis appended to one another. Most generated events show up in their respective reconstructed mode, but some are falsely reconstructed in different modes.

one for the muon mode. This is done by appending the histograms in the range between $-1.0 < m^2_{\text{miss}} < 2.0\,\text{GeV}\,c^{-2}$ for the eight separately reconstructed signal decay channels, so that at the end there exists one histogram with a single x-axis. Here, the product in eq. (8.4) runs over all bins of all eight m^2_{miss} histograms.
During the fit all scaling parameters are left free-floating and are additionally unconstrained. Due to the fact that certain truth categories were combined and others further split, this would yield a total of 11 scaling parameters (eight for signal and three for background). Determining all these scaling parameters including their uncertainties during one fitting procedure is a computationally intensive task. Besides, the uncertainties on the determined scaling parameters on the D^{**} meson modes into $D^{(*)}\pi^0$ combinations would otherwise be dominating (about $\sim 40 - 50\,\%$). These modes suffer from misreconstruction due to neutral pions in the $B \to D^{**}\ell\nu_\ell$ decay. Therefore, the physical property of isospin is considered. This links the scaling parameters for two signal decay channels, which reduces the number of scaling parameters for the eight different signal decays to four scaling parameters.

Isospin combination

The idea of isospin can be attributed back to nuclear physics. The proton and the neutron have very similar masses and the nuclear force is approximately charge independent, therefore Heisenberg [176] suggested that by neglecting the charge, there would be no possibility to distinguish between the proton and the neutron. As a result, the concept of isospin was introduced, where the proton and neutron form an isospin doublet with the charge invariance being expressed as a unitary transformation in the isospin space. This idea can be further extended to the quarks of the first generation, as QCD treats all quark flavours equally.
The isospin I is $1/2$ for u and d quarks, where the third component I_3 is $+1/2$ for the u quark, $-1/2$ for the d quark and zero for all the other quarks. For the anti quarks I_3 is $-1/2$ for the $\bar{u}$ and $1/2$ for the $\bar{d}$ quark.
For a combination of e.g. two quarks, the third component of the isospin can either align between the quarks or point into the opposite direction. This results in different I_3 values for one single value of total isospin I.
The combinations of e.g. a b quark with a u or d quark and $I = 1/2$ form the two isospin doublets for the neutral and charged mesons: B^-, $\overline{B}^0$ and B^+, B^0.
This means that by taking into account the approximate isospin symmetry (only approximate, because the mass of the u and d quarks are slightly different), the properties of the B meson do not change, when exchanging a u quark against a d quark, or vice versa. Thus, the B^+ and the B^0 form an isospin doublet.
Therefore, the decay width $B \to X_c\ell\nu_\ell$ should be equal for the B^0 and the B^+ meson, neglecting spectator effects due to QCD couplings with the other quark. Thus, the

following holds:

$$\frac{\mathcal{B}(B^0 \to X_c^- \ell^+ \nu_\ell)}{\mathcal{B}(B^+ \to X_c^0 \ell^+ \nu_\ell)} \propto \frac{\tau(B^+)}{\tau(B^0)}, \tag{8.5}$$

with $\mathcal{B}$ being the branching ratio and τ being the decay time. This can then be propagated down to the decay tree, meaning that the particle collection X_c can be exchanged by any allowed $c\bar{q}$ combination.
One example for linking two scale factors in the fit together are e.g. the two modes $B^+ \to \overline{D}^0 \pi^0 \ell \nu_\ell$ and $B^0 \to \overline{D}^0 \pi^- \ell \nu_\ell$.

8.2.2. Normalisation fit

This section will focus on the explanation of the normalisation fit performed for the $B \to D^* \ell \nu_\ell$ mode. The fit setup of the normalisation fit is very similar to the one used for the determination of the $B \to D^{**} \ell \nu_\ell$ decays. Due to the fact that the $B \to D^* \ell \nu_\ell$ decay has a much higher branching ratio and is easier to determine, the normalisation fit can also be considered as a validation of the signal fit.
Similar to the signal fit, the signal component, in this case the rate of $B \to D^* \ell \nu_\ell$, is further split into neutral and charged B mesons, resulting in two signal templates. All the other truth categories (see section 6.7 for more information) are combined into one background template called "other background".
The true $B \to D^* \ell \nu_\ell$ meson decays are expected to show a clear peak at zero, whereas the other background components are distributed more broadly in the positive m^2_{miss} regime.
To also incorporate the overlap between the neutral and charged D^* meson reconstruction, both reconstructed D^* decay channel histograms are appended to form one overall histogram using $-1.0 < m^2_{\text{miss}} < 2.0\,\text{GeV}\,c^{-2}$ as it is done in the signal fit for the eight signal modes. This overlap between the neutral and charged mode is however very small compared to the D^{**} meson reconstruction and is expected to not substantially improve the fit output, see fig. 8.6 for the charged D^* and fig. C.1 for the neutral D^* meson.
As in the signal fit, all unconstrained scaling parameters are left free-floating.

8.3. Fit validation

After the fit has been set up, different tests to validate the performance and reliability of the fit have been performed. These can be done on the simulated data set, as detailed in section 8.3.1, before performing additional checks on the actual data fitted in section 8.3.2. At last, some studies on the improvement of the performance of the fit are presented in section 8.3.3.

8.3.1. On simulated data

Before looking at the recorded data set, there are various tests that can be conducted using the simulated data set.

On simulated data the fit can be performed once using the same simulated histograms as data and as fit templates. This setup is called Asimov fit.
Pseudo-data can however be generated using the simulated data set to test the fit performance multiple times. This is done by merging in each bin all fit categories together and taking into account their appropriate ratios to each other. Then the content of each bin is randomly varied, where the original bin content can be thought of an expectation value of a Poisson distribution.
Therefore, one can generate different pseudo-data sets using the initial data set. For this analysis, 1000 pseudo-data sets were generated.
For each pseudo-data set, the fit is performed again and the results for the scaling parameters and the respective uncertainties can be further tested.
One such test is to see, whether the retrieved distribution's mean corresponds to the expectation. For this, each pseudo-data set is fitted separately and the determined results are filled into a histogram. To this histogram, a Gaussian distribution is fitted.
The corresponding distributions for the $B \to D^{**}\ell\nu_\ell$ decay mode using the electron can be seen in fig. 8.2 and for the muon in fig. F.1.

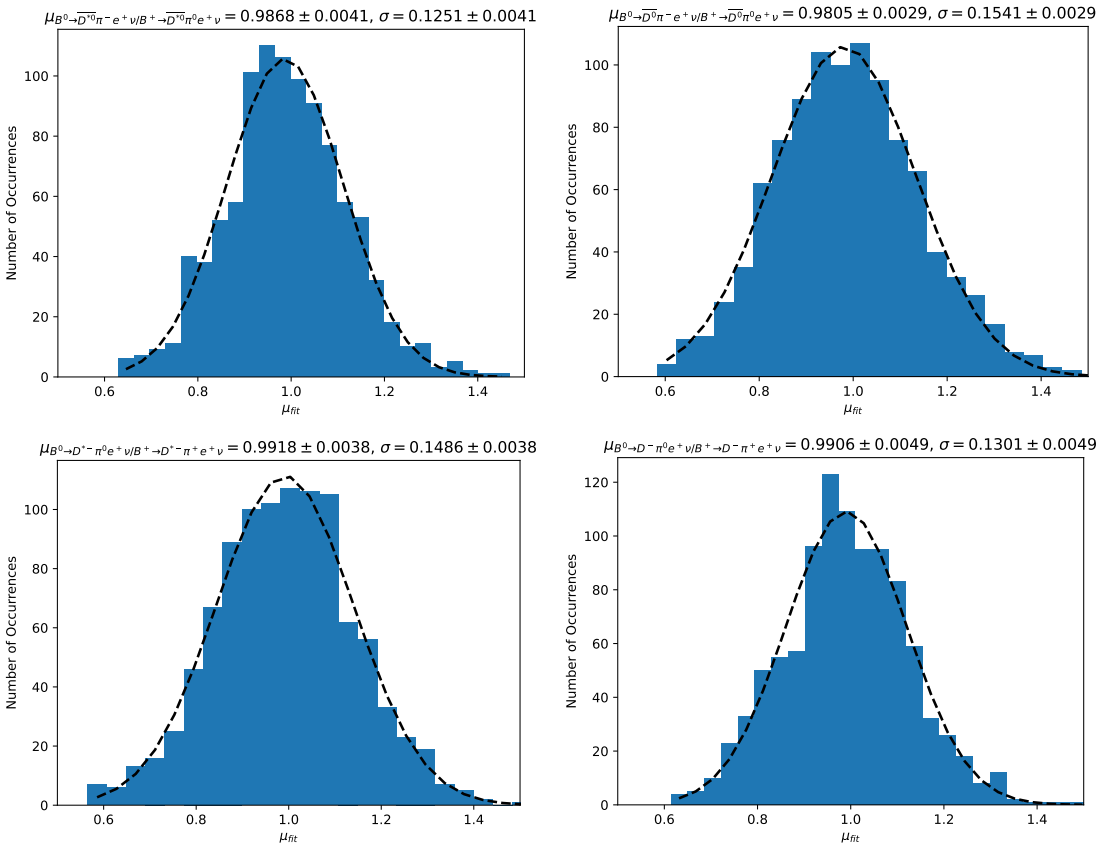

Figure 8.2.: Scaling parameter determined in the fit for each signal category including its uncertainties for the electron modes.

This test is also performed for the normalisation mode, where the results for the electron can be found in fig. G.1 and for the muon in fig. G.2.
As expected, the Gaussian fit to the resulting histogram for each signal template is compatible within uncertainties with a mean of one. The standard deviation σ gives the uncertainty associated to each scaling parameter. This uncertainty gives an estimate of the expected sensitivity of the fit.
Another test is to check the pulls of the different scaling parameters determined by the fit. The pull is defined as the difference between the fitted and the initial value (which is one in this case) of the scaling parameter divided by the uncertainty of the fitted scaling parameter:

$$Pull = \frac{\mu_{\text{Fit}} - \mu_{\text{Initial}}}{\sigma_{\text{Fit}}}. \tag{8.6}$$

If the statistical uncertainty σ_{Fit} is estimated correctly by the fit, a Gaussian distribution with mean $\mu = 0$ and a standard deviation $\sigma = 1$ can be fitted to the pull distribution within uncertainties.
The resulting pull distributions for the $B \to D^{**}\ell\nu_\ell$ decay mode using the electron as the charged light lepton can be seen in fig. 8.3 for all signal templates. The corresponding histograms for the muon can be found in fig. H.1.
This test can also be performed for the normalisation fit. The respective distributions can be found in fig. I.1 for the electron and in fig. I.2 for the muon.
This test showed no bias for either of the two fits or fit templates. In addition to looking only at the signal templates, the pull distributions for the scaling parameter of the background templates can also be investigated. This has been done and no bias has been found.
One last additional test, called linearity check, has been performed. This test checks if the fit is stable when varying the scaling parameter of the signal or background processes in the pseudo-data amount. This can be achieved by scaling certain signal or background processes up or down in the simulation and using this as the new data for the fit that still uses the nominal scaling as starting point. Various different scaling scenarios were tested in the range between 0.5 to 1.5 and the fit could always reproduce the parameter used to scale the corresponding contribution. Therefore, it was concluded that the fit is stable against any up or down scaling of signal or background categories, which is useful in case one contribution in the signal or background templates in the simulation is incorrectly modelled or if the signal branching ratio is not as expected.

8.3.2. On experimental data

After the completion of the tests using simulated data only, an additional test can be performed by running the fit on the experimental data without looking at the result for the signal strength parameters μ, i.e. keeping the result of the analysis still blinded. The pull as defined in eq. (8.6) can be investigated. This time however, the different nuisance parameters, see section 8.1 and section 8.5 for further details, and their determined uncertainties are checked in more detail.

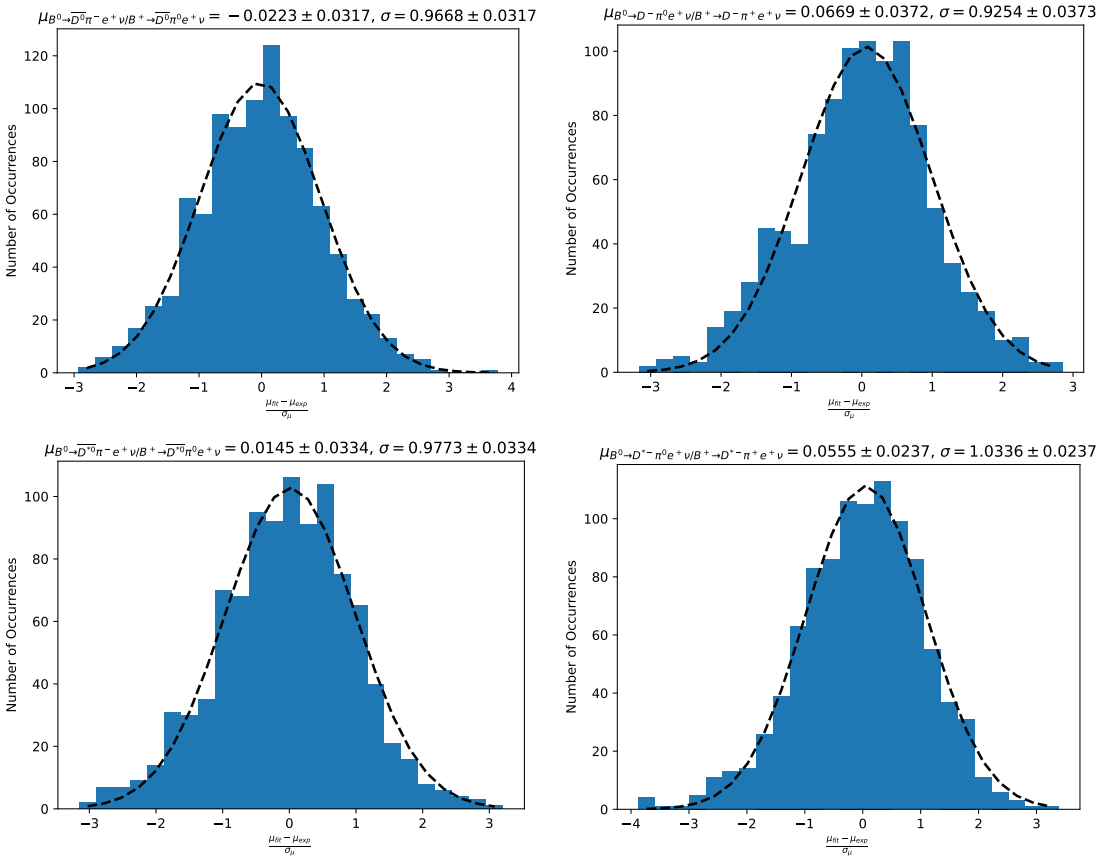

Figure 8.3.: Pull distributions for all signal templates, where the corresponding category can be found at the top left of the plot in the subscript of the μ. The μ corresponds to the width of the distribution for the electron mode.

The results for the $B \to D^{**}\ell\nu_\ell$ decay channel can be found in fig. 8.4. The different considered nuisance parameters can be seen on the y-axis, where "MC_stat_err[x]", corresponds to the statistical uncertainty on the MC simulation in bin x.
The black dots correspond to the determined value for each systematic uncertainty parameter and the black lines to the corresponding uncertainty. The dots should ideally be in the pull range of the x-axis between -1 and 1, meaning in the expected $1\,\sigma$ interval. Besides, the uncertainties should have a width of two.
This is the case for mostly all the considered nuisance parameters, only the nuisance parameters attributed to the GAP simulation show a lot smaller width, which means that the fit is able to constrain these parameters. However, the uncertainty considered in this analysis for the branching ratio associated to the GAP simulation is 100 %, which might be a slight overestimation.
This is also investigated for the normalisation decay channel in fig. J.1.
In general, this test underlines the correctness of the signal and normalisation fit.
The same test for the nuisance parameters has also been done on pseudo- and Asimov data before looking at the outcome on data. No bias or unexpected result for the nuisance parameters has been observed underlining the stability of the fit.

8.3.3. Fit performance studies

To improve the performance of the fit, several studies have been performed, such as changing the bin multiplicity by considering equidistant and non-equidistant binning, as well as other fit categories, or considering another variable.
Another promising variable to determine the branching ratios is u_{miss}, which is defined as $p_{\text{miss}} = p_{B_{\text{Sig}}} - p_\ell - p_{D^{*(*)}}$ and $u_{\text{miss}} = E_{\text{miss}} - |\vec{p}_{\text{miss}}|$.
Changing any of the mentioned parameters did not significantly change the fit result, for some cases the fit became even unstable. Therefore, the decision was reached to keep the nominal fit setup.

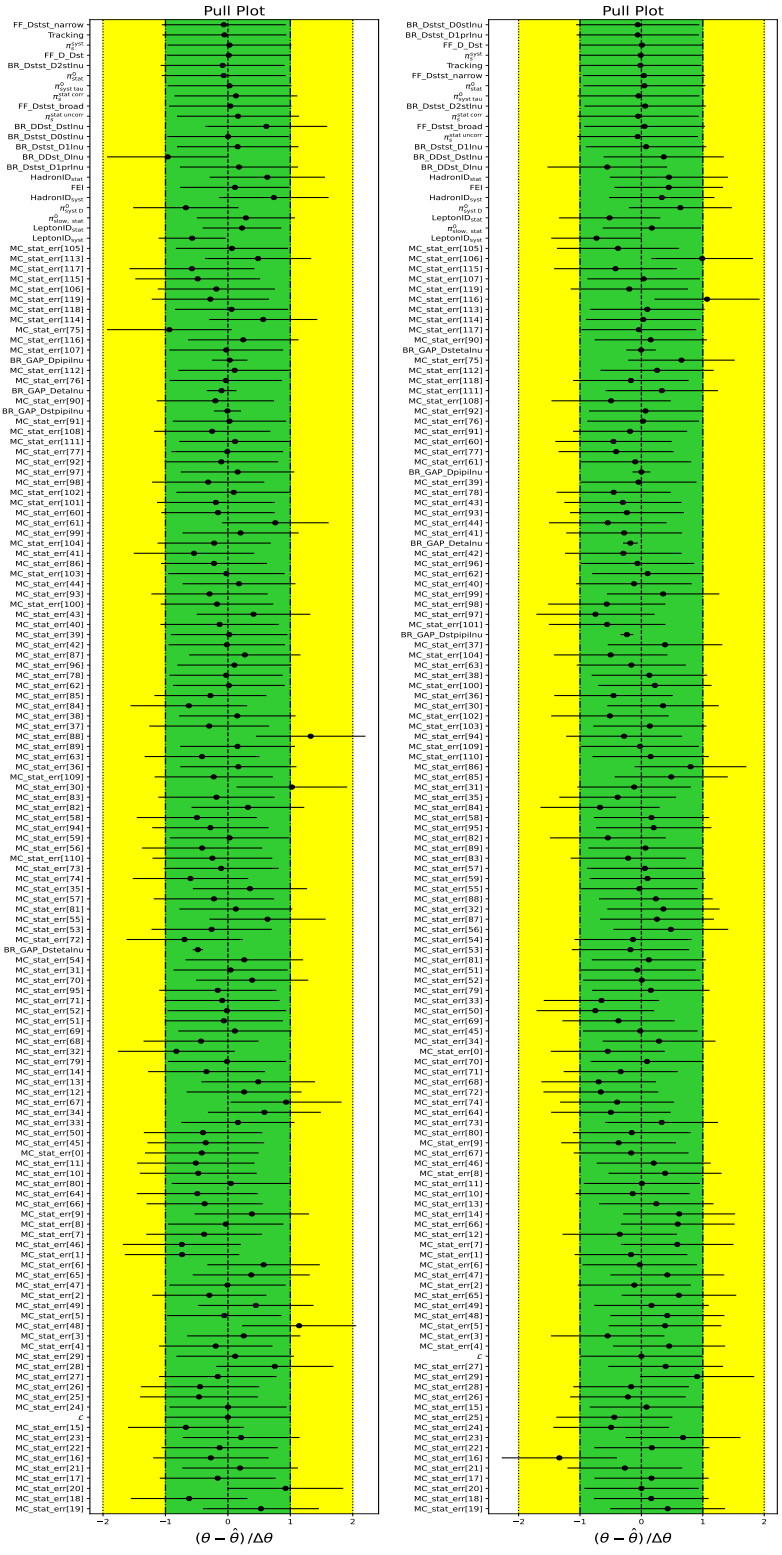

Figure 8.4.: Mean and width of the pull distributions for the fit using the electron mode on the left-hand side and the muon on the right-hand side including all the systematic uncertainties considered as nuisance parameters for the $B \to D^{**}\ell\nu_\ell$ decay mode.

8.4. Fit results

After the validation of the fit, the results when applying the fit on Belle II data will be presented and explained in the following sections.
The first section will start with showing the prefit distributions given to the fitter in section 8.4.1. The branching ratios can be determined using the fitted scaling parameters as will be explained in section 8.4.2. Besides, the postfit distributions will be given in section 8.4.3, followed by the origin of the different systematic uncertainties in section 8.5.1. Afterwards the impact on the result in section 8.5.2 is presented and the determination of the normalised branching ratios in section 8.5.3. At last, the combination of the light charged lepton channels to determine the normalised branching ratio, will be detailed in section 8.5.4.

8.4.1. Prefit distributions

The so called prefit distributions are the histograms that are given to the fitter and can also be used to compare if the simulation agrees with the data.
Extensive studies about the agreement between the simulated and the experimental data have already been performed in chapter 7. The overall agreement is reasonable.
Two example prefit distributions for the $B \to D^{**}\ell\nu_\ell$ decay channel can be found in fig. 8.5, where the rest of the decay modes can be found in appendix B.
In general, it can be said that the $B \to D^{**}\ell\nu_\ell$ decay modes including a π^0 in the D^{**} meson decay have a worse mass resolution than the modes, where a direct daughter of the D^{**} meson is a charged pion.
The prefit distributions for the charged D^* meson for the determination of the branching ratio used as a normalisation, can be found in fig. 8.6. The corresponding histograms for the neutral D^* meson can be seen in appendix C.
Compared to the $B \to D^{**}\ell\nu_\ell$ decay reconstruction the samples are much purer with only a small background contribution.
However, the data is slightly above the prediction but still within the uncertainties of the expectation, indicated by the blue band in the lower part of the histogram.

8.4.2. Branching ratio determination

After the investigation of the fit variable m^2_{miss} for the signal and normalisation mode, the fit is performed and the results are used to determine the measured branching ratio for the corresponding decay mode.
In case the determined branching ratio would deviate from the expected branching ratio, the rate of the observed signal events would be biased, this in return would directly be visible in higher or lower μ scaling parameters of the fit.
To determine the measured branching ratio, the branching ratios used for the generation of the simulated data are required. As mentioned in section 4.2.1, the branching ratios of the $B \to D^{**}\ell\nu_\ell$ and $B \to D^{*}\ell\nu_\ell$ decays are updated to the newest available values, which have to be considered as default values in this analysis.

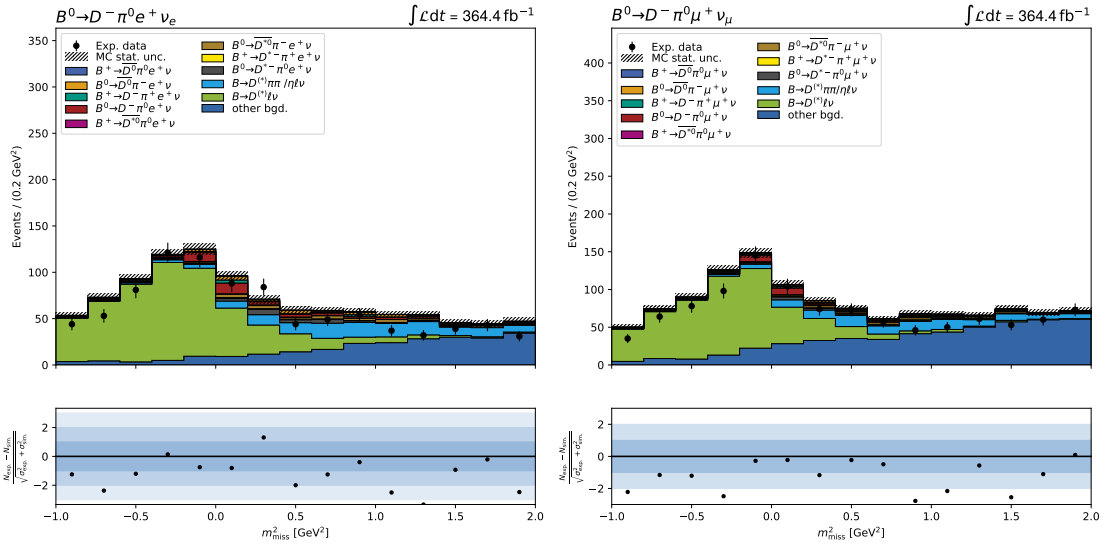

(a) Electron (b) Muon

Figure 8.5.: Prefit distributions showing the agreement between simulation and data for the decay mode indicated in the title, on the left-hand side for the electron and on the right-hand side for the muon.

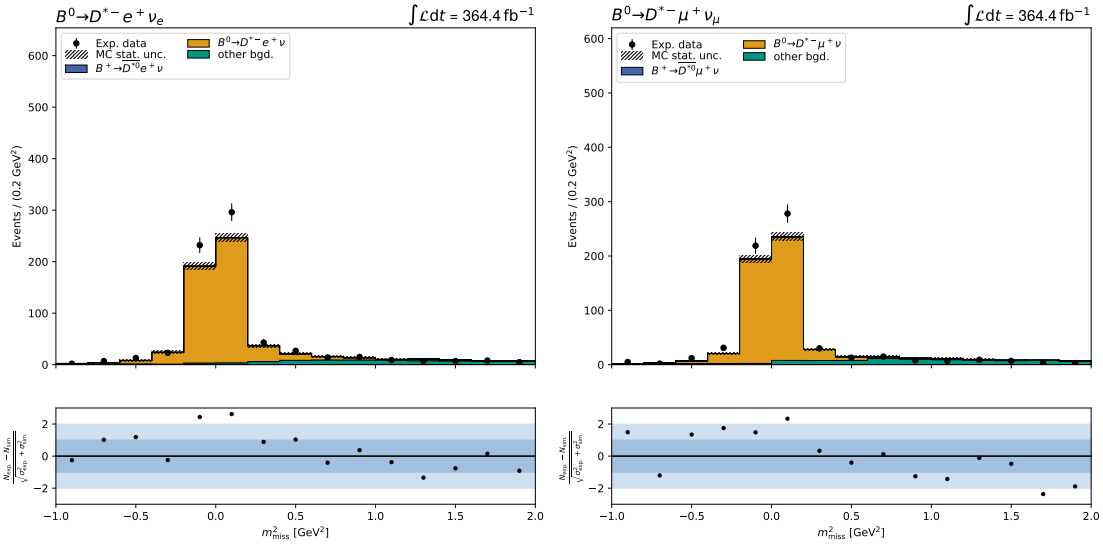

(a) Electron (b) Muon

Figure 8.6.: Prefit distributions showing the agreement between simulation and data for the decay mode indicated in the title, on the left-hand side for the electron and on the right-hand side for the muon.

In table 4.1, the branching ratios considered for the $B \to D^{**}\ell\nu_\ell$ decays can be found, starting from line three to six. Additionally, the sub-decays of the D^{**} mesons are summarised in table 8.1. Due to the fact that this analysis does not explicitly reconstruct

Decay channel			Branching ratio
Neutral			
D_0^{*0}	$\to$	$D^0\pi^0$	33.33 %
D_0^{*0}	$\to$	$D^+\pi^-$	66.67 %
D_1^0	$\to$	$D^{*0}\pi^0$	19.97 %
D_1^0	$\to$	$D^{*+}\pi^-$	39.94 %
$D_1^{\prime 0}$	$\to$	$D^{*+}\pi^-$	66.67 %
$D_1^{\prime 0}$	$\to$	$D^{*0}\pi^0$	33.33 %
D_2^{*0}	$\to$	$D^{*0}\pi^0$	13.34 %
D_2^{*0}	$\to$	$D^{*+}\pi^-$	26.69 %
D_2^{*0}	$\to$	$D^0\pi^0$	19.99 %
D_2^{*0}	$\to$	$D^+\pi^-$	39.98 %
Charged			
D_0^{*+}	$\to$	$D^+\pi^0$	33.33 %
D_0^{*+}	$\to$	$D^0\pi^+$	66.67 %
D_1^+	$\to$	$D^{*+}\pi^0$	19.97 %
D_1^+	$\to$	$D^{*0}\pi^+$	39.94 %
$D_1^{\prime +}$	$\to$	$D^{*+}\pi^0$	33.33 %
$D_1^{\prime +}$	$\to$	$D^{*0}\pi^+$	66.67 %
D_2^{*+}	$\to$	$D^{*+}\pi^0$	13.34 %
D_2^{*+}	$\to$	$D^{*0}\pi^+$	26.69 %
D_2^{*+}	$\to$	$D^+\pi^0$	19.99 %
D_2^{*+}	$\to$	$D^0\pi^-$	39.98 %

Table 8.1.: D^{**} meson branching ratios used in the generation of the Belle II simulated samples considering absolute measurements and isospin relations, see [117].

the D^{**} mesons, but rather uses an inclusive approach, meaning the reconstruction of the decays $B \to D^{(*)}\pi\ell\nu_\ell$, the branching ratios of the B mesons in table 4.1 need to be multiplied by the D^{**} meson sub-decays in table 8.1. To account for all possible combinations of $D^{(*)}$ mesons with neutral and charged π mesons, the determined branching ratios are summed.
The calculated values can be found in table 8.2.

Decay channel	Branching ratio
Neutral	
$B^0 \to \overline{D}^0 \pi^- \ell^+ \nu_\ell$	0.37 %
$B^0 \to D^- \pi^0 \ell^+ \nu_\ell$	0.18 %
$B^0 \to \overline{D}^{*0} \pi^- \ell^+ \nu_\ell$	0.67 %
$B^0 \to D^{*-} \pi^0 \ell^+ \nu_\ell$	0.34 %
Charged	
$B^+ \to \overline{D}^0 \pi^0 \ell^+ \nu_\ell$	0.20 %
$B^+ \to D^- \pi^+ \ell^+ \nu_\ell$	0.40 %
$B^+ \to \overline{D}^{*0} \pi^0 \ell^+ \nu_\ell$	0.31 %
$B^+ \to D^{*-} \pi^+ \ell^+ \nu_\ell$	0.62 %

Table 8.2.: Calculated branching ratios for the different decay modes of the D^{**} meson for the Belle II simulated data, where the ℓ can be either of the charged light leptons.

To determine the branching ratio for the normalisation mode, the reweighted branching ratios in table 4.1 in the second line are considered.
The results of the performed fit are scaling parameters with associated uncertainties for each fit template (the number of scaling parameters for the signal decays in the signal mode are halved due to the considered isospin constraint). Since the fitted scaling parameters are directly proportional to the branching ratios, the measured branching ratios are obtained by multiplying the branching ratios used in the simulation by the fitted values of μ.
The central values extracted in the presented analysis are kept blind to not impede a future publication by the Belle II collaboration. Therefore, only the uncertainties after the fit can be presented.
The results for the relative uncertainties for the normalisation mode $B \to D^* \ell \nu_\ell$ can be seen in table 8.3 for the electron and in table 8.4 for the muon. The relative uncertainty results for the signal fit are displayed in table 8.5 for the electron and in table 8.6 for the muon.
The relative measured $B \to D^* \ell \nu_\ell$ branching ratio uncertainty is around $\sim 10\,\%$, whereas the relative measured branching uncertainty for the $B \to D^{**} \ell \nu_\ell$ decays lies in the range $15-20\,\%$. As expected, the decay modes utilising a neutral pion in the reconstruction of the D^{**} meson have larger uncertainties, this is however improved by considering the isospin constraint between the charged and neutral pions in the D^{**} meson reconstruction.

Decay channel	Branching ratio uncertainty
Neutral	
$B^0 \to D^{*-} e^+$	$\pm 10.4\,\%$
Charged	
$B^+ \to \overline{D}^{*0} e^+$	$\pm 13.2\,\%$

Table 8.3.: Measured relative branching ratio uncertainties for the different decay modes of the D^* meson to a final state containing an electron.

Decay channel	Branching ratio uncertainty
Neutral	
$B^0 \to D^{*-} \mu^+$	$\pm 10.0\,\%$
Charged	
$B^+ \to \overline{D}^{*0} \mu^+$	$\pm 10.5\,\%$

Table 8.4.: Measured relative branching ratio uncertainties for the different decay modes of the D^* meson to a final state containing a muon.

Decay channel	Branching ratio uncertainty
Neutral	
$B^0 \to \overline{D}^0 \pi^- e^+ \nu_e$	$\pm 18.6\,\%$
$B^0 \to D^- \pi^0 e^+ \nu_e$	$\pm 17.1\,\%$
$B^0 \to \overline{D}^{*0} \pi^- e^+ \nu_e$	$\pm 16.4\,\%$
$B^0 \to D^{*-} \pi^0 e^+ \nu_e$	$\pm 19.4\,\%$
Charged	
$B^+ \to \overline{D}^0 \pi^0 e^+ \nu_e$	$\pm 18.6\,\%$
$B^+ \to D^- \pi^+ e^+ \nu_e$	$\pm 17.1\,\%$
$B^+ \to \overline{D}^{*0} \pi^0 e^+ \nu_e$	$\pm 16.4\,\%$
$B^+ \to D^{*-} \pi^+ e^+ \nu_e$	$\pm 19.4\,\%$

Table 8.5.: Measured relative branching ratio uncertainties for the different decay modes of the D^{**} meson to a final state containing an electron. The decay channels with the same branching ratio uncertainty are related using the isospin constraint.

Decay channel	Branching ratio uncertainty
Neutral	
$B^0 \to \overline{D}^0 \pi^- \mu^+ \nu_\mu$	$\pm 21.7\,\%$
$B^0 \to D^- \pi^0 \mu^+ \nu_\mu$	$\pm 16.5\,\%$
$B^0 \to \overline{D}^{*0} \pi^- \mu^+ \nu_\mu$	$\pm 16.2\,\%$
$B^0 \to D^{*-} \pi^0 \mu^+ \nu_\mu$	$\pm 16.6\,\%$
Charged	
$B^+ \to \overline{D}^0 \pi^0 \mu^+ \nu_\mu$	$\pm 21.7\,\%$
$B^+ \to D^- \pi^+ \mu^+ \nu_\mu$	$\pm 16.5\,\%$
$B^+ \to \overline{D}^{*0} \pi^0 \mu^+ \nu_\mu$	$\pm 16.2\,\%$
$B^+ \to D^{*-} \pi^+ \mu^+ \nu_\mu$	$\pm 16.6\,\%$

Table 8.6.: Measured relative branching ratio uncertainties for the different decay modes of the D^{**} meson to a final state containing a muon. The decay channels with the same branching ratio uncertainty are related using the isospin constraint.

8.4.3. Postfit distributions

After the fit has been performed the fit templates can be scaled by the determined scaling parameters to produce the postfit distributions. These can again be investigated to see if the simulation and the fit results agree well with the experimental data. A large visible deviation might hint on an internal problem with the fit like the setup or bad convergence.
The postfit distributions for two decay channels of the signal mode can be seen in fig. 8.7 and for all the other reconstructed decay channels in appendix D. Compared to fig. 8.5, the fitted templates are closer to the data after the fit has been performed.
Two example postfit distributions for the $B \to D^* \ell \nu_\ell$ normalisation mode can be found in fig. 8.8 and for the other channel in appendix E. Also in the normalisation fit (see fig. 8.6 for the prefit distribution), it is visible, that after the fit the fitted templates are closer to the data points.
In general, a good agreement between the simulation and the recorded data can be seen for both the signal and the normalisation mode after performing the fit.

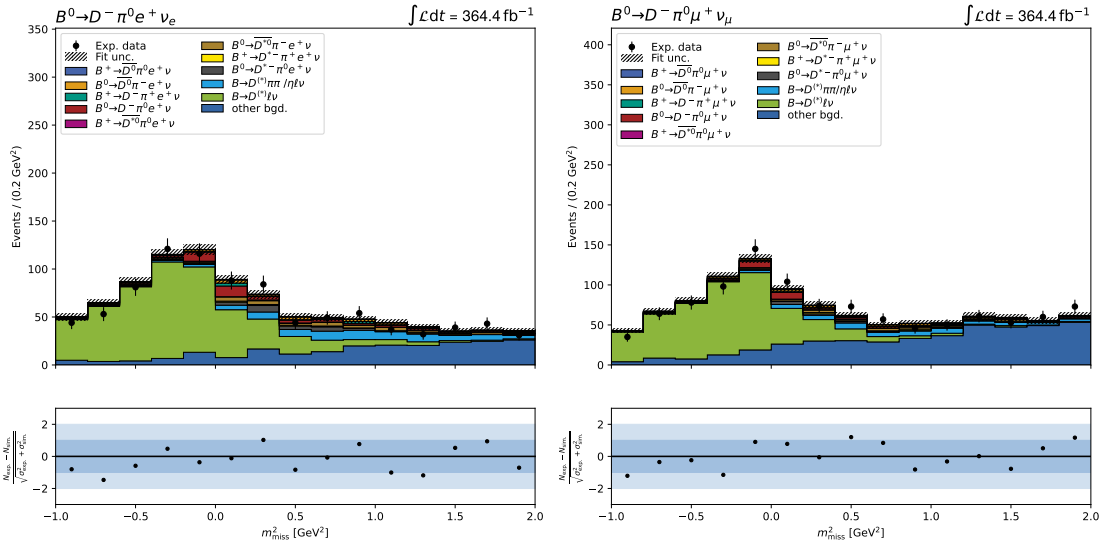

(a) Electron (b) Muon

Figure 8.7.: Postfit distributions showing the agreement between simulation and data for the decay in the title, on the left-hand side for the electron and on the right-hand side for the muon after the fit has been performed.

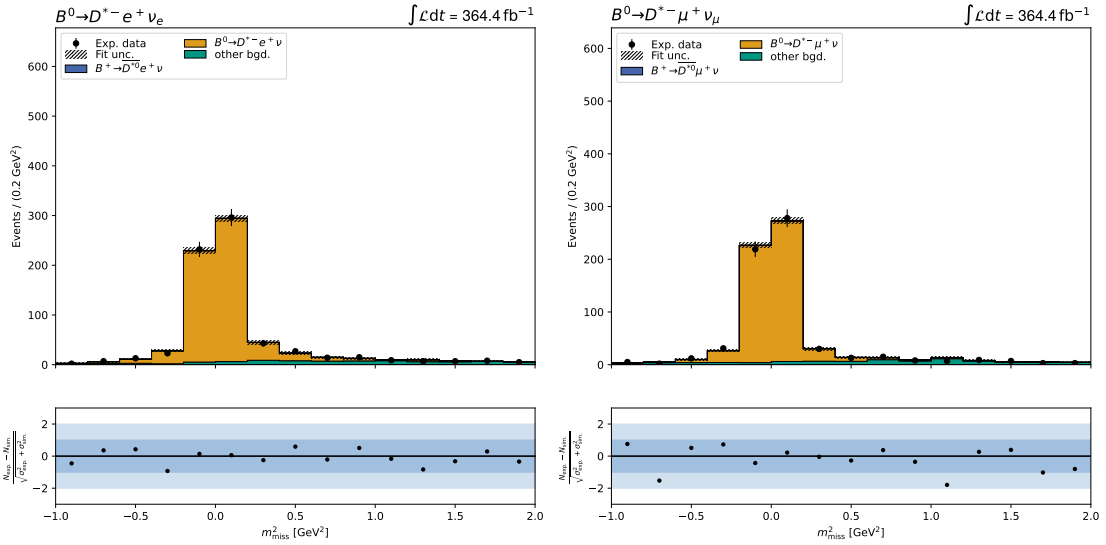

(a) Electron (b) Muon

Figure 8.8.: Postfit distributions showing the agreement between simulation and data for the decay in the title on the left-hand side for the electron and on the right-hand side for the muon after the fit has been performed.

8.5. Systematic uncertainties

In addition to the statistical uncertainties of the measurement originating from the number of observed events, there exist systematic uncertainties to each measurement. These systematic uncertainties can be further sub-classed into modelling and experimental uncertainties.
Uncertainties arising due to the modelling originate from the simulation, such as branching ratios or different considered form factor models.
In contrast, experimental uncertainties arise due to the experimental setup of the Belle II detector, meaning inefficiencies in the reconstruction of particle signatures, restrictions coming from the knowledge of the calibration of certain detector components or the limited understanding of the amount of collected data.
This section focuses on the determination of the impact of all considered systematic uncertainties on the measured branching ratio as well as their incorporation as nuisance parameters into the fit.
As already explained thoroughly in section 8.1, there exist different types of nuisance parameters. One type of nuisance parameter can take different values for every bin, however, uncorrelated and constrained by the overall amount of events. The second type of nuisance parameters is able to change the overall rate of the process, whereas the third and last type is able to change the shape as well as the normalisation of the distribution.
At first the incorporation of the different systematic uncertainties into the fit is described in section 8.5.1, followed by the determination of the impact of each uncertainty to the measured branching ratio in section 8.5.2 including the results.

8.5.1. Origin of systematic uncertainties

This section will be further split into the uncertainties arising from the simulation and the theoretical models and systematic uncertainties originating from experimental effects.

Uncertainties from modelling

For the generation of the simulated samples one needs to rely on theoretical descriptions of e.g. decay properties of certain particles or previous measurements. Due to the fact that there might have been updated measurements or even theories, these can be included into the current simulated samples by e.g. reweighting certain events. However, all these new values come with uncertainties, which results in an ”up” variation of the weight, when the value plus the uncertainty is considered and a ”down” variation by using the weight minus the uncertainty. These can then be considered as alternative weights to fill two additional distributions for the fit. Such uncertainties are of the third type changing shape and rate of the fitted distribution.

Branching ratios As mentioned in section 4.2.1, the generated events are reweighted according to the values given in table 4.1. Each of these values is assigned with an

uncertainty, which originates from the measurements or the isospin relations to already measured decays, expect for the so far unmeasured gap modes $B \to D^{(*)}\eta\ell\nu_\ell$. The uncertainty on the branching ratio here is assumed to be 100 %.
By considering the uncertainties associated to every branching ratio, two alternative templates can be built by varying the original templates up and down within their uncertainty.
So at the end there exists one nuisance parameter for every considered branching ratio uncertainty, each fully correlated between bins.
The uncertainties on the decay modes that are considered as nuisance parameters in this analysis are the processes $B \to D\ell\nu_\ell$, $B \to D^*\ell\nu_\ell$ (not included in the normalisation fit as this is the quantity that is measured), the individual $B \to D^{**}\ell\nu_\ell$ branching ratios for D_0^*, D_1', D_1 and D_2^*, $B \to D^{(*)}\pi\pi\ell\nu_\ell$ and $B \to D^{(*)}\eta\ell\nu_\ell$. These decay channels are the most important ones for this analysis. It has also been investigated to include the uncertainties of the sub-decays of the D^* or D meson. The impact on the final result was however so small, that the decision was made to remove them, to not interfere with the stability of the fit by introducing unnecessary parameters.

Form factors In addition to the newly measured branching ratios, there are updates from the theory for the considered form factors. The reweighting of the simulated samples to the newest theories has been described in section 4.2.1 according to table 4.2. A transformation into an eigenbasis is performed and new weights including uncertainties are determined. Therefore, the form factor uncertainties are translated into shape uncertainties. These uncertainties can again be used to build alternative distributions for nuisance parameters that are able to change the shape and rate of the distributions.
One such nuisance parameter is assigned for every considered new form factor model, which would be the models for the different $B \to D\ell\nu_\ell$, $B \to D^*\ell\nu_\ell$ and $B \to D^{**}\ell\nu_\ell$ decays.

Statistical uncertainty on MC samples To build the different templates for all considered signal and background categories simulated samples are used. The amount of simulated data is however not infinite, only a certain amount has been generated. Therefore, the systematic uncertainty arising from the limited number of statistics in the simulation can be included as nuisance parameters into the fit. For each bin there exists one nuisance parameter. These NPs are uncorrelated between the bins, but constrained by the overall size of the generated MC sample.

Uncertainties from experimental effects

As a final step in the generation of the simulated samples, the interaction of the detector material with the generated particles is performed. This behaviour is however not always simulated perfectly, therefore differences in the detection efficiency might occur compared to data. To work out the impact of these difference, several studies are performed by

comparing the simulation with the recorded data and correction factors are determined that need to be applied to the simulated data and in rare cases to the experimental data. These correction factors nonetheless come with uncertainties.
How these corrections have been calculated for each particle type is explained in further detail in section 6.9.

Track momentum scaling To account for errors in the Belle II magnetic field map, a global track momentum scaling correction is applied to the recorded data, as detailed in section 6.9.1. The systematic uncertainty originating from this correction is not further investigated as the alternative correction factors and their uncertainties are in the order of $\mathcal{O}(10^{-4})$ and thus can be neglected as this measurement is statistically limited.

Particle identification The particle identification can be further sub-divided into the lepton and hadron identification, where the determination of the correction factor including its statistical and systematic uncertainties is described in further detail in section 6.9.3.
For each of the different particles and uncertainty types, one nuisance parameter is assigned. This gives in total four nuisance parameters for the particle identification.

Slow charged pion correction In the D^* meson decay into a slow charged pion, the efficiency to detect such tracks needs to be corrected for observed differences between simulation and data, as stated in section 6.9.4.
For each of the determined uncertainties, meaning the correlated and uncorrelated statistical uncertainty as well as the systematic uncertainty on the method considered, one nuisance parameter is assigned. This results in another three parameters for the slow charged pion.

Neutral pion efficiency corrections The procedure to determine the corrections for the simulated samples that include neutral pions in the reconstruction is described in section 6.9.5, where a distinction between a slow neutral pion (e.g. daughter of a D^* meson with low momentum) and a nominal neutral pion is made.
For each of the two kinds of neutral pions a statistical and two systematic uncertainties are provided for the correction, meaning that three additional nuisance parameters are added for each neutral pion type.

Tagging efficiency correction To account for the observed difference seen between the recorded and the simulated data set, correction factors for the FEI, as detailed in section 6.9.6, are determined. To consider the uncertainty on the correction factor for the tagging in the fit, one additional nuisance parameter is introduced.

Tracking efficiency To determine a systematic uncertainty due to the efficiency of the tracking algorithm, τ pair events are used [177]. One of these tau leptons is supposed to decay leptonically $\tau \to \ell^{\pm}\nu_{\ell}\bar{\nu}_{\tau}$, where the ℓ can either be an electron or a muon. The other tau is hadronically reconstructed into three charged pions $\tau \to 3\pi^{\pm}\nu_{\tau}$.

A tag and probe method is used. For this, three tracks are combined to yield at the end a total charge of ± 1, where the existence of the additional track, the probe track, can be determined by considering charge conservation. This allows to measure the track finding efficiency by looking if the probe track was reconstructed or not. Therefore, the tracking efficiency $\varepsilon_{\text{track}}$ can be calculated as:

$$\varepsilon_{\text{track}} \cdot A = \frac{N_4}{N_3 + N_4}, \tag{8.7}$$

where N_3 is the total number of events, where only three tracks were found, meaning the probe track was not found, and N_4, where four tracks were successfully reconstructed. The factor A takes into account the acceptance of the Belle II detector for the probe track.
The tracking efficiency determined using this study is 0.24 % for each mid- or high-momentum track. To calculate the overall tracking efficiency for an event the number of tracks considered in the reconstruction of the B_{Sig} meson is considered, as this might differ for the reconstructed B meson decay channels. In case of a D^* meson decay into a slow charged pion, the track of the π_{slow} is excluded from the calculation, as this is covered by the slow charged pion corrections as mentioned above.
This results in a unique number of tracks for each event, where alternative weights are determined by subtracting or adding the tracking efficiency to the power of the number of determined tracks for the event from the original weight.
This results in one additional nuisance parameter.

Luminosity The simulated samples are scaled to the luminosity of the recorded data set. To determine the luminosity of the experimental data, a measurement using Bhabha and di-gamma events, for more information please refer to [178], is performed that itself comes with an associated uncertainty.
To take this uncertainty on the luminosity determination into account an additional nuisance parameter is included.

In total this results in 151 different NPs (one NP for every bin for the statistical uncertainty of the simulation) for the $B \to D^{**}\ell\nu_\ell$ fit and 150 NPs for the normalisation fit, as the branching ratio of the decay $B \to D^*\ell\nu_\ell$ is measured there. The introduction of an additional NP to account for the uncertainty on the $B \to D^*\ell\nu_\ell$ decay in the normalisation fit would be double counting as the NP and the scaling parameter do the same.

8.5.2. Impact of systematic uncertainties on the result

As mentioned above, in section 8.5.1, from almost all corrections applied to the simulated or experimental data, an associated systematic uncertainty can be built. Here, the general idea is the same for all systematic uncertainties. Each correction comes with an uncertainty either due to the amount of data considered for this study or the method

for the determination itself. Therefore, in addition to the nominal histogram, which is determined by multiplying the event with the corresponding correction weight, two alternative histograms can be determined. One of these histograms accounts for the uncertainty in the up direction and the other in the lower direction.
Two example distributions for two different systematic uncertainties can be seen in fig. 8.9.

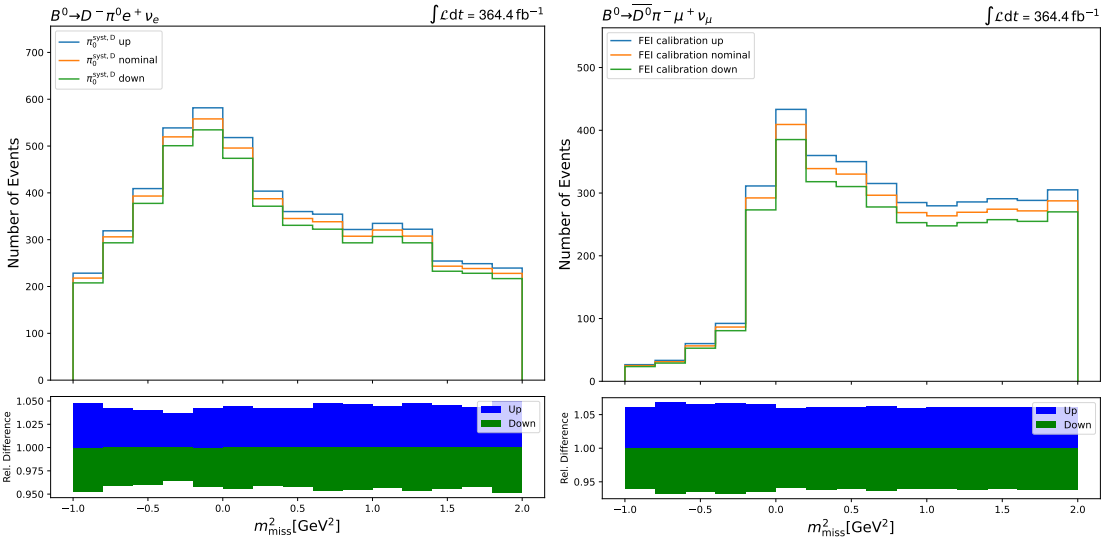

Figure 8.9.: m^2_{miss} distributions showing the nominal, up and down variation for two different systematic uncertainties for the modes shown in the title.

These histograms can be made for each reconstructed B meson decay mode as well as the considered systematic uncertainty. However, in some cases the deviation between the alternative histograms from the nominal histogram is negligible, whereas for others a clear difference is visible.
These histograms are all passed as input to the fit and considered in the fitting procedure. The interpolation between these histograms is done with the parameters σ_{pb} as described in section 8.1.
The general approach to determine the contribution originating from each systematic uncertainty on the signal and the normalisation fit utilises the "Profiling" method. The idea is to run the fit using only the scaling parameters for the different signal and background fit categories on the recorded data set. The uncertainty calculated this way is the statistical uncertainty of the fit.
To determine the impact of one particular systematic uncertainty on the individual scaling parameters, the nuisance parameters associated to this systematic uncertainty are included in addition to the scaling parameters just described. Then a scan around the minimum determined by the fit is performed for each scaling parameter of interest. This means that one scaling parameter is fixed to a certain value, which is usually in the two sigma interval around the minimum, while all the other scaling parameters are left

free floating in the fit. During this scan usually 10 different fixed values for the scaling parameter are considered.
The negative log-likelihood multiplied by two is determined for each of the scanned values, as the intersection with one corresponds to the one-sigma confidence interval and therefore the uncertainty originating from this systematic source including the statistical uncertainty of the fit. The difference between the intersection points is divided by two, as it might be the case, that there exist asymmetric uncertainties at the end.
To determine the statistical uncertainty of the fit, as mentioned above, the same scan is repeated including just the scaling parameters and the intersection points are determined again. Then the square root is taken from the determined squared value including the investigated systematic uncertainty subtracted by the squared value using only the scaling parameters, meaning the statistical uncertainty fit only. By including the different systematic uncertainties, the width of the distribution broadens and this change in width can be used to determine the impact of a systematic uncertainty.
Two example scans can be seen in fig. 8.10.

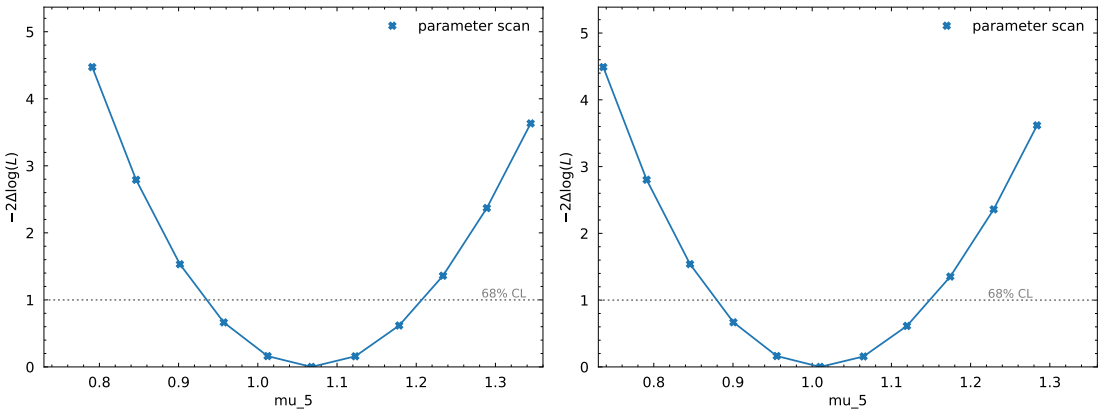

Figure 8.10.: Example for a scan of one scaling parameter, where the scaling parameter is fixed and all the other nuisance parameters are left free floating and for each fixed value $-2\ln\mathcal{L}$ is determined. The histogram on the left-hand side shows the scan with only the scaling parameters included in the fit and the plot on the right-hand side shows the scan, when one additional systematic uncertainty is considered in the fit. It can be seen that the width of the distribution changes by including an additional systematic uncertainty.

These scans have been performed for each signal scaling parameter and systematic uncertainty in the signal and normalisation fit. For simplicity, only the two examples are shown.
The results for these scans have been summarised in tables for the different signal categories in the $B \to D^{**}\ell\nu_\ell$ and the $B \to D^{*}\ell\nu_\ell$ fit. The results for the signal fit using the electron as the light charged lepton can be found in table 8.7 and using the muon in table 8.8.

Source	$B^0 \to D^- \pi^0 e^+ \nu_e /$ $B^+ \to D^- \pi^+ e^+ \nu_e$	$B^0 \to D^{*-} \pi^0 e^+ \nu_e /$ $B^+ \to D^{*-} \pi^+ e^+ \nu_e$	$B^0 \to \overline{D}^0 \pi^- e^+ \nu_e /$ $B^+ \to \overline{D}^0 \pi^0 e^+ \nu_e$	$B^0 \to \overline{D}^{*0} \pi^- e^+ \nu_e /$ $B^+ \to \overline{D}^{*0} \pi^0 e^+ \nu_e$
Statistical	13.6	16.1	15.1	12.6
Systematic uncertainties				
Tagging efficiency	4.4	6.2	3.6	5.7
$\mathcal{B}(B \to D^{(*)}/\eta\pi\pi\ell\nu_\ell)$	<0.1	<0.1	<0.1	2.7
$\mathcal{B}(B \to D^{**}\ell\nu_\ell)$	0.2	1.7	0.5	1.6
$\mathcal{B}(B \to D^{(*)}\ell\nu_\ell)$	0.9	<0.1	<0.1	<0.1
FF(Broad D^{**})	6.2	<0.1	4.6	0.2
FF(Narrow D^{**})	1.5	0.9	1.5	0.8
FF($D^{(*)}$)	<0.1	<0.1	<0.1	<0.1
Tracking efficiency	1.0	1.1	0.7	0.9
$\pi^{\pm}_{\text{slow}}$	0.6	2.5	0.3	0.2
HadronID	0.9	<0.1	<0.1	<0.1
LeptonID	1.0	0.6	1.5	2.9
Luminosity	3.1	4.0	2.5	3.7
π^0	1.8	2.6	3.3	3.6
π^0_{slow}	0.7	<0.1	1.5	1.3
MC statistics	4.0	1.6	4.4	3.7

Table 8.7.: All considered systematic uncertainties as well as the statistical uncertainty for the signal categories in the signal fit using the electron as the light charged lepton in percent. Due to the isospin constraint considered in this analysis, the uncertainties for the isospin partners are always the same.

Source	$B^0 \to D^- \pi^0 \mu^+ \nu_\mu /$ $B^+ \to D^- \pi^+ \mu^+ \nu_\mu$	$B^0 \to D^{*-} \pi^0 \mu^+ \nu_\mu /$ $B^+ \to D^{*-} \pi^+ \mu^+ \nu_\mu$	$B^0 \to \overline{D}^0 \pi^- \mu^+ \nu_\mu /$ $B^+ \to \overline{D}^0 \pi^0 \mu^+ \nu_\mu$	$B^0 \to \overline{D}^{*0} \pi^- \mu^+ \nu_\mu /$ $B^+ \to \overline{D}^{*0} \pi^0 \mu^+ \nu_\mu$
Statistical	13.5	14.7	17.8	14.2
Systematic uncertainties				
Tagging efficiency	1.1	2.6	2.5	2.4
$\mathcal{B}(B \to D^{(*)}/\eta\pi\pi\ell\nu_\ell)$	<0.1	<0.1	<0.1	1.7
$\mathcal{B}(B \to D^{**}\ell\nu_\ell)$	0.5	0.5	0.5	1.3
$\mathcal{B}(B \to D^{(*)}\ell\nu_\ell)$	0.6	<0.1	<0.1	<0.1
FF(Broad D^{**})	5.3	<0.2	7.0	0.3
FF(Narrow D^{**})	0.9	0.5	1.0	0.3
FF($D^{(*)}$)	<0.1	<0.1	<0.1	<0.1
Tracking efficiency	0.8	0.8	0.9	0.7
$\pi^\pm_{\text{slow}}$	0.3	2.1	<0.1	0.2
HadronID	<0.1	<0.1	<0.1	<0.1
LeptonID	2.3	1.6	2.9	1.3
Luminosity	2.5	2.7	3.1	2.9
π^0	1.7	0.6	<0.1	<0.1
π^0_{slow}	0.7	<0.1	1.6	1.6
MC statistics	3.4	3.6	5.1	3.6

Table 8.8.: All considered systematic uncertainties as well as the statistical uncertainty for the signal categories in the signal fit using the muon as the light charged lepton in percent. Due to the isospin constraint considered in this analysis, the uncertainties for the isospin partners are always the same.

It can be seen that the measurement of the $B \to D^{**}\ell\nu_\ell$ decays is statistically limited. The tagging efficiency associated to the hadronic FEI, the FFs for the broad D^{**} mesons, the luminosity, the π^0 detection efficiency and the limited amount of simulated events available, are the main sources of systematic uncertainty. This however is dependent on the reconstructed $B \to D^{**}\ell\nu_\ell$ decay mode.
The split of the systematic uncertainties into their components for the normalisation mode can be seen in table L.1 for the electron and in table L.2 for the muon channel.
This measurement is systematically limited, where the biggest contributions originate from the tagging of the FEI again, the π^0, the $\pi^{\pm}_{\text{slow}}$detection efficiency and the luminosity. Also here, the main systematic uncertainties are dependent on the $B \to D^*\ell\nu_\ell$ reconstruction mode.
Some of the systematic uncertainties are dominant in the signal and the normalisation fit, therefore, by considering the ratio of these two, some of them will cancel out such as the tagging systematic due to the hadronic FEI, but especially the luminosity.
For the final normalised and combined result the systematic uncertainties are not further split into their components due to the fact that the statistical uncertainties are much larger and most of the contributions in the tables of systematic uncertainties will be negligibly small.

8.5.3. Normalised branching ratios

The decision to normalise the $B \to D^{**}\ell\nu_\ell$ decay branching ratios with the $B \to D^*\ell\nu_\ell$ branching ratio was made, as there are systematic uncertainties that contribute to the determination of both branching ratios and will thus cancel out. An example would be the luminosity. Therefore, the uncertainty on the normalised branching ratio is expected to be reduced.
The obtained results for the relative uncertainties on the normalised branching ratios can be seen in eq. (8.11) for the electron and in eq. (8.12) for the muon, where the first value shows the statistical and the second the systematic uncertainty.
For the normalisation, every $B \to D^{**}\ell\nu_\ell$ decay mode is normalised by its associated D^* meson decay mode, depending on the charge of the $D^{(*)}\pi$ combination and the lepton.
To determine the statistical uncertainty on the associated normalised branching ratio, Gaussian error propagation is used, as these uncertainties are uncorrelated:

$$\frac{\sigma_x}{x} = \sqrt{\left(\frac{\sigma_A}{A}\right)^2 + \left(\frac{\sigma_B}{B}\right)^2}, \tag{8.8}$$

where $x = \frac{A}{B}$, with x being the normalised branching ratio, A being the branching ratio of the decay $B \to D^{**}\ell\nu_\ell$ and B the $B \to D^*\ell\nu_\ell$ decay rate.
The statistical uncertainties are uncorrelated, which is achieved by the considered best candidate selection, as explained in section 6.6, and inverting a cut on the D and π combinations for the $B \to D^*\ell\nu_\ell$ decays compared to the signal reconstruction, as mentioned in section 6.4.3.
For the determination of the systematic uncertainties on the normalised branching ratio,

a correlation of 100 % is assumed. The measured signal branching ratio $B \to D^{**}\ell\nu_\ell$ is given by $A \pm \sigma^A_{\text{syst}}$ and the normalisation mode $B \to D^*\ell\nu_\ell$ by $B \pm \sigma^B_{\text{syst}}$.
Since the uncertainties on A and B are assumed to be 100 % correlated, the systematic uncertainty on the result x is evaluated by shifting the results for A and B simultaneously into the same direction according to their individual uncertainty.
The resulting upper systematic uncertainty on the normalised branching ratio is thus given by:

$$\sigma^{x,+}_{\text{syst}} = \left| x - \frac{A + \sigma^A_{\text{syst}}}{B + \sigma^B_{\text{syst}}} \right| . \tag{8.9}$$

And the lower uncertainty can be calculated using the following formula:

$$\sigma^{x,-}_{\text{syst}} = \left| x - \frac{A - \sigma^A_{\text{syst}}}{B - \sigma^B_{\text{syst}}} \right| . \tag{8.10}$$

The outcome might yield asymmetric uncertainties. However, due to the fact that the systematic uncertainties are not the limiting factor in this analysis, the biggest determined systematic uncertainty is considered at the end as symmetric uncertainty.
In addition to this approach it was also investigated to assume full anti-correlation, which means that a systematic uncertainty in the normalisation would go into the opposite direction in the signal mode. This would yield the highest possible systematic uncertainty, but it overestimates the uncertainty completely since there is usually no reason for an uncertainty to have a completely different effect in both modes.

$$
\begin{aligned}
\sigma\left(\frac{\mathcal{B}(B^0 \to \overline{D}^0 \pi^- e^+ \nu_e)}{\mathcal{B}(B^0 \to D^{*-} e^+ \nu_e)}\right) &= (\pm 18.9 \pm 6.1)\,\% \\
\sigma\left(\frac{\mathcal{B}(B^+ \to D^- \pi^+ e^+ \nu_e)}{\mathcal{B}(B^+ \to \overline{D}^{*0} e^+ \nu_e)}\right) &= (\pm 14.2 \pm 0.1)\,\% \\
\sigma\left(\frac{\mathcal{B}(B^0 \to \overline{D}^{*0} \pi^- e^+ \nu_e)}{\mathcal{B}(B^0 \to D^{*-} e^+ \nu_e)}\right) &= (\pm 11.6 \pm 1.4)\,\% \\
\sigma\left(\frac{\mathcal{B}(B^+ \to D^{*-} \pi^+ e^+ \nu_e)}{\mathcal{B}(B^+ \to \overline{D}^{*0} e^+ \nu_e)}\right) &= (\pm 1.68 \pm 0.26)\,\% \\
\sigma\left(\frac{\mathcal{B}(B^0 \to D^- \pi^0 e^+ \nu_e)}{\mathcal{B}(B^0 \to D^{*-} e^+ \nu_e)}\right) &= (\pm 14.1 \pm 1.6)\,\% \\
\sigma\left(\frac{\mathcal{B}(B^+ \to \overline{D}^0 \pi^0 e^+ \nu_e)}{\mathcal{B}(B^+ \to \overline{D}^{*0} e^+ \nu_e)}\right) &= (\pm 18.7 \pm 3.1)\,\% \\
\sigma\left(\frac{\mathcal{B}(B^0 \to D^{*-} \pi^0 e^+ \nu_e)}{\mathcal{B}(B^0 \to D^{*-} e^+ \nu_e)}\right) &= (\pm 14.3 \pm 1.5)\,\% \\
\sigma\left(\frac{\mathcal{B}(B^+ \to \overline{D}^{*0} \pi^0 e^+ \nu_e)}{\mathcal{B}(B^+ \to \overline{D}^{*0} e^+ \nu_e)}\right) &= (\pm 11.3 \pm 1.7)\,\%
\end{aligned}
\tag{8.11}
$$

$$
\begin{aligned}
\sigma\left(\frac{\mathcal{B}(B^0 \to \overline{D}^0 \pi^- \mu^+ \nu_\mu)}{\mathcal{B}(B^0 \to D^{*-} \mu^+ \nu_\mu)}\right) &= (\pm 17.2 \pm 4.5)\,\% \\
\sigma\left(\frac{\mathcal{B}(B^+ \to D^- \pi^+ \mu^+ \nu_\mu)}{\mathcal{B}(B^+ \to \overline{D}^{*0} \mu^+ \nu_\mu)}\right) &= (\pm 16.2 \pm 2.9)\,\% \\
\sigma\left(\frac{\mathcal{B}(B^0 \to \overline{D}^{*0} \pi^- \mu^+ \nu_\mu)}{\mathcal{B}(B^0 \to D^{*-} \mu^+ \nu_\mu)}\right) &= (\pm 15.2 \pm 5.8)\,\% \\
\sigma\left(\frac{\mathcal{B}(B^+ \to D^{*-} \pi^+ \mu^+ \nu_\mu)}{\mathcal{B}(B^+ \to \overline{D}^{*0} \mu^+ \nu_\mu)}\right) &= (\pm 17.2 \pm 4.4)\,\% \\
\sigma\left(\frac{\mathcal{B}(B^0 \to D^- \pi^0 \mu^+ \nu_\mu)}{\mathcal{B}(B^0 \to D^{*-} \mu^+ \nu_\mu)}\right) &= (\pm 16.5 \pm 4.1)\,\% \\
\sigma\left(\frac{\mathcal{B}(B^+ \to \overline{D}^0 \pi^0 \mu^+ \nu_\mu)}{\mathcal{B}(B^+ \to \overline{D}^{*0} \mu^+ \nu_\mu)}\right) &= (\pm 17.0 \pm 3.3)\,\% \\
\sigma\left(\frac{\mathcal{B}(B^0 \to D^{*-} \pi^0 \mu^+ \nu_\mu)}{\mathcal{B}(B^0 \to D^{*-} \mu^+ \nu_\mu)}\right) &= (\pm 17.5 \pm 1.7)\,\% \\
\sigma\left(\frac{\mathcal{B}(B^+ \to \overline{D}^{*0} \pi^0 \mu^+ \nu_\mu)}{\mathcal{B}(B^+ \to \overline{D}^{*0} \mu^+ \nu_\mu)}\right) &= (\pm 14.9 \pm 0.7)\,\%
\end{aligned}
\tag{8.12}
$$

8.5.4. Combined normalised branching ratios

After the determination of the normalised branching ratio for each light charged lepton separately, the results can also be combined into one final result for both lepton categories together.
One approach to combine these two measurements is the best linear unbiased estimate (BLUE) method [179, 180], where the correlation between the uncertainties is correctly taken into account. In this analysis the result for the electron including its uncertainty is given by $\theta_e = \hat{\theta}_e \pm \sigma_e$ and the result for the muon with the corresponding uncertainty is given by $\theta_\mu = \hat{\theta}_\mu \pm \sigma_\mu$.
The estimation of combined uncertainties in this case is equal to a χ^2 minimisation, which is equivalent to a maximum-likelihood estimation in case of a Gaussian distribution.
Therefore, the following formula gives the BLUE estimation for the combination of both charged light leptons:

$$\hat{\theta} = \frac{\hat{\theta}_e(\sigma_\mu^2 - \rho\sigma_e\sigma_\mu) + \hat{\theta}_\mu(\sigma_e^2 - \rho\sigma_e\sigma_\mu)}{\sigma_e^2 - 2\rho\sigma_e\sigma_\mu + \sigma_\mu^2} \tag{8.13}$$

with the variance:

$$\sigma_{e\mu}^2 = \frac{\sigma_e^2\sigma_\mu^2(1-\rho^2)}{\sigma_e^2 - 2\rho\sigma_e\sigma_\mu + \sigma_\mu^2}. \tag{8.14}$$

Here, ρ is given by:

$$\rho = \frac{V_{e\mu}}{\sigma_e\sigma_\mu}, \tag{8.15}$$

with V being the covariance matrix.
The covariance matrix can be split into a correlated and an uncorrelated component as follows:

$$V = \begin{pmatrix} \sigma_{e,\text{uncorr}}^2 & 0 \\ 0 & \sigma_{\mu,\text{uncorr}}^2 \end{pmatrix} + \begin{pmatrix} \sigma_{e,\text{corr}}^2 & \sigma_{e,\text{corr}}\sigma_{\mu,\text{corr}} \\ \sigma_{e,\text{corr}}\sigma_{\mu,\text{corr}} & \sigma_{\mu,\text{corr}}^2 \end{pmatrix}. \tag{8.16}$$

The uncertainties in this analysis that are assumed to be uncorrelated are the systematic uncertainties arising from to the lepton identification as well as the statistics of the considered data set. All the other uncertainties are assumed to be fully correlated.
The determined results for the relative uncertainties are the following, where the first

error is statistical and the second of systematic nature:

$$
\begin{aligned}
\sigma\left(\frac{\mathcal{B}(B^0 \to \overline{D}^0\pi^-\ell^+\nu_\ell)}{\mathcal{B}(B^0 \to D^{*-}\ell^+\nu_\ell)}\right) &= (\pm 9.3 \pm 0.5)\,\% \\
\sigma\left(\frac{\mathcal{B}(B^+ \to D^-\pi^+\ell^+\nu_\ell)}{\mathcal{B}(B^+ \to \overline{D}^{*0}\ell^+\nu_\ell)}\right) &= (\pm 10.7 \pm 0.1)\,\% \\
\sigma\left(\frac{\mathcal{B}(B^0 \to \overline{D}^{*0}\pi^-\ell^+\nu_\ell)}{\mathcal{B}(B^0 \to D^{*-}\ell^+\nu_\ell)}\right) &= (\pm 9.3 \pm 0.5)\,\% \\
\sigma\left(\frac{\mathcal{B}(B^+ \to D^{*-}\pi^+\ell^+\nu_\ell)}{\mathcal{B}(B^+ \to \overline{D}^{*0}\ell^+\nu_\ell)}\right) &= (\pm 11.0 \pm 0.4)\,\% \\
\sigma\left(\frac{\mathcal{B}(B^0 \to D^-\pi^0\ell^+\nu_\ell)}{\mathcal{B}(B^0 \to D^{*-}\ell^+\nu_\ell)}\right) &= (\pm 10.9 \pm 2.6)\,\% \\
\sigma\left(\frac{\mathcal{B}(B^+ \to \overline{D}^0\pi^0\ell^+\nu_\ell)}{\mathcal{B}(B^+ \to \overline{D}^{*0}\ell^+\nu_\ell)}\right) &= (\pm 12.7 \pm 2.4)\,\% \\
\sigma\left(\frac{\mathcal{B}(B^0 \to D^{*-}\pi^0\ell^+\nu_\ell)}{\mathcal{B}(B^0 \to D^{*-}\ell^+\nu_\ell)}\right) &= (\pm 11.2 \pm 1.1)\,\% \\
\sigma\left(\frac{\mathcal{B}(B^+ \to \overline{D}^{*0}\pi^0\ell^+\nu_\ell)}{\mathcal{B}(B^+ \to \overline{D}^{*0}\ell^+\nu_\ell)}\right) &= (\pm 9.0 \pm 0.6)\,\%.
\end{aligned}
\tag{8.17}
$$

All combined branching ratios uncertainties are in the order of $\sim$10 % and limited by the statistical precision of the measurement.

CHAPTER 9

Conclusion and Outlook

In this chapter the results of the performed analysis are compared with previous measurements at the other two B factories *BABAR* and *Belle*, and an outlook into the future with more data at Belle II is given.

9.1. Discussion of results

In this thesis, the first measurement of the $B \to D^{**}\ell\nu_\ell$ decay branching ratio at the Belle II experiment with the data set collected in the time period between 2019 and 2022 has been performed. Compared to previous measurements, D^{**} meson decays into a $D^{(*)}$and a π^0 meson are explicitly reconstructed and considered as additional templates in a binned maximum likelihood fit. However, due to the low reconstruction efficiency of the π^0 reconstruction channels in the D^{**} meson decays, the precision is improved with combined scaling parameters for the fit templates using isospin relations. In addition, there exists some overlap between the differently reconstructed $B \to D^{**}\ell\nu_\ell$ decay channels. Therefore, instead of fitting each reconstructed $B \to D^{**}\ell\nu_\ell$ decay channel separately, one simultaneous fit is performed.
Due to the fact that there might be some effects in the simulation that are not well understood, the branching ratio for the $B \to D^{**}\ell\nu_\ell$ decays is normalised by the $B \to D^{*}\ell\nu_\ell$ branching ratio, as this decay rate is much higher and generally better understood. By considering the ratio of two decay rates, sources of systematic uncertainties common to both modes cancel out, at least partially.
Several studies on the reliability of the simulation as well as the signal and normalisation fit have been performed, followed by the determination of the normalised branching ratio combined for both charged leptons.
Since the determined results are not an official Belle II result, only the uncertainties can be shown and thus only these can be compared to the previous measurements by

BABAR [84] and *Belle* [94], summarised in table 2.1.
The determined normalised and combined uncertainties for the different modes can be seen in eq. (8.17).
As the measurement is statistically limited, the relative statistical uncertainties for the three measurements are compared for the charged π meson decays of the D^{**} mesons, as the neutral π modes were previously only inferred from isospin symmetry.
The calculated relative statistical uncertainties for the *BABAR* experiment, which is also statistically limited, vary from around 9 to 19 %, depending on the reconstructed $B \to D^{**}\ell\nu_\ell$ decay mode. In contrast, the measured values in this analysis are between 9 and 11 %. The recorded data set by the *BABAR* experiment corresponds roughly to the data set collected with the Belle II experiment, therefore, the statistical uncertainties and thus the considered methods can be directly compared and the different detector setups can be neglected.
It can be seen that the measurement by *BABAR* from 2008 is slightly worse than the presented measurement in this thesis, hence it seems that the maximum likelihood fit as well as the additional reconstruction of the D^{**} meson into $D^{(*)}\pi^0$ combinations yields a slight improvement.
For the *Belle* experiment the calculated relative statistical uncertainties lay in the range between 4 to 5 %, again depending on the reconstructed D^{**} meson decay mode, only considering the charged π mesons. This performed measurement is already systematically limited, at least for some of the reconstructed $B \to D^{**}\ell\nu_\ell$ decay channels.
The *Belle* experiment has accumulated about twice as much data as what the Belle II experiment has recorded so far. Therefore, the recently performed measurement using the full *Belle* data set has a slightly higher precision than the performed analysis in this thesis, when scaling the uncertainty to the same luminosity. However, this *Belle* analysis is a re-analysis, using optimised cuts and also the FEI instead of the FR, of the performed analysis in [181], which is also partially statistically and partially systematically limited in precision depending on the $B \to D^{**}\ell\nu_\ell$ reconstruction mode. As seen in the two *Belle* measurements, more data allows for a harder selection, which results in a disproportionately high improvement of the statistical uncertainty. Here, the precision achieved by the original *Belle* measurement is slightly worse than the precision achieved using the current Belle II data set.
Compared to previous measurements, this analysis uses a binned maximum likelihood instead of a PDF fit for the first time. The performed fit in this analysis is based on the modelling of the simulation, which is the best known theory to generate events, as opposed to using PDFs, which are a simplified modelling of the fit variable using only a few parameters. Moreover, the binned maximum likelihood fit directly includes the systematic uncertainties as NPs in the fitting procedure.

9.2. Outlook

Presented here is the first measurement of the branching ratio $B \to D^{**}\ell\nu_\ell$ using the first part of the Belle II data set. This analysis is therefore highly statistically limited, which means that major improvements are possible using a bigger data sample. This is however possible with the Belle II experiment as after the scheduled long-shut-down one, which ended in early 2024, the plan is to record more data with a partly upgraded detector. As a result, the statistical uncertainties on the measured branching ratio will drastically decrease.
In addition to more experimental data, it is crucial to also understand the detector, which is naturally achieved by a longer running period of the experiment. As a consequence the systematic uncertainties originating from inefficiencies in the detector reconstruction will also become smaller.
However, not only the detector needs to be understood better, but also a good theoretical description of e.g. the form factors is needed. Therefore, new models or improvements on the theoretical understanding are another key aspect to improve the analysis.
Besides, the hadronic FEI, which is used for the B_{Tag} meson reconstruction needs further extensive studies as there are still a few features that are not so well understood at Belle II. It was one of the leading systematic uncertainties for both the normalisation $B \to D^{*}\ell\nu_\ell$ and the signal $B \to D^{**}\ell\nu_\ell$ on the measured branching ratios. As this analysis measures a ratio, this is not so crucial, but understanding the main contributions to a measurement is always important.
In general, it can be said that more recorded data will significantly improve the determined result and might even help to constrain the contributions to the gap between the inclusively and exclusively measured branching ratios. In the current description of the gap, resonant contributions originating from D^{**} mesons are considered, as stated in section 4.2.1, where the resonance decays into the two pion ($D^{**} \to D^{(*)}\pi\pi$) state. This is however not a valid theoretical approach as stated in [118]. Nonetheless this gap needs to be filled with yet unmeasured processes, and understanding the $B \to D^{**}\ell\nu_\ell$ branching ratios into the one and two pion states will contribute to that. Therefore, performing this analysis again by also considering the two pion state in the reconstruction is something to investigate with a bigger data set.
The above mentioned suggestions should be possible within the next year or two, when the Belle II data set matches the recorded *Belle* data set.
Another interesting analysis that could be performed towards the middle of the run time of the Belle II experiment, is the actual measurement of the D^{**} meson branching ratios for the four known resonances D_0^*, D_1', D_1 and D_2^* and not just only $D^{(*)}\pi$ or $D^{(*)}\pi\pi$ combinations, meaning the investigation of the invariant mass spectra for the different $D^{(*)}\pi$ and $D^{(*)}\pi\pi$ combinations and which D^{**} meson contributes to which combination. On top of that, it is possible to look for unknown resonances that decay to $D^{(*)}\pi(\pi)$.
This can then be extended towards the end of the Belle II run time to a ratio measurement between the heavy charged lepton the τ and the two light charged leptons, the

electron and the muon [182, 183]. Thus the ratio is given by:

$$R(D^{**}) = \frac{\Gamma(B \to D^{**}\tau\nu_\tau)}{\Gamma(B \to D^{**}\ell\nu_\ell)}. \tag{9.1}$$

Substituting the D^{**} meson with either the D or the D^* meson in eq. (9.1) has already shown some tension with the SM expectation [78]. Therefore, measuring this ratio with a D^{**} meson instead of the $D^{(*)}$ mesons can be considered another probe of the SM.
This lepton flavour universality test assumes that the weak interaction couples identically to all charged leptons. If this turns out to not be the case, it could hint towards new physics beyond the SM.
One possibility could be a charged Higgs boson that would mediate the interaction instead of the charged W boson. This charged Higgs boson could originate from an extension of the SM like the two-Higgs-doublet model (2HDM) [184]. The 2HDM introduces another Higgs doublet instead of only one considered for the SM. Due to the introduction of an additional Higgs doublet, there are five physical scalars that can be measured, the CP even neutral h and H, where the latter is heavier than the former, the CP odd pseudoscalar A and the two charged Higgs bosons $H^{\pm}$. Due to the fact that the Higgs bosons couple to the mass of the particle, the coupling to the much heavier τ lepton in the ratio in eq. (9.1) is favoured over the coupling to the light charged leptons and therefore, the measured value would deviate from the SM prediction in case of an additional charged Higgs boson.
Another possibility to explain a possible deviation from the SM would be leptoquarks [185]. These leptoquarks are assumed to exist in numerous extensions of the SM, such as grand unified theories (GUT). In a GUT, the strong, the electromagnetic and the weak interaction are joined together into one force described by a single gauge group at high energies.
These leptoquarks are able to interact both with leptons and quarks and thus carry lepton and baryon number. Therefore, the introduction of a leptoquark would yield an additional decay possibility that impacts the ratio.
The measurement conducted at Belle II hence represents an initial exploration of these novel physics processes, by later investigating e.g. the ratio defined in eq. (9.1).

Bibliography

[1] J. J. Thomson, *XL. Cathode Rays*, The London, Edinburgh, and Dublin Philosophical Magazine and Journal of Science **44** (1897) 293–316.

[2] E. Rutherford, *LXXIX. The scattering of α and β particles by matter and the structure of the atom*, The London, Edinburgh, and Dublin Philosophical Magazine and Journal of Science **21** (1911) 669–688.

[3] E. Rutherford, *LIV. Collision of α particles with light atoms. IV. An anomalous effect in nitrogen*, Phil. Mag. Ser. 6 **37** (1919) 581–587.

[4] J. Chadwick, *The Existence of a Neutron*, Proc. Roy. Soc. Lond. A **136** (1932) 692–708.

[5] C. D. Anderson and S. H. Neddermeyer, *Cloud Chamber Observations of Cosmic Rays at 4300 Meters Elevation and Near Sea-Level*, Physical Review **50** (1936) 263–271.

[6] C. M. G. Lattes, et al., *Processes involving charged mesons*, Nature **159** (1947) 694–697.

[7] A. Einstein, *Über einen die Erzeugung und Verwandlung des Lichtes betreffenden heuristischen Gesichtspunkt*, Annalen der Physik **322** (1905) 132–148.

[8] A. Einstein, *Über die von der molekularkinetischen Theorie der Wärme geforderte Bewegung von in ruhenden Flüssigkeiten suspendierten Teilchen*, Annalen der Physik **322** (1905) 549–560.

[9] A. Einstein, *Zur Elektrodynamik bewegter Körper*, Annalen der Physik **322** (1905) 891–921.

[10] A. Einstein, *Ist die Trägheit eines Körpers von seinem Energieinhalt abhängig?*, Annalen der Physik **323** (1905) 639–641.

[11] M. Planck, *Über das Gesetz der Energieverteilung im Normalspectrum*, Annalen der Physik **309** (1901) 553–563.

[12] E. Schrödinger, *Quantisierung als Eigenwertproblem*, Annalen der Physik **386** (1926) 109–139.

[13] W. Heisenberg, *Über quantentheoretische Umdeutung kinematischer und mechanischer Beziehungen.*, Zeitschrift für Physik **33** (1925).

[14] M. Born and P. Jordan, *Zur Quantenmechanik*, Zeitschrift für Physik **34** (1925).

[15] W. Heisenberg, M. Born, and P. Jordan, *Zur Quantenmechanik II*, Zeitschrift für Physik **35** (1926).

[16] P. A. M. Dirac and N. H. D. Bohr, *The quantum theory of the emission and absorption of radiation*, Proceedings of the Royal Society of London. Series A, Containing Papers of a Mathematical and Physical Character **114** (1927) 243–265.

[17] P. A. M. Dirac and R. H. Fowler, *The quantum theory of the electron*, Proceedings of the Royal Society of London. Series A, Containing Papers of a Mathematical and Physical Character **117** (1928) 610–624.

[18] R. P. Feynman, *The Theory of Positrons*, Phys. Rev. **76** (1949) 749–759.

[19] P. A. M. Dirac, *Quantum theory of emission and absorption of radiation*, Proc. Roy. Soc. Lond. A **114** (1927) 243.

[20] E. Fermi, *Quantum Theory of Radiation*, Rev. Mod. Phys. **4** (1932) 87–132.

[21] S. Tomonaga, *On a relativistically invariant formulation of the quantum theory of wave fields*, Prog. Theor. Phys. **1** (1946) 27–42.

[22] J. Schwinger, *On Quantum-Electrodynamics and the Magnetic Moment of the Electron*, Phys. Rev. **73** (1948) 416–417.

[23] J. Schwinger, *Quantum Electrodynamics. I. A Covariant Formulation*, Phys. Rev. **74** (1948) 1439–1461.

[24] R. P. Feynman, *Space-Time Approach to Non-Relativistic Quantum Mechanics*, Rev. Mod. Phys. **20** (1948) 367–387.

[25] R. P. Feynman, *Mathematical Formulation of the Quantum Theory of Electromagnetic Interaction*, Phys. Rev. **80** (1950) 440–457.

[26] F. J. Dyson, *The Radiation Theories of Tomonaga, Schwinger, and Feynman*, Phys. Rev. **75** (1949) 486–502.

[27] F. J. Dyson, *The S Matrix in Quantum Electrodynamics*, Phys. Rev. **75** (1949) 1736–1755.

[28] M. Gell-Mann, *A Schematic Model of Baryons and Mesons*, Phys. Lett. **8** (1964) 214–215.

[29] G. Zweig, *An SU_3 model for strong interaction symmetry and its breaking; Version 2*, https://cds.cern.ch/record/570209.

[30] H. Fritzsch, M. Gell-Mann, and H. Leutwyler, *Advantages of the color octet gluon picture*, Phys. Lett. B **47** (1973) 365–368.

[31] D. J. Gross and F. Wilczek, *Asymptotically free gauge theories. 2.*, Phys. Rev. D **9** (1974) 980–993.

[32] S. Weinberg, *Non-Abelian Gauge Theories of the Strong Interactions*, Phys. Rev. Lett. **31** (1973) 494–497.

[33] G. Arnison, et al., *Experimental observation of isolated large transverse energy electrons with associated missing energy at s=540 GeV*, Physics Letters B **122** (1983) 103–116.

[34] M. Banner, et al., *Observation of single isolated electrons of high transverse momentum in events with missing transverse energy at the CERN $p\bar{p}$ collider*, Physics Letters B **122** (1983) 476–485.

[35] G. Arnison, et al., *Experimental observation of lepton pairs of invariant mass around 95 GeV c^{-2} at the CERN SPS collider*, Physics Letters B **126** (1983) 398–410.

[36] P. Bagnaia, et al., *Evidence for $Z^0 \to e^+e^-$ at the CERN pp collider*, Physics Letters B **129** (1983) 130–140.

[37] S. L. Glashow, *Partial-symmetries of weak interactions*, Nuclear Physics **22** (1961) 579–588.

[38] S. Weinberg, *A Model of Leptons*, Phys. Rev. Lett. **19** (1967) 1264–1266.

[39] A. Salam, *Weak and Electromagnetic Interactions*, Conf. Proc. C **680519** (1968) 367–377.

[40] S. W. Herb, et al., *Observation of a Dimuon Resonance at 9.5 GeV in 400-GeV Proton-Nucleus Collisions*, Phys. Rev. Lett. **39** (1977) 252–255.

[41] TASSO Collaboration, R. Brandelik et al., *Evidence for Planar Events in e^+e^- Annihilation at High-Energies*, Phys. Lett. B **86** (1979) 243–249.

[42] D. P. Barber et al., *Discovery of Three Jet Events and a Test of Quantum Chromodynamics at PETRA Energies*, Phys. Rev. Lett. **43** (1979) 830.

[43] PLUTO Collaboration, C. Berger et al., *Evidence for Gluon Bremsstrahlung in e^+e^- Annihilations at High-Energies*, Phys. Lett. B **86** (1979) 418–425.

[44] JADE Collaboration, W. Bartel et al., *Observation of Planar Three Jet Events in e^+e^- Annihilation and Evidence for Gluon Bremsstrahlung*, Phys. Lett. B **91** (1980) 142–147.

[45] F. Abe, et al., *Observation of Top Quark Production in $p\bar{p}$ Collisions with the Collider Detector at Fermilab*, Phys. Rev. Lett. **74** (1995) 2626–2631.

[46] S. Abachi, et al., *Observation of the Top Quark*, Phys. Rev. Lett. **74** (1995) 2632–2637.

[47] K. Kodama, et al., *Observation of tau neutrino interactions*, Physics Letters B **504** (2001) 218–224.

[48] ATLAS Collaboration, G. Aad, et al., *Observation of a new particle in the search for the Standard Model Higgs boson with the ATLAS detector at the LHC*, Phys. Lett. B **716** (2012) 1–29.

[49] CMS Collaboration, S. Chatrchyan et al., *Observation of a New Boson at a Mass of 125 GeV with the CMS Experiment at the LHC*, Phys. Lett. B **716** (2012) 30–61.

[50] A. D. Sakharov, *Violation of CP invariance, C asymmetry, and baryon asymmetry of the universe*, Soviet Physics Uspekhi **34** (1991) 392.

[51] S. L. Glashow, J. Iliopoulos, and L. Maiani, *Weak Interactions with Lepton-Hadron Symmetry*, Phys. Rev. D **2** (1970) 1285–1292.

[52] H. Georgi and S. L. Glashow, *Unified weak and electromagnetic interactions without neutral currents*, Phys. Rev. Lett. **28** (1972) 1494.

[53] D. J. Gross and F. Wilczek, *Ultraviolet Behavior of Nonabelian Gauge Theories*, Phys. Rev. Lett. **30** (1973) 1343–1346.

[54] H. D. Politzer, *Reliable Perturbative Results for Strong Interactions?*, Phys. Rev. Lett. **30** (1973) 1346–1349.

[55] G. 't Hooft, *Renormalization of Massless Yang-Mills Fields*, Nucl. Phys. B **33** (1971) 173–199.

[56] G. 't Hooft, *Renormalizable Lagrangians for Massive Yang-Mills Fields*, Nucl. Phys. B **35** (1971) 167–188.

[57] G. 't Hooft and M. J. G. Veltman, *Regularization and Renormalization of Gauge Fields*, Nucl. Phys. B **44** (1972) 189–213.

[58] G. 't Hooft and M. J. G. Veltman, *Combinatorics of gauge fields*, Nucl. Phys. B **50** (1972) 318–353.

[59] LHCb Collaboration, R. Aaij, et al., *Observation of $J/\psi p$ Resonances Consistent with Pentaquark States in $\Lambda_b^0 \to J/\psi K^- p$ Decays*, Phys. Rev. Lett. **115** (2015).

[60] LHCb Collaboration, R. Aaij, et al., *Observation of a $J/\psi\Lambda$ Resonance Consistent with a Strange Pentaquark Candidate in $B^- \to J/\psi\Lambda\bar{p}$ Decays*, Phys. Rev. Lett. **131** (2023) 031901.

[61] LHCb Collaboration, R. Aaij et al., *First Observation of a Doubly Charged Tetraquark and Its Neutral Partner*, Phys. Rev. Lett. **131** (2023) 041902.

[62] R. Davis, D. S. Harmer, and K. C. Hoffman, *Search for Neutrinos from the Sun*, Phys. Rev. Lett. **20** (1968) 1205–1209.

[63] M. Gell-Mann, *Symmetries of Baryons and Mesons*, Phys. Rev. **125** (1962) 1067–1084.

[64] P. Higgs, *Broken symmetries, massless particles and gauge fields*, Phys. Lett. **12** (1964) 132–133.

[65] F. Englert and R. Brout, *Broken Symmetry and the Mass of Gauge Vector Mesons*, Phys. Rev. Lett. **13** (1964) 321–323.

[66] E. Noether, *Invariante Variationsprobleme*, Nachrichten von der Gesellschaft der Wissenschaften zu Göttingen, Mathematisch-Physikalische Klasse **1918** (1918) 235–257.

[67] G. Lüders, *On the Equivalence of Invariance under Time Reversal and under Particle-Antiparticle Conjugation for Relativistic Field Theories*, Kong. Dan. Vid. Sel. Mat. Fys. Med. **28N5** (1954) 1–17.

[68] C. S. Wu, et al., *Experimental Test of Parity Conservation in Beta Decay*, Phys. Rev. **105** (1957) 1413–1415.

[69] J. H. Christenson, et al., *Evidence for the 2π Decay of the K_2^0 Meson*, Phys. Rev. Lett. **13** (1964) 138–140.

[70] Particle Data Group Collaboration, R. L. Workman and Others, *Review of Particle Physics*, PTEP **2022** (2022) 083C01.

[71] BABAR Collaboration, J. P. Lees, et al., *Observation of Time-Reversal Violation in the B^0 Meson System*, Phys. Rev. Lett. **109** (2012) 211801.

[72] N. Cabibbo, *Unitary Symmetry and Leptonic Decays*, Phys. Rev. Lett. **10** (1963) 531–533.

[73] S. L. Glashow, J. Iliopoulos, and L. Maiani, *Weak Interactions with Lepton-Hadron Symmetry*, Phys. Rev. D **2** (1970) 1285–1292.

[74] M. Kobayashi and T. Maskawa, *CP Violation in the Renormalizable Theory of Weak Interaction*, Prog. Theor. Phys. **49** (1973) 652–657.

[75] L.-L. Chau and W.-Y. Keung, *Comments on the Parametrization of the Kobayashi-Maskawa Matrix*, Phys. Rev. Lett. **53** (1984) 1802–1805.

[76] L. Wolfenstein, *Parametrization of the Kobayashi-Maskawa Matrix*, Phys. Rev. Lett. **51** (1983) 1945–1947.

[77] J. Charles, et al., *CP violation and the CKM matrix: assessing the impact of the asymmetric B factories*, The European Physical Journal C **41** (2005) 1–131, updated results and plots available at `http://ckmfitter.in2p3.fr`.

[78] HFLAV Collaboration, Y. Amhis, et al., *Averages of b-hadron, c-hadron, and τ-lepton properties as of 2021*, Phys. Rev. D **107** (2023).

[79] BABAR Collaboration, B. Aubert, et al., *Determination of the form factors for the decay $B^0 \to D^{*-} l^+ \nu_l$ and of the CKM matrix element $|V_{cb}|$*, Phys. Rev. D **77** (2008) 032002.

[80] A. K. Leibovich, et al., *Semileptonic B decays to excited charmed mesons*, Phys. Rev. D **57** (1998) 308–330.

[81] N. Isgur and M. B. Wise, *Spectroscopy with heavy-quark symmetry*, Phys. Rev. Lett. **66** (1991) 1130–1133.

[82] D. Liventsev, et al., *Study of $B \to D^{**} \ell\nu$ with full reconstruction tagging*, Phy. Rev. D **77** (2008).

[83] B. Aubert, et al., *Measurement of Semileptonic B Decays into Orbitally Excited Charmed Mesons*, Phys. Rev. Lett. **103** (2009).

[84] B. Aubert, et al., *Measurement of the Branching Fractions of $B \to D^{**} \ell\nu$ Decays in Events Tagged by a Fully Reconstructed B Meson*, Phys. Rev. Lett. **101** (2008).

[85] BaBar Collaboration, B. Aubert et al., *Study of the decays $B^- \to D^{(*)+} \pi^- \pi^-$*, in *21st International Symposium on Lepton and Photon Interactions at High Energies (LP 03)*. 8, 2003. `arXiv:hep-ex/0308026`.

[86] I. Bigi, et al., *Memorino on the '1/2 versus 3/2 puzzle' in $\overline{B} \to \ell\bar{\nu} X_c$ a year later and a bit wiser*, The European Physical Journal C **52** (2007) 975–985.

[87] V. Morénas, et al., *Quantitative predictions for B semileptonic decays into D, D^* and the orbitally excited D^{**} in quark models in the manner of Bakamjian and Thomas*, Phys. Rev. D **56** (1997) 5668–5680.

[88] M. Albaladejo, et al., *Two-pole structure of the $D_0^*(2400)$*, Phys. Lett. B **767** (2017) 465–469.

[89] M.-L. Du, et al., *Towards a new paradigm for heavy-light meson spectroscopy*, Phys. Rev. D **98** (2018).

[90] F.-K. Guo, et al., *Hadronic molecules*, Reviews of Modern Physics **90** (2018).

[91] G. Moir, et al., *Coupled-channel $D\pi$, $D\eta$ and $D_s\overline{K}^0$ scattering from lattice QCD*, Journal of High Energy Physics **2016** (2016).

[92] A. Le Yaouanc, J.-P. Leroy, and P. Roudeau, *Model for nonleptonic and semileptonic decays by $\overline{B}^0 \to D^{**}$ transitions with* $\mathrm{BR}(j = 1/2) \ll \mathrm{BR}(j = 3/2)$ *using the Leibovich-Ligeti-Stewart-Wise scheme*, Phys. Rev. D **105** (2022) 013004.

[93] A. Vossen, et al., *Measurement of the branching fraction of $B \to D^{(*)}\pi\ell\nu$ at Belle using hadronic tagging in fully reconstructed events*, Phys. Rev. D **98** (2018).

[94] Belle Collaboration, F. Meier, et al., *First observation of $B \to \overline{D}_1(\to \overline{D}\pi^+\pi^-)\ell^+\nu_\ell$ and measurement of the $B \to \overline{D}^{(*)}\pi\ell^+\nu_\ell$ and $B \to \overline{D}^{(*)}\pi^+\pi^-\ell^+\nu_\ell$ branching fractions with hadronic tagging at Belle*, Phys. Rev. D **107** (2023) 092003.

[95] J. Lees, et al., *Observation of $\overline{B} \to D^{(*)}\pi^+\pi^-\ell^-\bar{\nu}$ Decays in e^+e^- Collisions at the $\Upsilon(4S)$ Resonance*, Phys. Rev. Lett. **116** (2016).

[96] T. Abe et al., *Belle II Technical Design Report*, 2010.

[97] Belle Collaboration, A. Abashian et al., *The Belle Detector*, Nucl. Instrum. Meth. A **479** (2002) 117–232.

[98] J. Brodzicka, et al., *Physics achievements from the Belle experiment*, Progress of Theoretical and Experimental Physics **2012** (2012), 04D001.

[99] A. J. Bevan, et al., *The Physics of the B Factories*, The European Physical Journal C **74** (2014).

[100] K. Akai, K. Furukawa, and H. Koiso, *SuperKEKB collider*, Nuclear Instruments and Methods in Physics Research Section A: Accelerators, Spectrometers, Detectors and Associated Equipment **907** (2018) 188–199, Advances in Instrumentation and Experimental Methods (Special Issue in Honour of Kai Siegbahn).

[101] S. Kurokawa and E. Kikutani, *Overview of the KEKB accelerators*, Nuclear Instruments and Methods in Physics Research Section A: Accelerators, Spectrometers, Detectors and Associated Equipment **499** (2003) 1–7, KEK-B: The KEK B-factory.

[102] SuperB Collaboration, *SuperB: A High-Luminosity Asymmetric e^+e^- Super Flavor Factory. Conceptual Design Report*, 2007.

[103] E. Kou, et al., *The Belle II Physics Book*, Progress of Theoretical and Experimental Physics **2019** (2019).

[104] *Belle II Detector 3D model*, https://www.belle2.org/archives/, December 21, 2023.

[105] A. Natochii, et al., *Measured and projected beam backgrounds in the Belle II experiment at the SuperKEKB collider*, Nuclear Instruments and Methods in Physics Research Section A: Accelerators, Spectrometers, Detectors and Associated Equipment **1055** (2023) 168550.

[106] J. Kemmer and G. Lutz, *New detector concepts*, Nuclear Instruments and Methods in Physics Research Section A: Accelerators, Spectrometers, Detectors and Associated Equipment **253** (1987) 365–377.

[107] A. Moll et al., *The vertex detector numbering scheme*, BELLE2-NOTE-TE-2015-010 (2011).

[108] H. Bethe, *Zur Theorie des Durchgangs schneller Korpuskularstrahlen durch Materie*, Annalen der Physik **397** (1930) 325–400.

[109] Belle II Collaboration, *Belle II Luminosity*, 2023. https://confluence.desy.de/display/BI/Belle+II+Luminosity. Access date: 2023-10-18.

[110] D. J. Lange, *The EvtGen particle decay simulation package*, Nuclear Instruments and Methods in Physics Research Section A: Accelerators, Spectrometers, Detectors and Associated Equipment **462** (2001) 152–155, BEAUTY2000, Proceedings of the 7th Int. Conf. on B-Physics at Hadron Machines.

[111] S. Agostinelli, et al., *Geant4—a simulation toolkit*, Nuclear Instruments and Methods in Physics Research Section A: Accelerators, Spectrometers, Detectors and Associated Equipment **506** (2003) 250–303.

[112] T. Kuhr, et al., *The Belle II Core Software*, Computing and Software for Big Science **3** (2018).

[113] Belle II Collaboration, I. Adachi, et al., *Belle II Analysis Software Framework (basf2)*, Aug., 2022. https://doi.org/10.5281/zenodo.6949513.

[114] E. Barberio, B. van Eijk, and Z. Wa s, *Photos — a universal Monte Carlo for QED radiative corrections in decays*, Comput. Phys. Commun. **66** (1991) 115–128.

[115] E. Barberio and Z. Was, *PHOTOS: A Universal Monte Carlo for QED radiative corrections. Version 2.0*, Comput. Phys. Commun. **79** (1994) 291–308.

[116] A. Natochii, et al., *Beam background expectations for Belle II at SuperKEKB*, 2022.

[117] Belle Collaboration, L. Cao, et al., *Measurements of partial branching fractions of inclusive $B \to X_u \ell^+ \nu_\ell$ decays with hadronic tagging*, Phys. Rev. D **104** (2021).

[118] E. J. Gustafson, et al., *A model independent description of $B \to D\pi\ell\nu$ decays*, arXiv:2311.00864 [hep-ph].

[119] F. U. Bernlochner, et al., *Constrained second-order power corrections in HQET: $R(D^{(*)})$, $|V_{cb}|$, and new physics*, Phys. Rev. D **106** (2022).

[120] F. U. Bernlochner, Z. Ligeti, and D. J. Robinson, *Model-independent analysis of semileptonic B decays to D^{**} for arbitrary new physics*, Phys. Rev. D **97** (2018) 075011.

[121] F. U. Bernlochner and Z. Ligeti, *Semileptonic $B_{(s)}$ decays to excited charmed mesons with e, μ, τ and searching for new physics with $R(D^{**})$*, Phys. Rev. D **95** (2017) 014022.

[122] F. U. Bernlochner, et al., *Das ist der HAMMER: consistent new physics interpretations of semileptonic decays*, The European Physical Journal C **80** (2020).

[123] S. Jadach, B. Ward, and Z. Wa s, *The precision Monte Carlo event generator KK for two-fermion final states in e^+e^- collisions*, Comput. Phys. Commun. **130** (2000) 260–325.

[124] T. Sjöstrand, et al., *An introduction to PYTHIA 8.2*, Comput. Phys. Commun. **191** (2015) 159–177.

[125] S. Jadach, J. H. Kühn, and Z. Was, *TAUOLA - a library of Monte Carlo programs to simulate decays of polarized τ leptons*, Comput. Phys. Commun. **64** (1991) 275–299.

[126] A. Géron, *Hands-on machine learning with Scikit-Learn and TensorFlow : concepts, tools, and techniques to build intelligent systems*. O'Reilly Media, Sebastopol, CA, 2017.

[127] L. Breiman, *Bagging Predictors*, Machine Learning **24** (1996) 123–140.

[128] Y. Freund and R. E. Schapire, *A Decision-Theoretic Generalization of On-Line Learning and an Application to Boosting*, Journal of Computer and System Sciences **55** (1997) 119–139.

[129] J. H. Friedman, *Greedy function approximation: A gradient boosting machine.*, The Annals of Statistics **29** (2001) 1189 – 1232.

[130] J. H. Friedman, *Stochastic gradient boosting*, Computational Statistics Data Analysis **38** (2002) 367–378, Nonlinear Methods and Data Mining.

[131] T. Keck, *FastBDT: A Speed-Optimized Multivariate Classification Algorithm for the Belle II Experiment*, Computing and Software for Big Science **1** (2017) .

[132] T. Keck, et al., *The Full Event Interpretation*, Computing and Software for Big Science **3** (2019).

[133] Belle Collaboration, D. Liventsev, et al., *Study of $B \to D^{**} l\nu$ with full reconstruction tagging*, Phys. Rev. D **77** (2008) 091503.

[134] K.-F. Chen, et al., *Search for $B \to h^{(*)}\nu\bar{\nu}$ Decays at Belle*, Phys. Rev. Lett. **99** (2007).

[135] K. Ikado, et al., *Evidence of the Purely Leptonic Decay $B^- \to \tau\bar{\nu_\tau}$*, Phys. Rev. Lett. **97** (2006).

[136] D. Liventsev, et al., *Measurement of the branching fractions for $B^- \to D^{(*)+}\pi^-\ell^-\nu_\ell$ and $B^0 \to D^{(*)0}\pi^+\ell^-\nu_\ell$ and B*, Phys. Rev. D **72** (2005) 51109.

[137] I. Bizjak, et al., *Determination of $|V_{\rm ub}|$ from Measurements of the Inclusive Charmless Semileptonic Partial Rates of B Mesons using Full Reconstruction Tags*, Phys. Rev. Lett. **95** (2005).

[138] M. Feindt, et al., *A hierarchical NeuroBayes-based algorithm for full reconstruction of B mesons at B factories*, Nuclear Instruments and Methods in Physics Research Section A: Accelerators, Spectrometers, Detectors and Associated Equipment **654** (2011) 432–440.

[139] J. Tanaka, *Precise measurements of charm meson lifetimes and search for D^0-$\overline{D}^0$ Mixing*. PhD thesis, Tokyo U., 2002.

[140] R. Brun, et al., *root-project/root: v6.18/02*, June, 2020. https://doi.org/10.5281/zenodo.3895860.

[141] R. Brun and F. Rademakers, *ROOT: An object oriented data analysis framework*, Nucl. Instrum. Meth. A **389** (1997) 81–86.

[142] M. Milesi, J. Tan, and P. Urquijo, *Lepton identification in Belle II using observables from the electromagnetic calorimeter and precision trackers*, EPJ Web Conf. **245** (2020) 06023.

[143] Belle-II Collaboration, I. Adachi et al., *A test of lepton flavor universality with a measurement of $R(D^*)$ using hadronic B tagging at the Belle II experiment*, arXiv:2401.02840 [hep-ex].

[144] Belle II Collaboration, I. Adachi, et al., *Tests of Light-Lepton Universality in Angular Asymmetries of $B^0 \to D^{*-}\ell\nu$ Decays*, Phys. Rev. Lett. **131** (2023) 181801.

[145] Belle II Collaboration, I. Adachi, et al., *Determination of $|V_{cb}|$ using $\overline{B}^0 \to D^{*+}\ell^-\overline{\nu}_\ell$ decays with Belle II*, Phys. Rev. D **108** (2023) 092013.

[146] V. Bertacchi, et al., *Track finding at Belle II*, Computer Physics Communications **259** (2021) 107610.

[147] V. Bertacchi and K. Trabelsi, *Observation of $B \to D^{(*)}K^-K^0_S$ decays using the 2019-2022 Belle II data sample*, Jan, 2023. BELLE2-NOTE-PH-2023-002.

[148] A. T. S.Stengel, *Optimization of π^0 reconstruction selection and first systematic uncertainty evaluation of the efficiencies*, Feb, 2020. BELLE2-NOTE-PH-2020-003.

[149] P. Cheema, et al., *Development of FastBDT Classifiers to Suppress Beam Background Clusters and Fake Photons*, Apr, 2023. BELLE2-NOTE-TE-2023-012.

[150] J. Tanaka, *Kinematic Fitting*, March, 1998. Belle Note 194.

[151] J.-F. Krohn, et al., *Global decay chain vertex fitting at Belle II*, Nuclear Instruments and Methods in Physics Research Section A: Accelerators, Spectrometers, Detectors and Associated Equipment **976** (2020) 164269.

[152] R. E. Kalman, *A New Approach to Linear Filtering and Prediction Problems*, Journal of Basic Engineering **82** (1960) 35–45.

[153] M. Röhrken, *Time-Dependent CP Violation Measurements in Neutral B Meson to Double-Charm Decays at the Japanese Belle Experiment*. PhD thesis, KIT, Karlsruhe, Dept. Phys., 2012.

[154] E. Farhi, *Quantum Chromodynamics Test for Jets*, Phys. Rev. Lett. **39** (1977) 1587–1588.

[155] G. C. Fox and S. Wolfram, *Observables for the Analysis of Event Shapes in e^+e^- Annihilation and Other Processes*, Phys. Rev. Lett. **41** (1978) 1581–1585.

[156] Belle II Collaboration, F. Bernlochner, et al., *First extraction of inclusive V_{cb} from q^2 moments*, JHEP**10** 068.

[157] Belle II Collaboration, *Curl Tagger MVA Documentation*, 2024. `https://software.belle2.org/light-2305-korat/sphinx/_modules/modularAnalysis.html#tagCurlTracks`. Access date: 2024-02-13.

[158] A. Hershenhorn, *Search for axion like particles with the BaBar detector and photon hadron separation using Zernike moments at Belle II*. PhD thesis, University of British Columbia, 2021. `https://open.library.ubc.ca/collections/ubctheses/24/items/1.0398055`.

[159] Q.-D. Zhou, *Correction for tracking momentum bias based on invariant mass peak studies*, Jun, 2020. BELLE2-NOTE-PH2020-030.

[160] Q.-D. Zhou, et al., *Correction for tracking momentum bias*, Feb, 2022. BELLE2-NOTE-PH-2022-006.

[161] F. J. Abudinen, et al., *Impact of photon-energy biases on candidate-reconstruction variables*, Mar, 2020. BELLE2-NOTE-TE-2020-011.

[162] J. X. Cui, et al., *Energy resolution and bias with* $E_\gamma < 2.0\,\text{GeV}$ *using symmetric decays of* $\pi^0 \to \gamma\gamma$ *and* $\eta \to \gamma\gamma$ *at Belle II*, Dec, 2020. BELLE2-NOTE-PH-2020-073.

[163] Belle II Lepton ID Group, *Muon and electron identification performance with* $189\,\text{fb}^{-1}$ *of Belle II data*, Apr, 2021. BELLE2-NOTE-TE-2021-011.

[164] S. Sandilya and A. Schwartz, *Study of Kaon and Pion Identification Performances in Phase III data with* D^{*+}*sample*, Jul, 2019. BELLE2-NOTE-PH-2019-048.

[165] Belle Collaboration, E. Waheed et al., *Measurement of the CKM matrix element* $|V_{cb}|$ *from* $B^0 \to D^{*-}\ell^+\nu_\ell$ *at Belle*, Phys. Rev. D **100** (2019) 052007, [Erratum: Phys.Rev.D 103, 079901 (2021)].

[166] D. Dorner, P. Rados, and C. Schwanda, *Relative tracking efficiency study of charged, low momentum pions*, Jul, 2023. BELLE2-NOTE-PH-2023-035.

[167] T.Koga, *momentum dependent* π^0 *efficiency measurement with D decays*, Sep, 2020. BELLE2-NOTE-PH-2020-061.

[168] W. Sutcliffe and F. Bernlochner, *Calibration of hadronic tagging with* $B \to X\ell\nu$ *decays with the LS1 Dataset*, Feb, 2023. BELLE2-NOTE-PH-2023-008.

[169] M. Liu, et al., *Hadronic FEI calibration with* $D^{(*)}\pi$ *samples*, Jan, 2023. BELLE2-NOTE-PH-2023-004.

[170] W. Sutcliffe, et al., *Combination of calibration factors for hadronic tagging*, Jun, 2023. BELLE2-NOTE-PH-2023-029.

[171] L. Heinrich, M. Feickert, and G. Stark, *pyhf: v0.7.5*, https://doi.org/10.5281/zenodo.1169739. https://github.com/scikit-hep/pyhf/releases/tag/v0.7.5.

[172] L. Heinrich, et al., *pyhf: pure-Python implementation of HistFactory statistical models*, Journal of Open Source Software **6** (2021) 2823.

[173] ROOT Collaboration, K. Cranmer, et al., *HistFactory: A tool for creating statistical models for use with RooFit and RooStats*, tech. rep., New York U., New York, 2012. https://cds.cern.ch/record/1456844.

[174] G. Cowan, et al., *Asymptotic formulae for likelihood-based tests of new physics*, The European Physical Journal C **71** (2011).

[175] G. Cowan, *Statistical Data Analysis*. Oxford science publications.

[176] W. Heisenberg, *Über den Bau der Atomkerne. I*, Zeitschrift für Physik **77** (1932) 1–11.

[177] A. Glazov, et al., *Measurement of the tracking efficiency in Phase 3 data using tau-pair events.*, Feb, 2020. BELLE2-NOTE-PH-2020-006.

[178] F. Abudinén, et al., *Measurement of the integrated luminosity of the Phase 2 data of the Belle II experiment*, Chinese Physics C **44** (2020) 021001.

[179] A. C. Aitken, *IV.—On Least Squares and Linear Combination of Observations*, Proceedings of the Royal Society of Edinburgh **55** (1936) 42–48.

[180] L. Lyons, D. Gibaut, and P. Clifford, *How to combine correlated estimates of a single physical quantity*, Nuclear Instruments and Methods in Physics Research Section A: Accelerators, Spectrometers, Detectors and Associated Equipment **270** (1988) 110–117.

[181] Belle Collaboration, A. Vossen, et al., *Measurement of the branching fraction of* $B \to D^{(*)}\pi\ell\nu_\ell$ *at Belle using hadronic tagging in fully reconstructed events*, Physs Rev. D **98** (2018).

[182] F. U. Bernlochner and Z. Ligeti, *Semileptonic* $B^{(s)}$ *decays to excited charmed mesons with* e^-, μ , τ *and searching for new physics with R* (D^{**}), Physical Review D **95** (2016) 014022.

[183] F. U. Bernlochner, Z. Ligeti, and D. J. Robinson, *Model-independent analysis of semileptonic B decays to* D^{**}*for arbitrary new physics*, Physical Review D **97** (2018).

[184] T. D. Lee, *A Theory of Spontaneous T Violation*, Phys. Rev. D **8** (1973) 1226–1239.

[185] W. Buchmüller, R. Rückl, and D. Wyler, *Leptoquarks in lepton-quark collisions*, Phys. Lett. B **191** (1987) 442–448.

Appendices

APPENDIX A

D meson decay study

Additional histograms for the performed importance study for the different reconstructed D mesons in dependence of each considered B meson decay channel. All channels on or above the red line in the histograms are removed for this analysis.

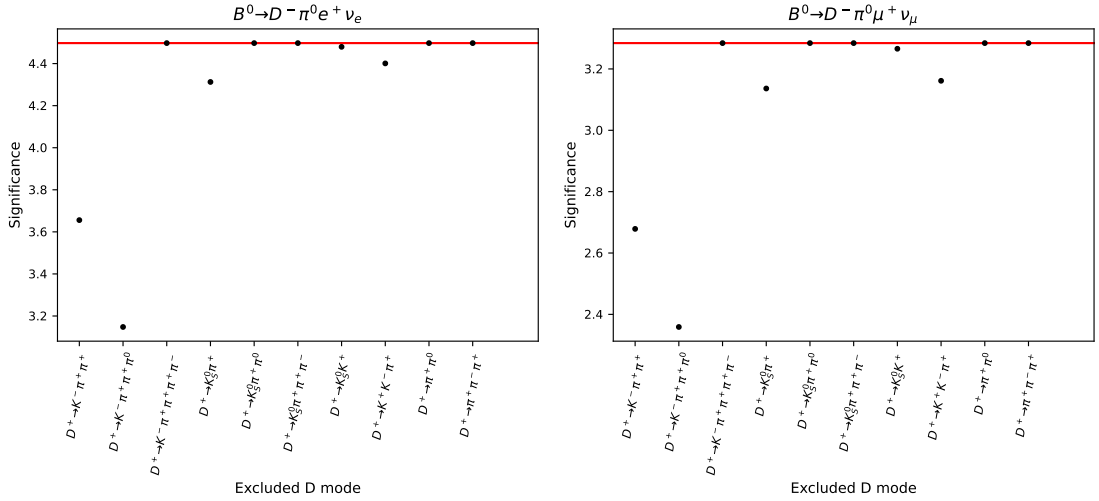

Figure A.1.: Histogram showing the significance for one reconstructed B meson (in the title), where the lepton is an electron on the left-hand side or a muon on the right-hand side. The overall significance is portrayed by the red line and the excluded reconstructed D meson decay mode is shown on the x-axis.

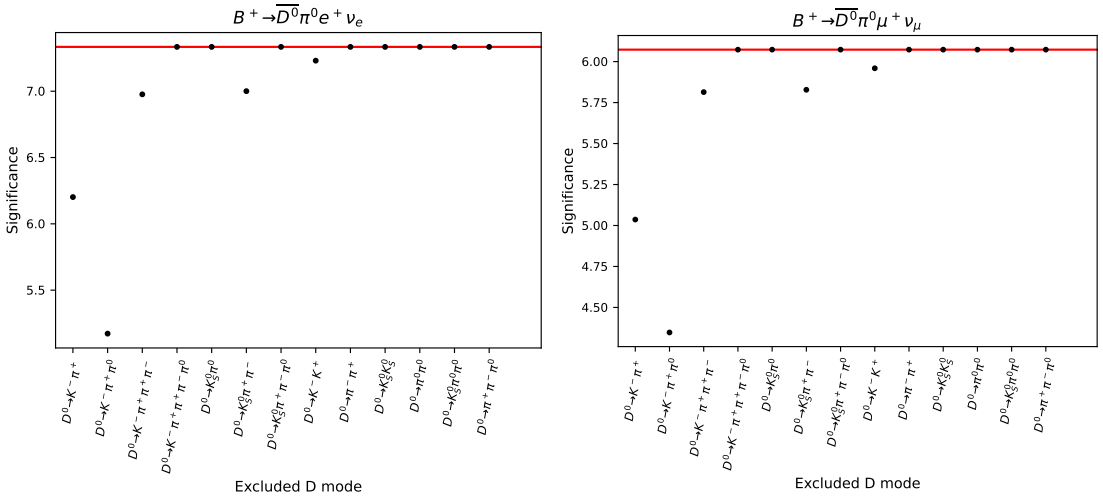

Figure A.2.: Histogram showing the significance for one reconstructed B meson (in the title), where the lepton is an electron on the left-hand side or a muon on the right-hand side. The overall significance is portrayed by the red line and the excluded reconstructed D meson decay mode is shown on the x-axis.

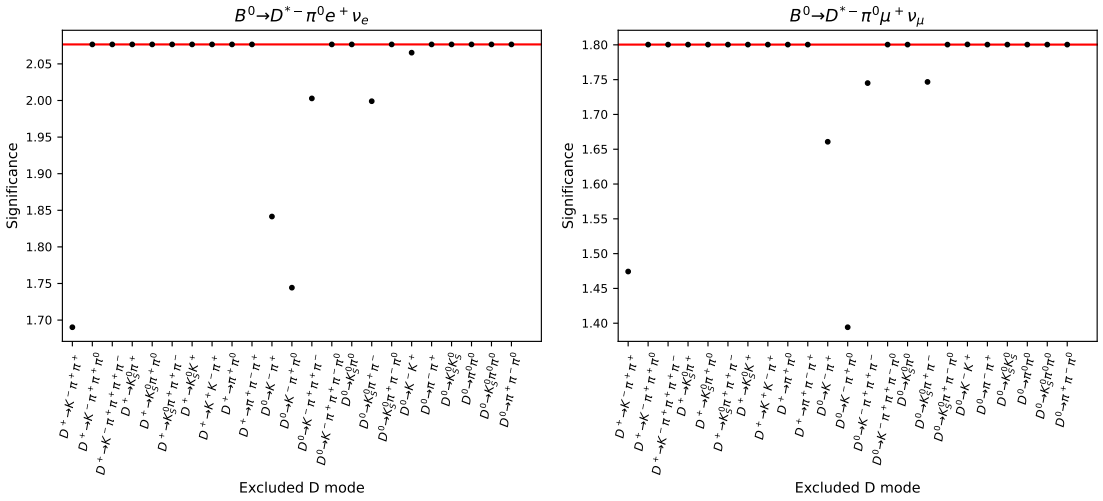

Figure A.3.: Histogram showing the significance for one reconstructed B meson (in the title), where the lepton is an electron on the left-hand side or a muon on the right-hand side. The overall significance is portrayed by the red line and the excluded reconstructed D meson decay mode is shown on the x-axis.

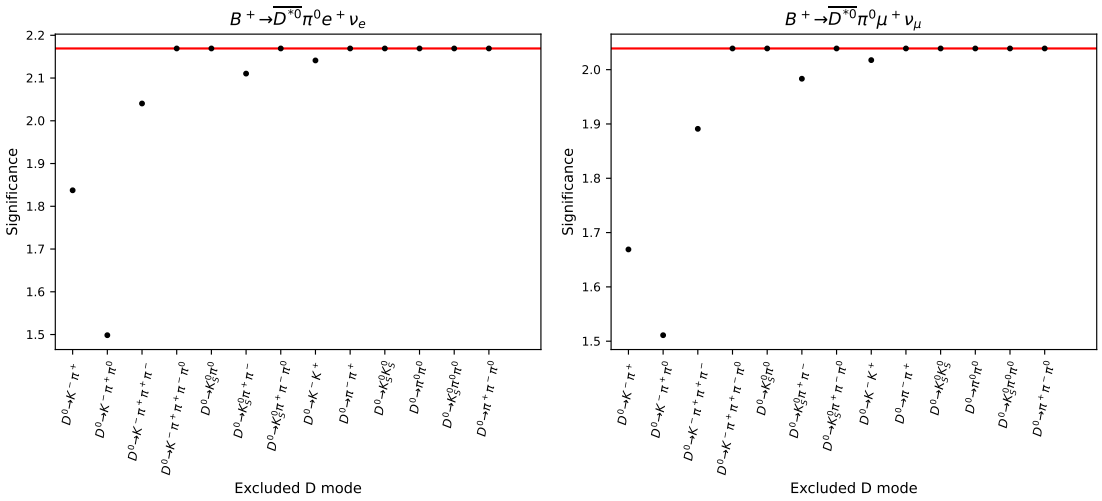

Figure A.4.: Histogram showing the significance for one reconstructed B meson (in the title), where the lepton is an electron on the left-hand side or a muon on the right-hand side. The overall significance is portrayed by the red line and the excluded reconstructed D meson decay mode is shown on the x-axis.

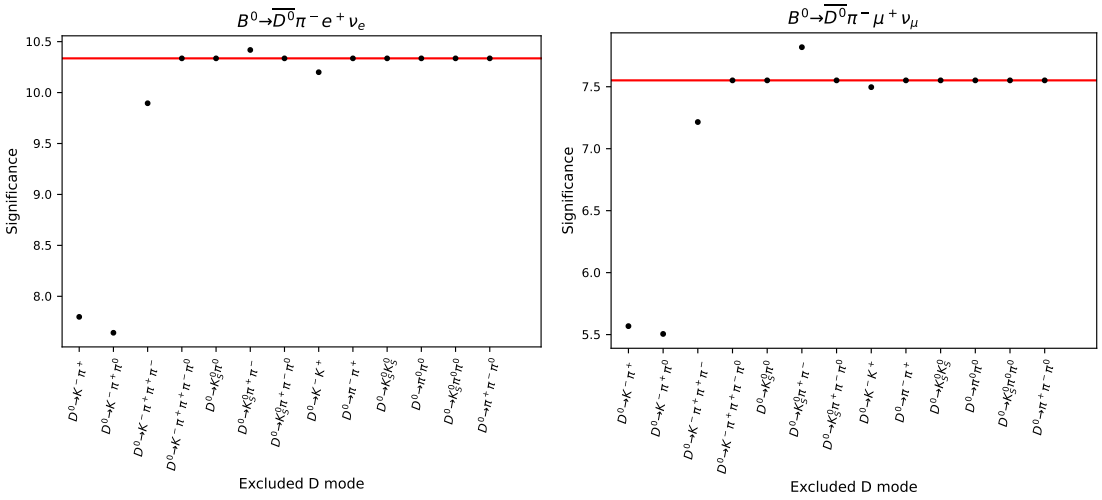

Figure A.5.: Histogram showing the significance for one reconstructed B meson (in the title), where the lepton is an electron on the left-hand side or a muon on the right-hand side. The overall significance is portrayed by the red line and the excluded reconstructed D meson decay mode is shown on the x-axis.

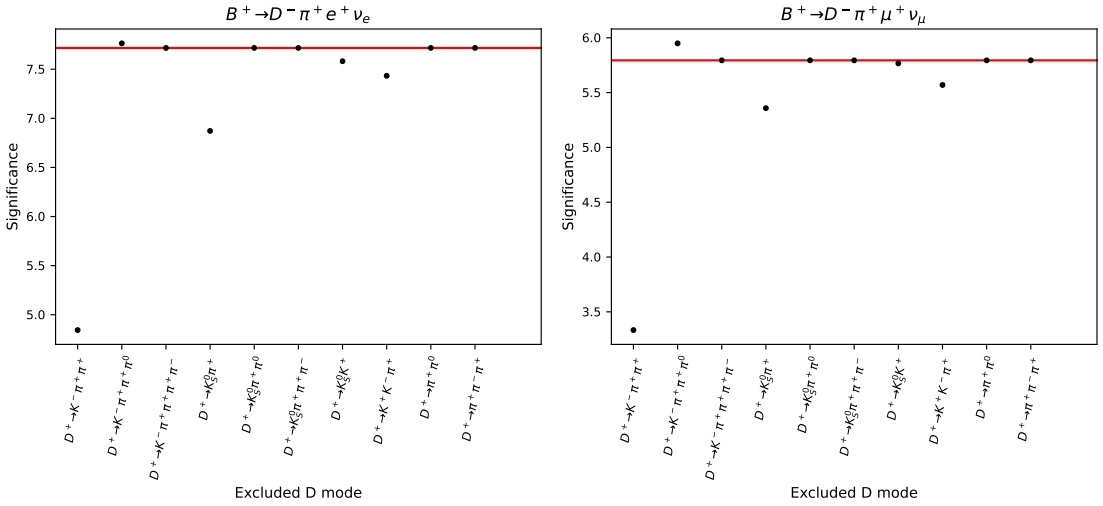

Figure A.6.: Histogram showing the significance for one reconstructed B meson (in the title), where the lepton is an electron on the left-hand side or a muon on the right-hand side. The overall significance is portrayed by the red line and the excluded reconstructed D meson decay mode is shown on the x-axis.

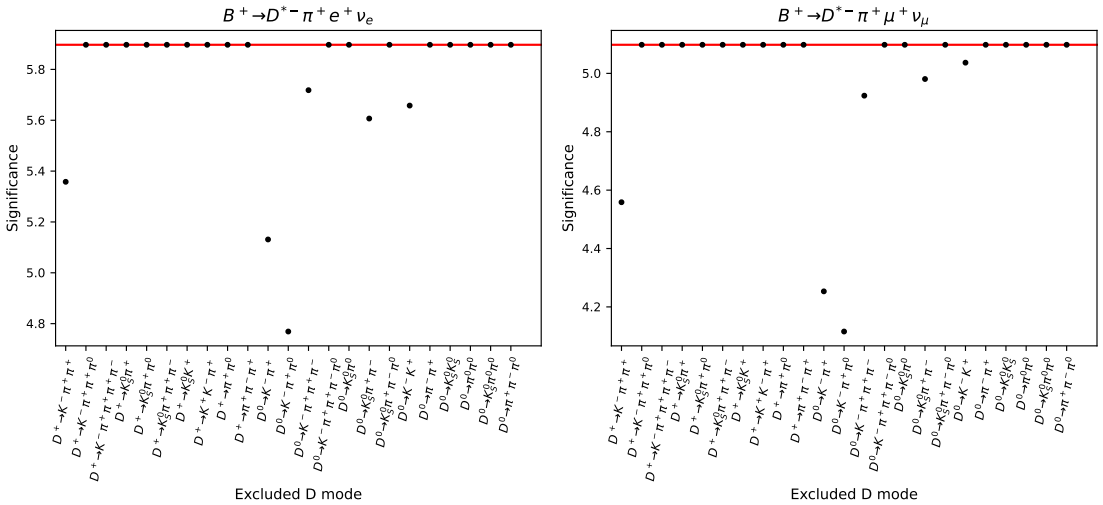

Figure A.7.: Histogram showing the significance for one reconstructed B meson (in the title), where the lepton is an electron on the left-hand side or a muon on the right-hand side. The overall significance is portrayed by the red line and the excluded reconstructed D meson decay mode is shown on the x-axis.

APPENDIX B

Prefit distributions for the $B \to D^{**}\ell\nu_\ell$ decays

Prefit distributions to compare the agreement between simulation and data for the $B \to D^{**}\ell\nu_\ell$ decays. Besides, the different templates can be seen.

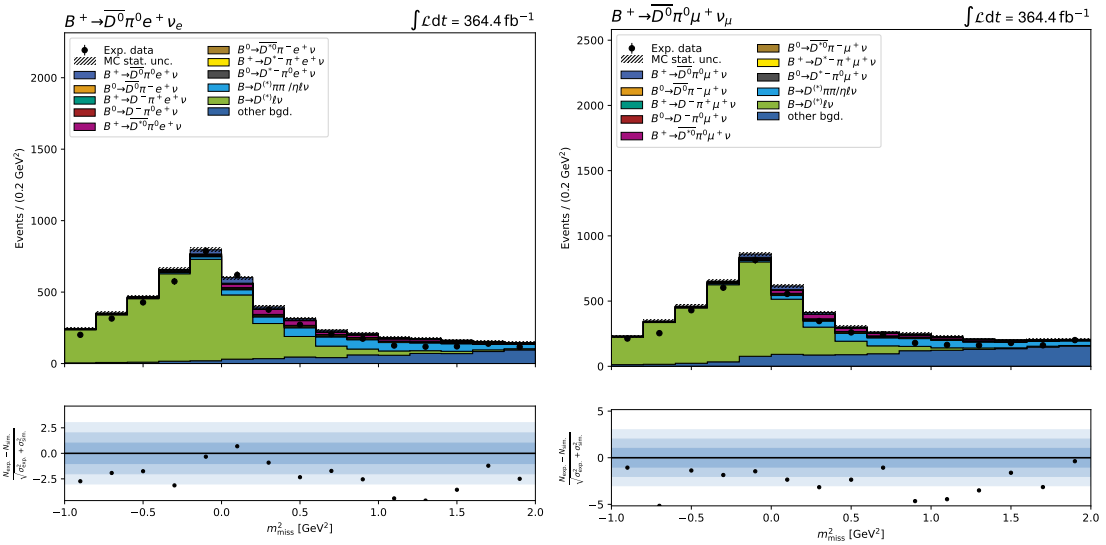

(a) Electron (b) Muon

Figure B.1.: Prefit distributions showing the agreement between simulation and data for the decay in the title, on the left-hand side for the electron and on the right-hand side for the muon.

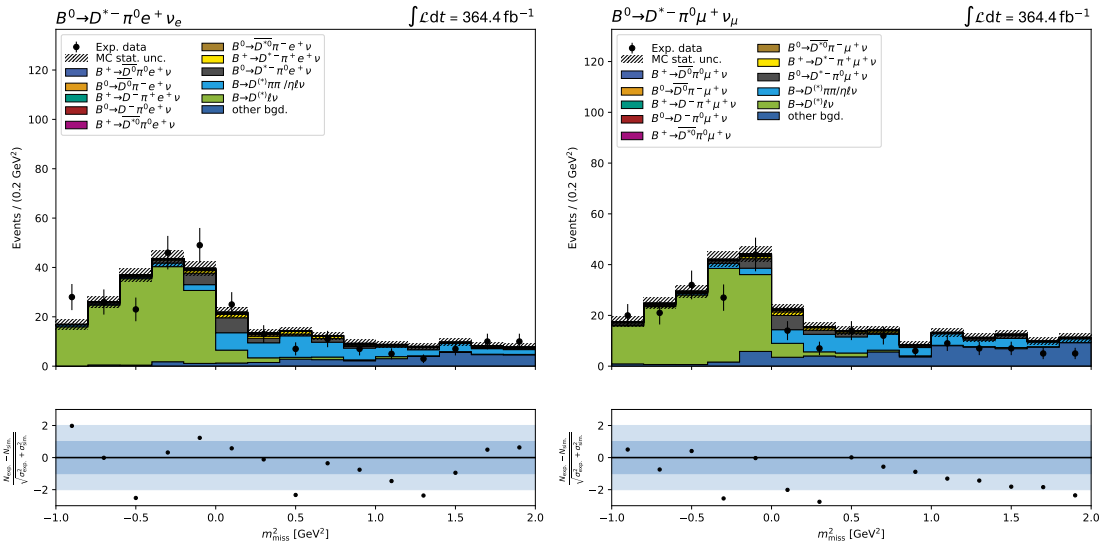

(a) Electron (b) Muon

Figure B.2.: Prefit distributions showing the agreement between simulation and data for the decay mode indicated in the title, on the left-hand side for the electron and on the right-hand side for the muon.

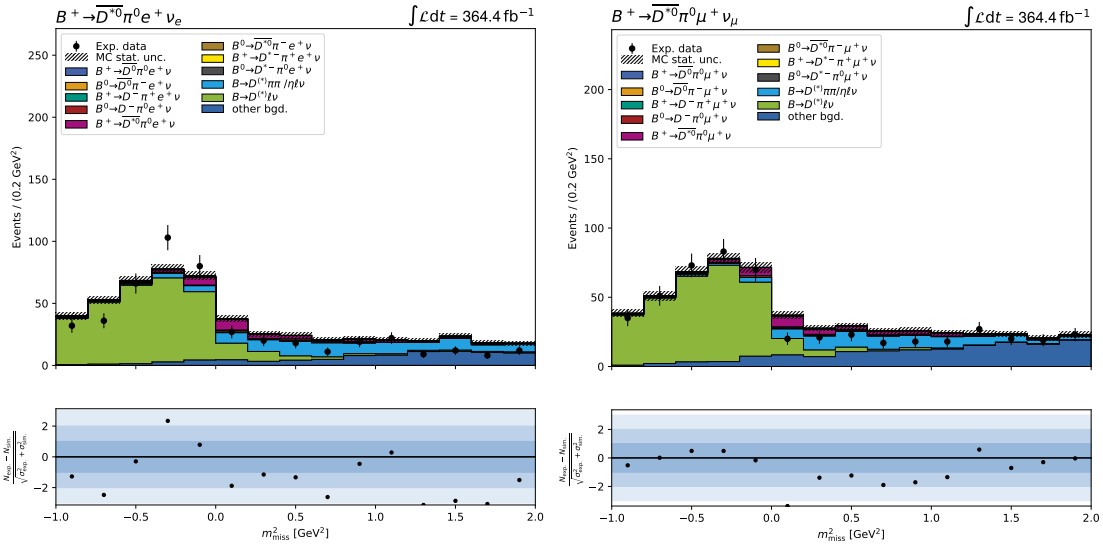

(a) Electron (b) Muon

Figure B.3.: Prefit distributions showing the agreement between simulation and data for the decay mode indicated in the title, on the left-hand side for the electron and on the right-hand side for the muon.

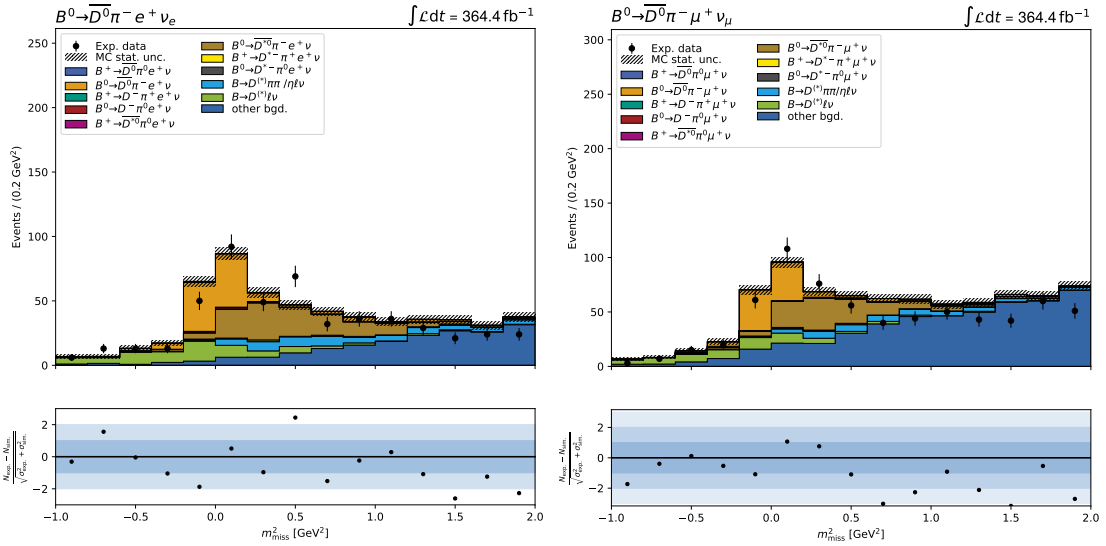

(a) Electron (b) Muon

Figure B.4.: Prefit distributions showing the agreement between simulation and data for the decay mode indicated in the title, on the left-hand side for the electron and on the right-hand side for the muon.

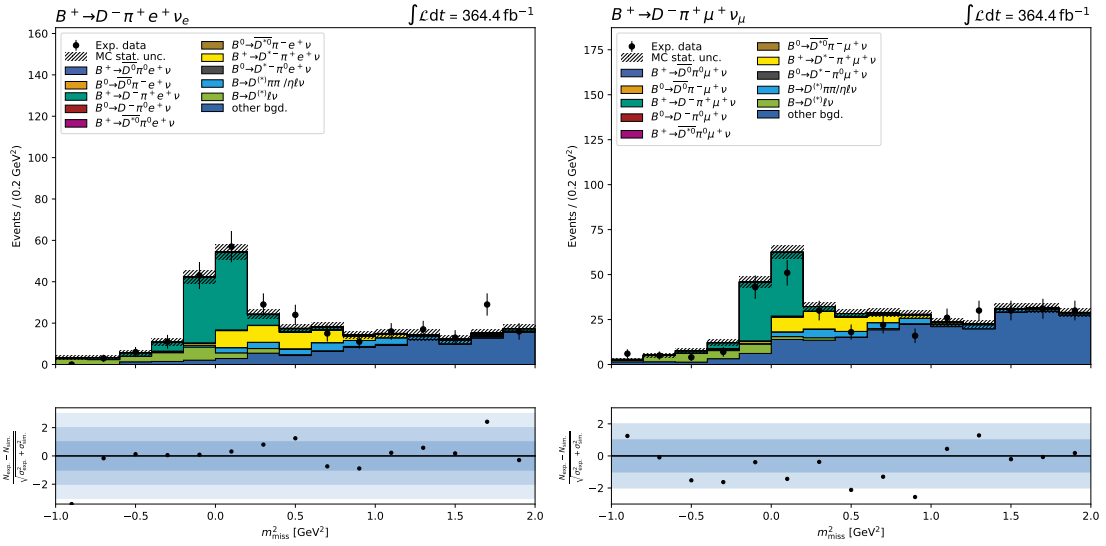

(a) Electron (b) Muon

Figure B.5.: Prefit distributions showing the agreement between simulation and data for the decay mode indicated in the title, on the left-hand side for the electron and on the right-hand side for the muon.

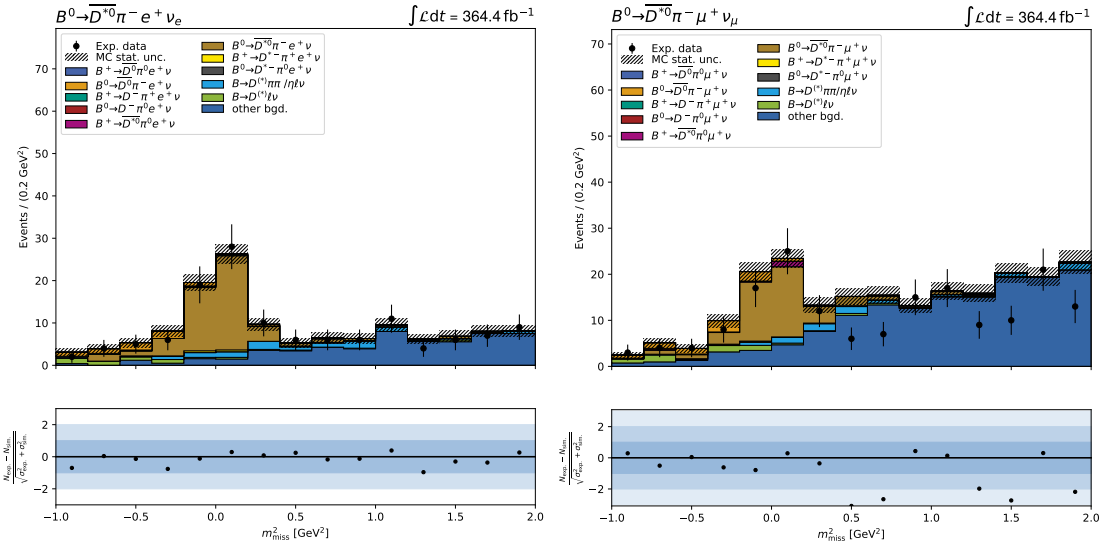

(a) Electron (b) Muon

Figure B.6.: Prefit distributions showing the agreement between simulation and data for the decay mode indicated in the title, on the left-hand side for the electron and on the right-hand side for the muon.

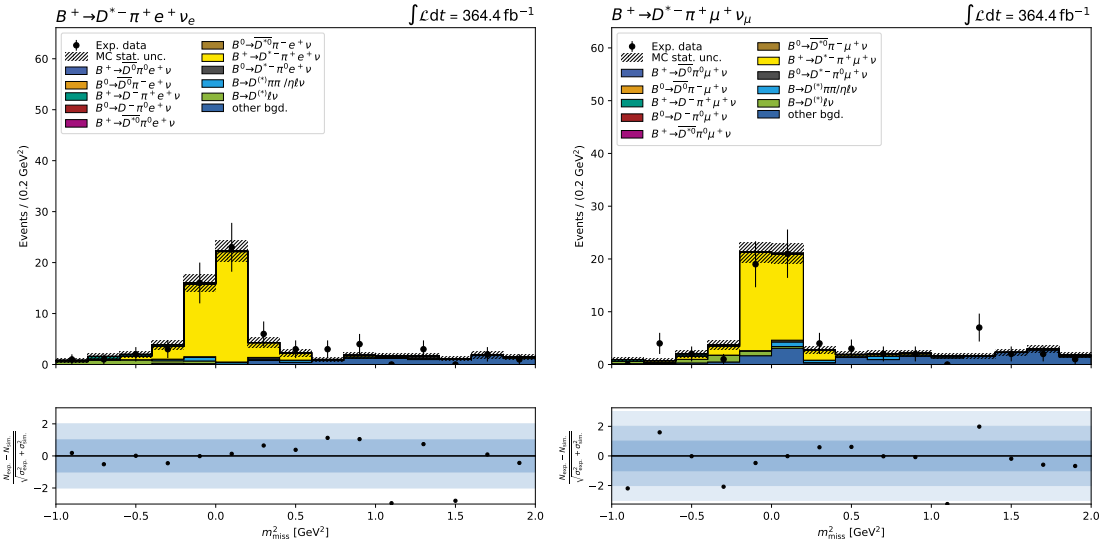

(a) Electron (b) Muon

Figure B.7.: Prefit distributions showing the agreement between simulation and data for the decay mode indicated in the title, on the left-hand side for the electron and on the right-hand side for the muon.

APPENDIX C

Prefit distributions for the $B \to D^* \ell \nu_\ell$ decays

Prefit distributions to validate the agreement between simulation and recorded data for the $B \to D^* \ell \nu_\ell$ decays.

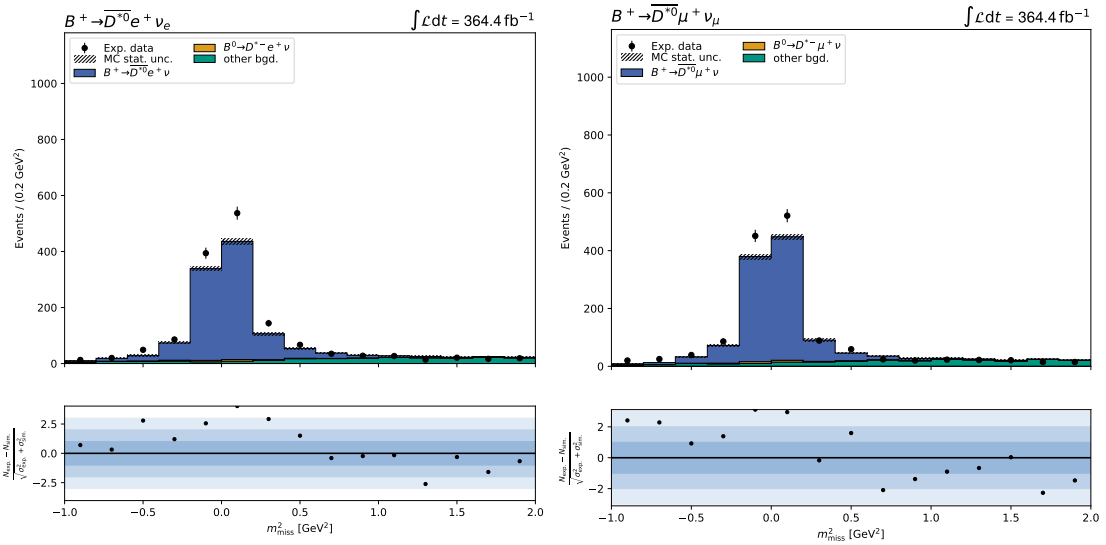

(a) Electron (b) Muon

Figure C.1.: Prefit distributions showing the agreement between simulation and data for the decay mode indicated in the title, on the left-hand side for the electron and on the right-hand side for the muon.

APPENDIX D

Postfit distributions for the $B \to D^{**}\ell\nu_\ell$ decays

Postfit distributions to compare the agreement between simulation and data for the $B \to D^{**}\ell\nu_\ell$ decays after the fit has been performed.

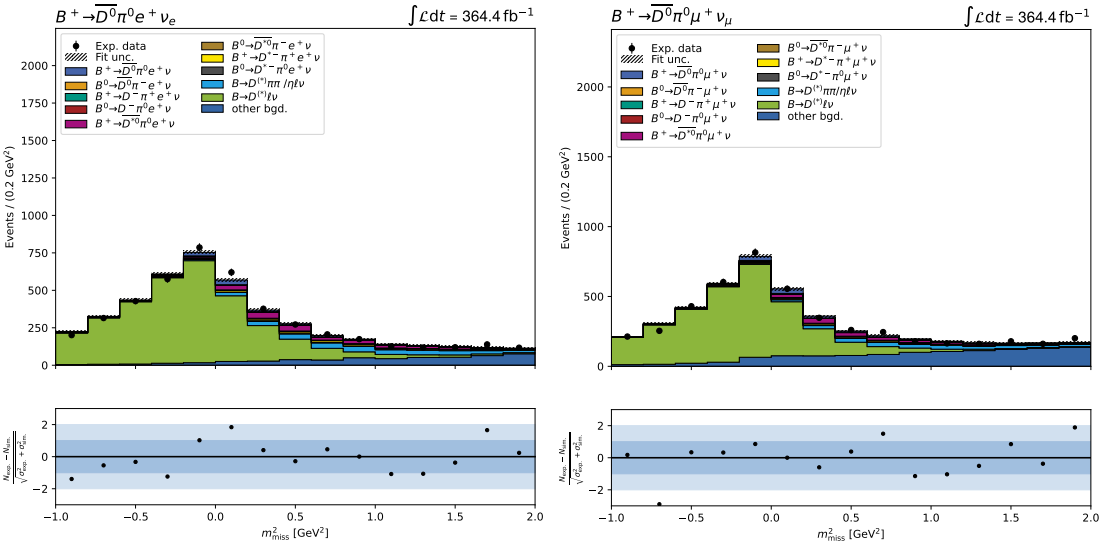

(a) Electron (b) Muon

Figure D.1.: Postfit distributions showing the agreement between simulation and data for the decay in the title, on the left-hand side for the electron and on the right-hand side for the muon after the fit has been performed.

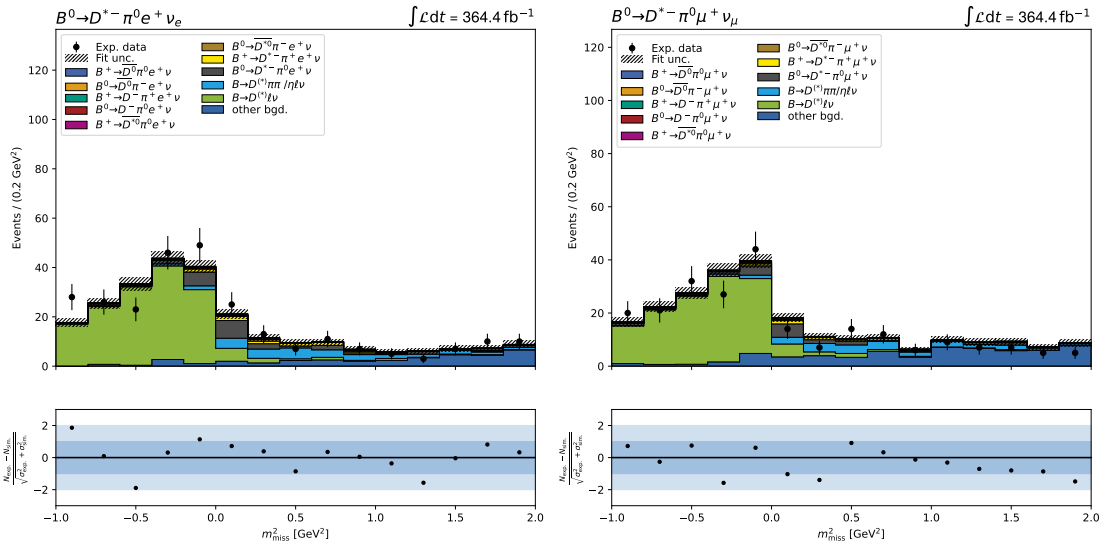

(a) Electron (b) Muon

Figure D.2.: Postfit distributions showing the agreement between simulation and data for the decay in the title, on the left-hand side for the electron and on the right-hand side for the muon after the fit has been performed.

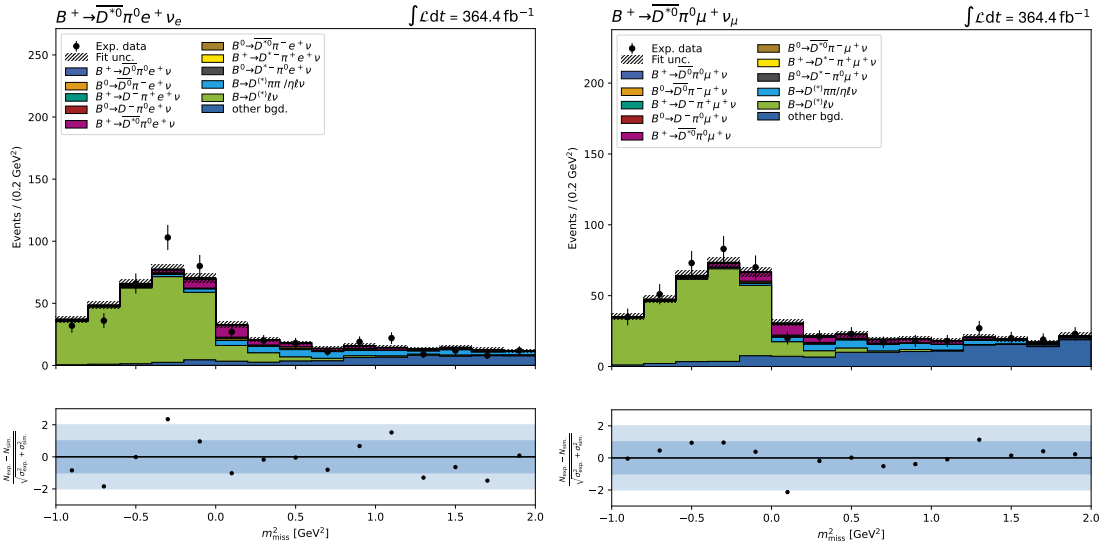

(a) Electron (b) Muon

Figure D.3.: Postfit distributions showing the agreement between simulation and data for the decay in the title, on the left-hand side for the electron and on the right-hand side for the muon after the fit has been performed.

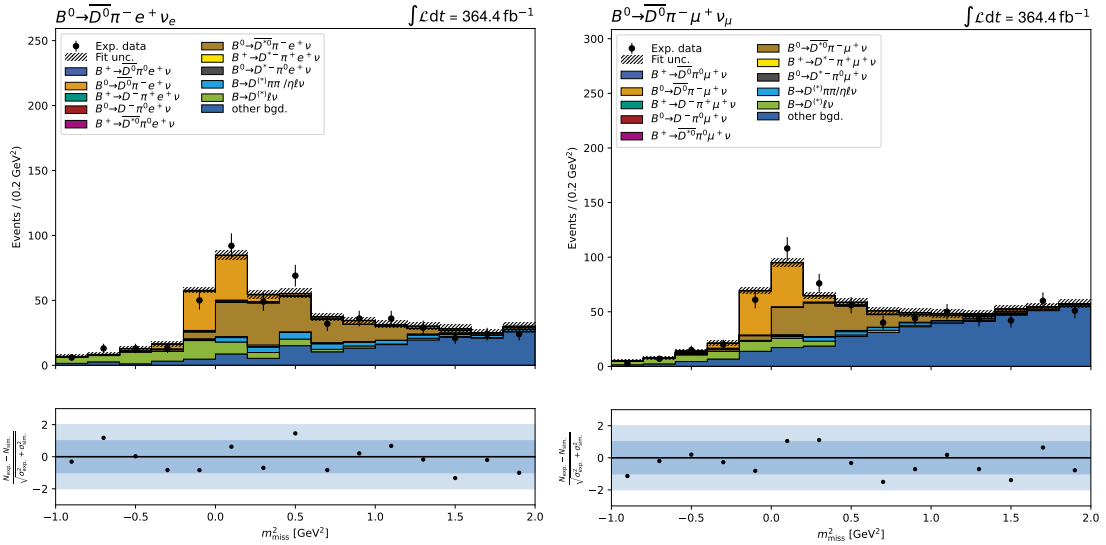

(a) Electron (b) Muon

Figure D.4.: Postfit distributions showing the agreement between simulation and data for the decay in the title, on the left-hand side for the electron and on the right-hand side for the muon after the fit has been performed.

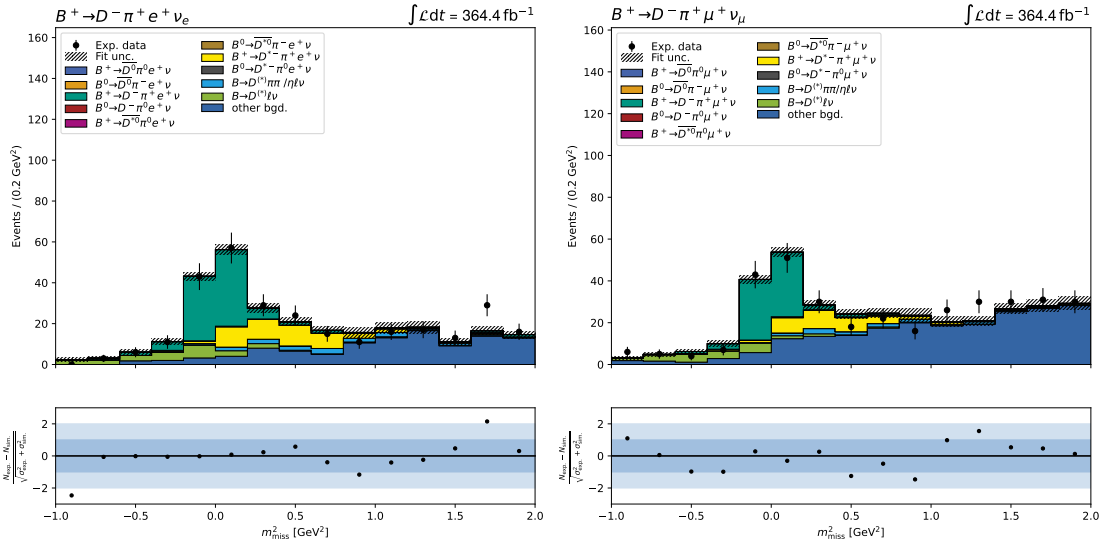

(a) Electron (b) Muon

Figure D.5.: Postfit distributions showing the agreement between simulation and data for the decay in the title, on the left-hand side for the electron and on the right-hand side for the muon after the fit has been performed.

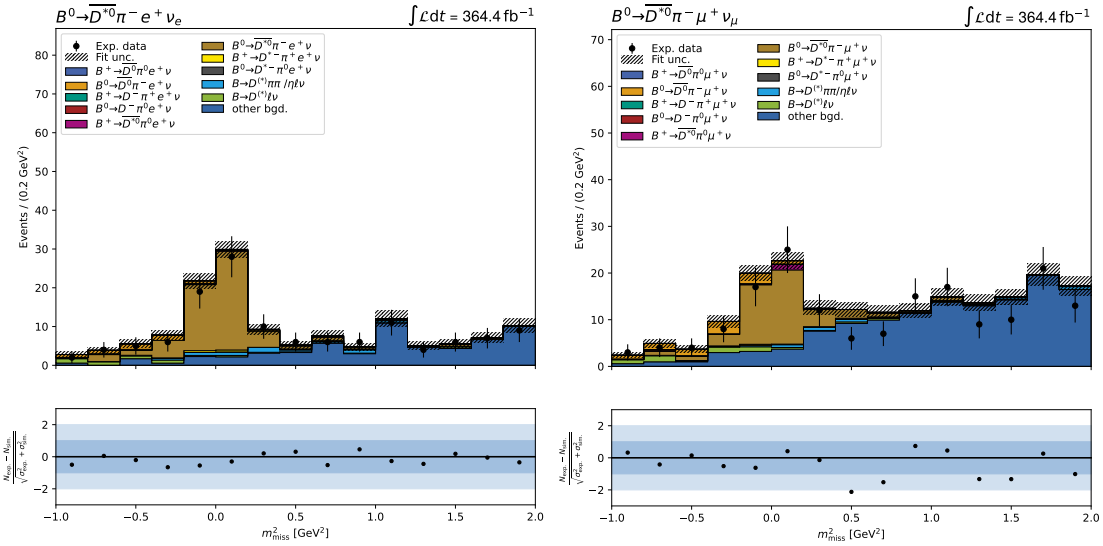

(a) Electron (b) Muon

Figure D.6.: Postfit distributions showing the agreement between simulation and data for the decay in the title, on the left-hand side for the electron and on the right-hand side for the muon after the fit has been performed.

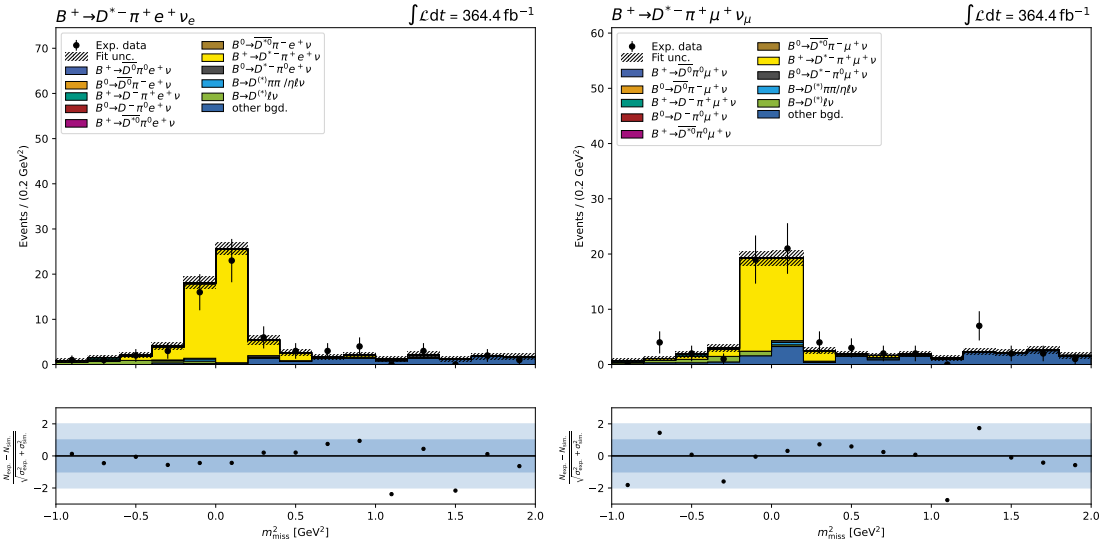

(a) Electron (b) Muon

Figure D.7.: Postfit distributions showing the agreement between simulation and data for the decay in the title, on the left-hand side for the electron and on the right-hand side for the muon after the fit has been performed.

APPENDIX E

Postfit distributions for the $B \to D^* \ell \nu_\ell$ decays

Postfit distributions to validate the agreement between simulation and recorded data for the $B \to D^* \ell \nu_\ell$ decays after the application of the determined scaling parameters by the fit.

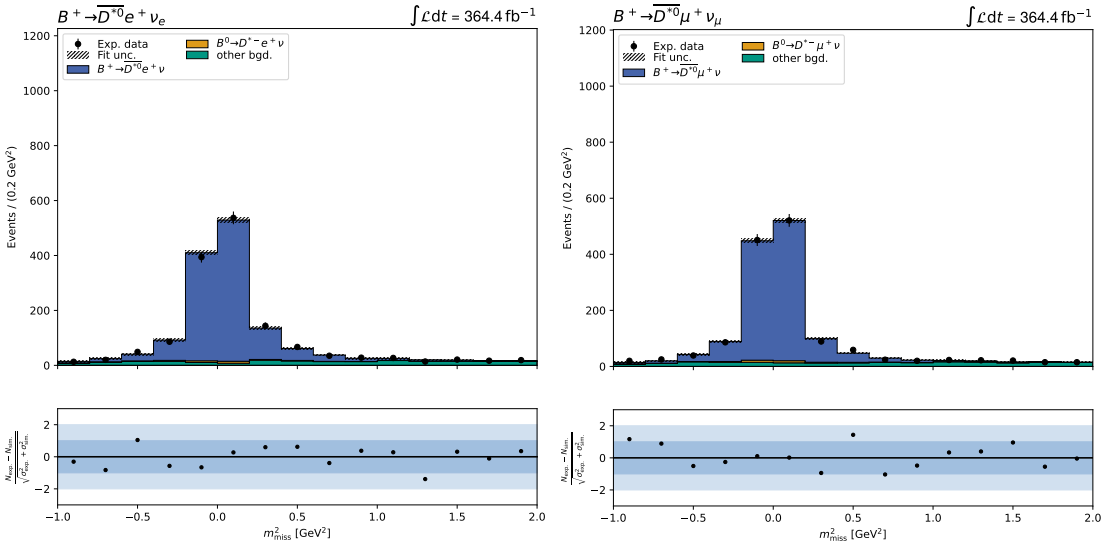

(a) Electron (b) Muon

Figure E.1.: Postfit distributions showing the agreement between simulation and data for the decay in the title, on the left-hand side for the electron and on the right-hand side for the muon after the performed fit.

APPENDIX F

Pull plots for each scaling parameter of the $B \to D^{**}\ell\nu_\ell$ decay

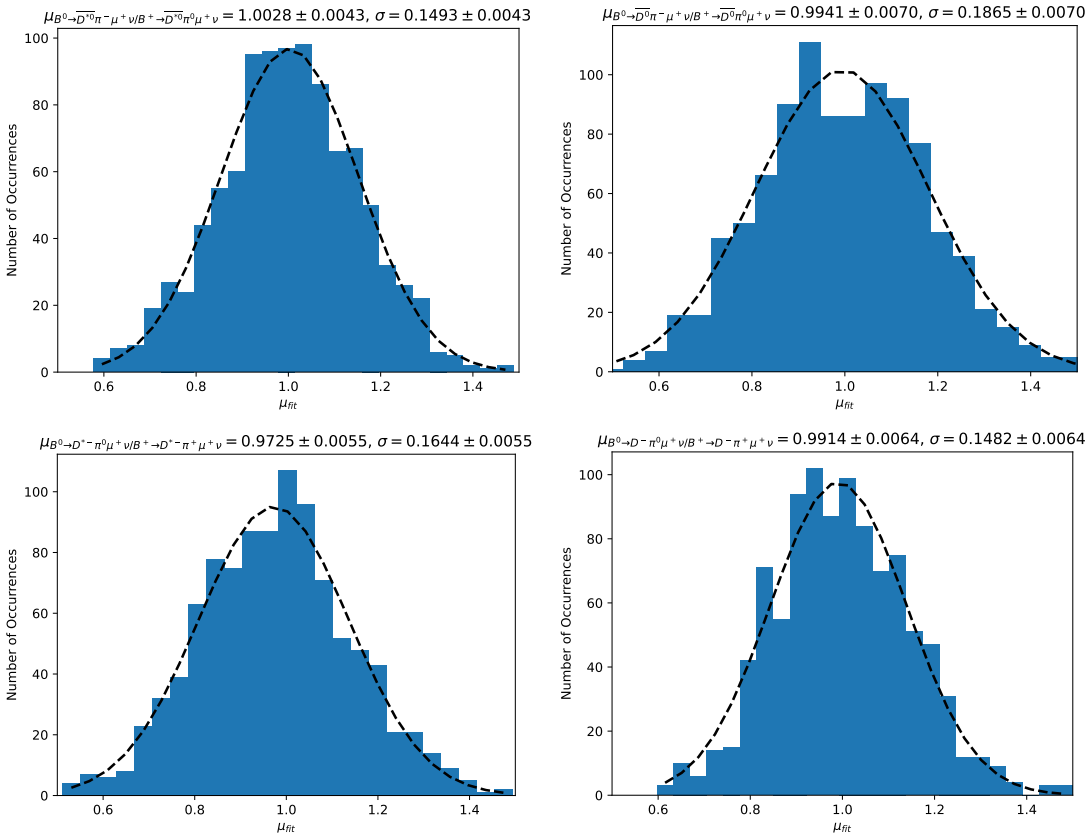

Figure F.1.: Scaling parameter determined in the fit for each signal category including its uncertainties for the muon modes.

APPENDIX G

Pull plots for each scaling parameter of the $B \to D^* \ell \nu_\ell$ decay

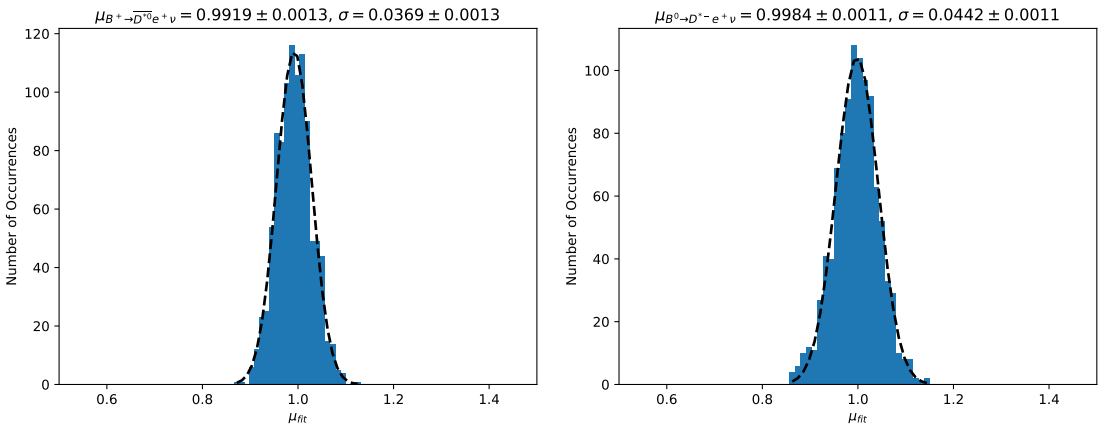

Figure G.1.: Scaling parameter determined in the fit for each signal category including its uncertainties for the electron modes.

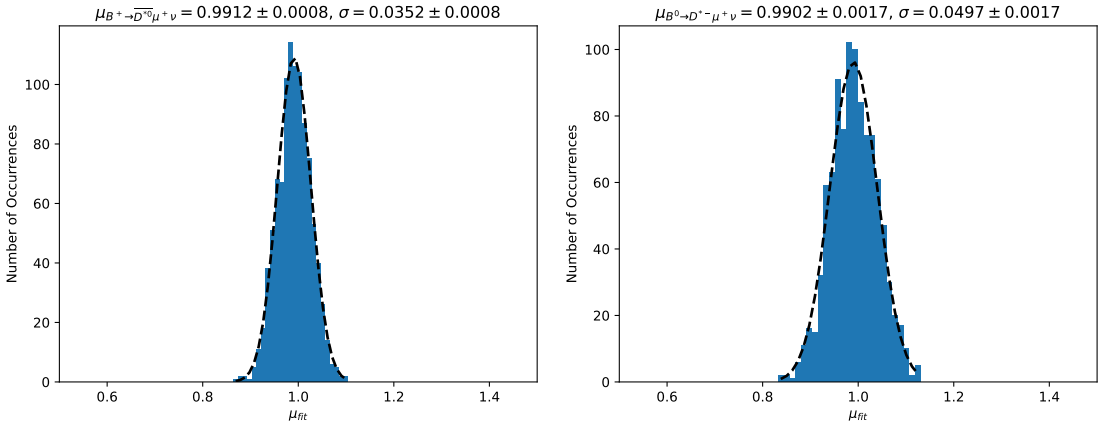

Figure G.2.: Scaling parameter determined in the fit for each signal category including its uncertainties for the muon modes.

APPENDIX H

Pull distributions for each $B \to D^{**}\ell\nu_\ell$ decay

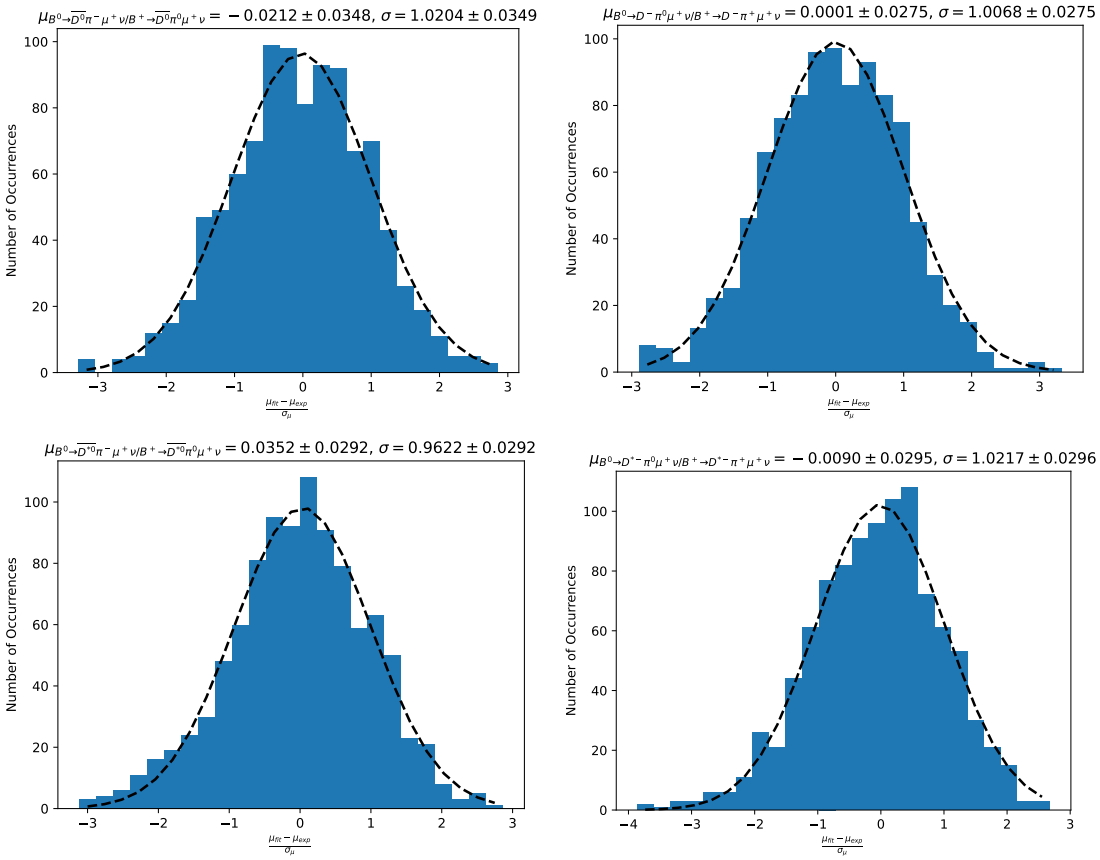

Figure H.1.: Pull distributions for all signal templates, where the corresponding category can be found at the top left of the plot in the subscript of the μ. The μ corresponds to the width of the distribution for the muon mode.

APPENDIX I

Pull distributions for each $B \to D^* \ell \nu_\ell$ decay

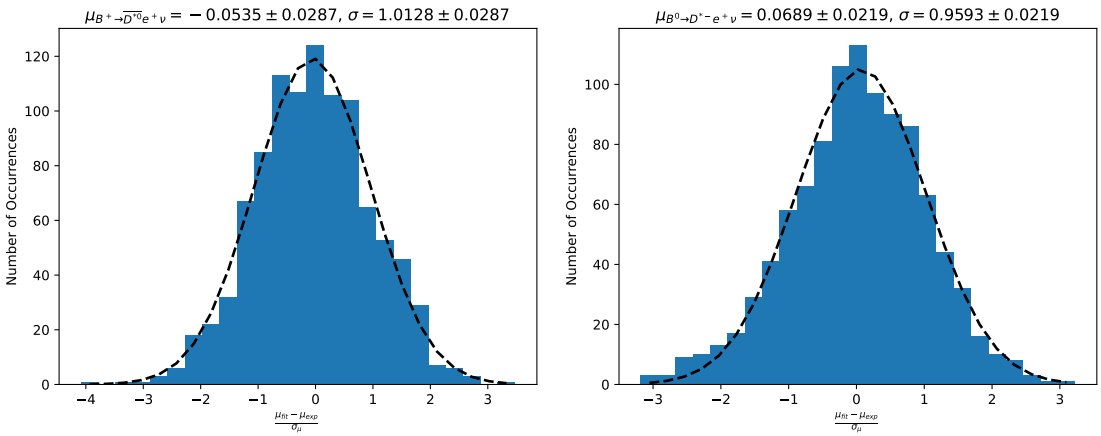

Figure I.1.: Pull distributions for all signal templates, where the corresponding category can be found at the top left of the plot in the subscript of the μ. The μ corresponds to the width of the distribution for the electron mode.

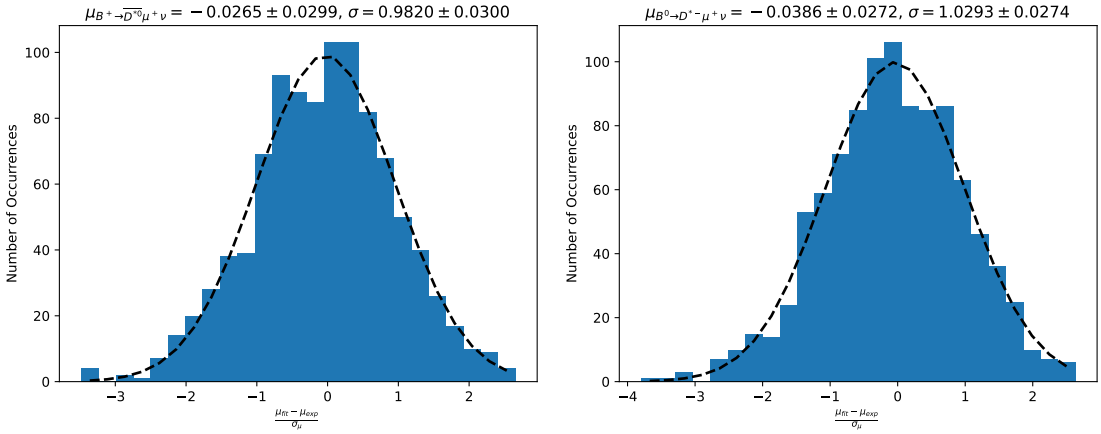

Figure I.2.: Pull distributions for all signal templates, where the corresponding category can be found at the top left of the plot in the subscript of the μ. The μ corresponds to the width of the distribution for the muon mode.

APPENDIX J

Fit validation on data for $B \to D^* \ell \nu_\ell$ decays

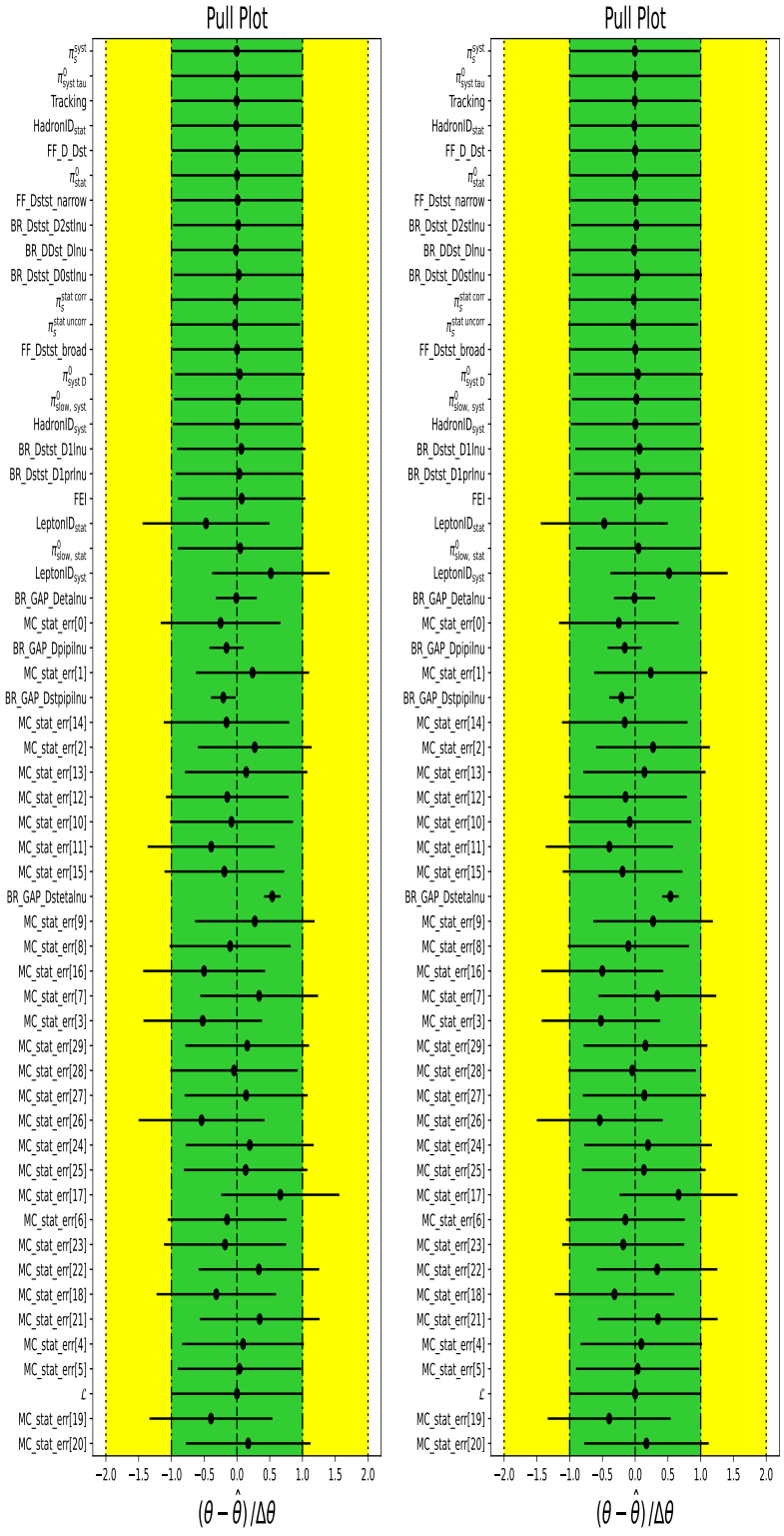

Figure J.1.: Mean and width of the pull distributions for the fit using the electron mode on the left-hand side and the muon on the right-hand side including all the systematic uncertainties considered as nuisance parameters for the $B \to D^* \ell \nu_\ell$ decay mode.

APPENDIX K

ROE sideband distributions

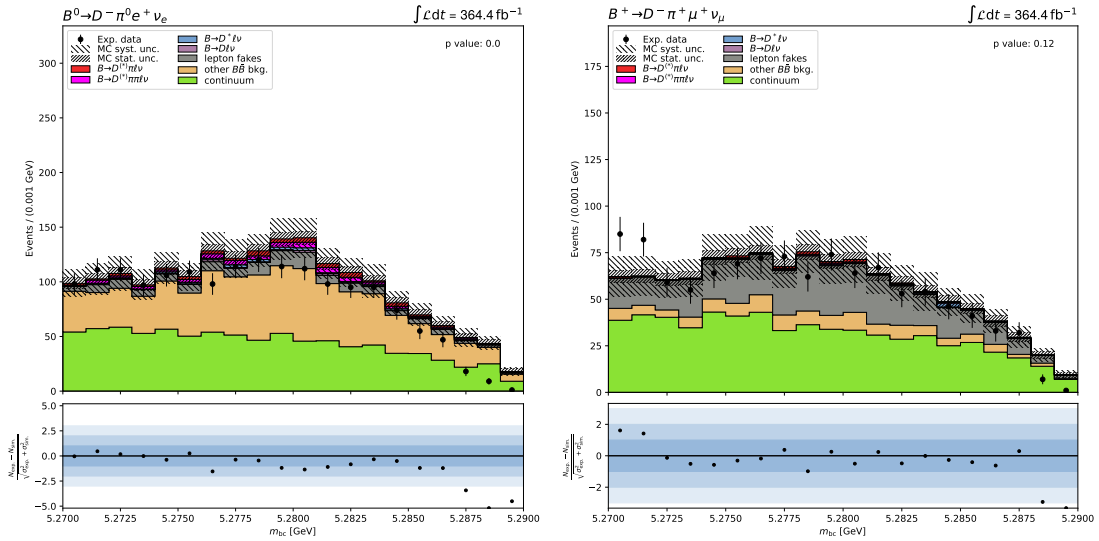

Figure K.1.: Distributions for M_{bc} of the B_{Tag} meson for two $B \to D^{**} \ell \nu_\ell$ decay modes, which can be found in the title of the plots.

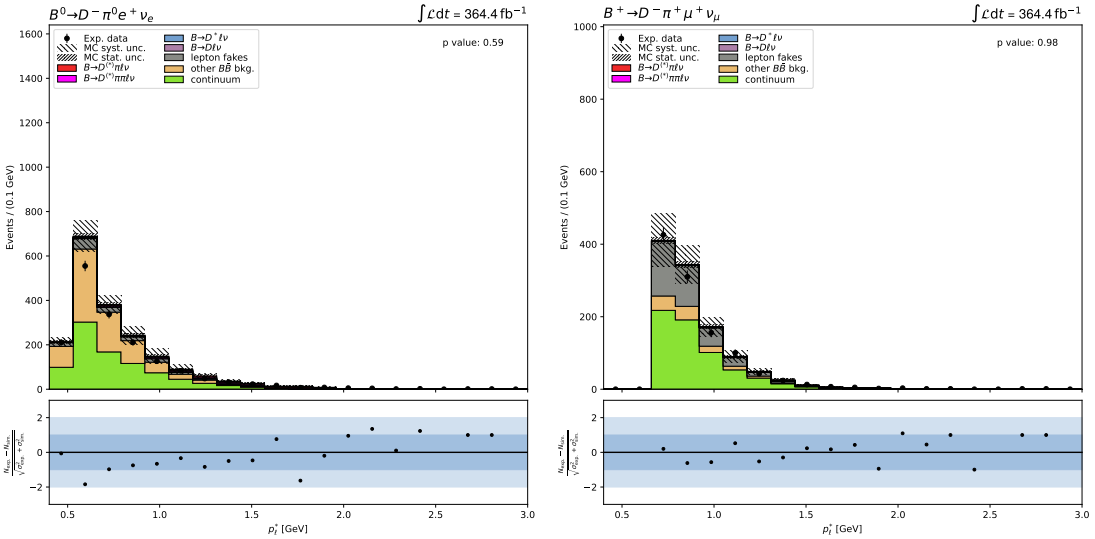

Figure K.2.: Distributions for the momentum of the light charged lepton in the CMS frame for two $B \to D^{**} \ell \nu_\ell$ decay modes, which can be found in the title of the plots.

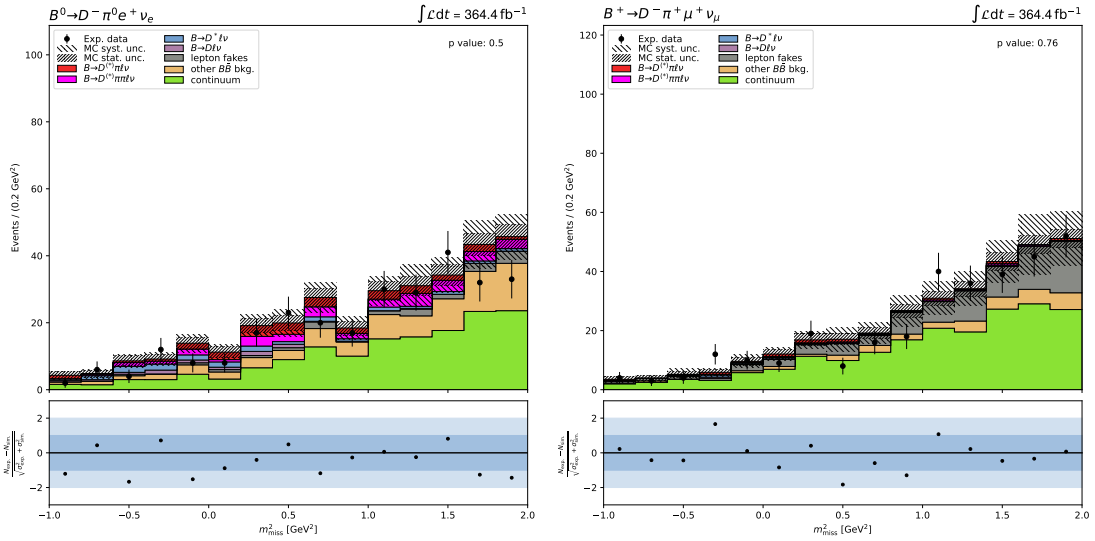

Figure K.3.: Distributions for m^2_{miss} for two $B \to D^{**} \ell \nu_\ell$ decay modes, which can be found in the title of the plots.

APPENDIX L

Systematic uncertainty tables for the normalisation fit

Source	$B^0 \to D^{*-} e^+ \nu_e$	$B^+ \to \overline{D}^{*0} e^+ \nu_e$
Statistical	4.9	3.7
Systematic uncertainties		
Tagging efficiency	7.4	8.8
$\mathcal{B}(B \to D^{(*)}/\eta\pi\pi\ell\nu_\ell)$	< 0.1	<0.1
$\mathcal{B}(B \to D^{**}\ell\nu_\ell)$	<0.1	<0.1
$\mathcal{B}(B \to D\ell\nu_\ell)$	<0.1	<0.1
FF(Broad D^{**})	<0.1	<0.1
FF(Narrow D^{**})	<0.1	<0.1
FF($D^{(*)}$)	<0.1	<0.1
Tracking efficiency	0.9	0.9
$\pi^{\pm}_{\text{slow}}$	2.1	<0.1
HadronID	1.0	0.9
LeptonID	0.5	1.2
Luminosity	3.5	3.5
π^0	1.8	2.7
π^0_{slow}	2.1	8.8
MC statistics	1.5	1.1

Table L.1.: All considered systematic uncertainties as well as the statistical uncertainty for the signal categories in the normalisation fit using the electron as the light charged lepton in percent.

Source	$B^0 \to D^{*-}\mu^+\nu_\mu$	$B^+ \to \overline{D}^{*0}\mu^+\nu_\mu$
Statistical	5.1	3.6
Systematic uncertainties		
Tagging efficiency	6.8	8.2
$\mathcal{B}(B \to D^{(*)}/\eta\pi\pi\ell\nu_\ell)$	<0.1	<0.1
$\mathcal{B}(B \to D^{**}\ell\nu_\ell)$	<0.1	<0.1
$\mathcal{B}(B \to D\ell\nu_\ell)$	<0.1	<0.1
FF(Broad D^{**})	<0.1	<0.1
FF(Narrow D^{**})	<0.1	<0.1
FF($D^{(*)}$)	<0.1	<0.1
Tracking efficiency	0.9	0.9
$\pi^{\pm}_{\text{slow}}$	2.1	<0.1
HadronID	1.0	0.9
LeptonID	1.5	1.3
Luminosity	3.4	3.4
π^0	1.7	2.7
π^0_{slow}	1.0	4.1
MC statistics	1.6	1.0

Table L.2.: All considered systematic uncertainties as well as the statistical uncertainty for the signal categories in the normalisation fit using the muon as the light charged lepton in percent.

Danksagung

Zunächst möchte ich mich recht herzlich bei allen Leuten bedanken, die mich während meiner Promotion unterstützt haben.
Dabei gebührt besonderer Dank Ariane Frey, welche mir die Möglichkeit gab, meine Doktorarbeit in ihrer Arbeitsgruppe zu schreiben. Ihre Unterstützung während der gesamten Bearbeitungszeit war immer sehr hilfreich, auch wenn einiges mal nicht ganz nach Plan lief.
Mein weiterer Dank gebührt Thibaud Humair, welcher als Zweitgutachter fungiert für diese Arbeit. Des Weiteren möchte ich mich bei den anderen Mitgliedern des Prüfungsaussschusses Jörn Große-Knetter, Stan Lai, Steffen Schumann und Baida Achkar bedanken.
Außerdem möchte ich mich noch bei der gesamten Arbeitsgruppe für die gute Arbeitsatmosphäre und die tollen Unternehmungen, wie das Kartfahren und die schönen Weihnachtsmarktbesuche, bedanken.
Besonderer Dank geht hier auch an die Leute, die meine Arbeit probegelesen haben: Thomas Rauls, Uwe Gebauer, Yannik Buch, Marike Schwickardi, Moritz Bauer, Tommy Martinov, Merle Graf-Schreiber, Sreelakshmi Sindhu, Rahila Kumar und Ilias Tsaklidis.
Zu guter Letzt möchte ich mich noch bei meiner Familie und meinen Freunden bedanken. Ohne euch hätte ich das ganze nie geschafft!